June 2024

# Investigating the Impact of Inverter-Based Resources on Power Grid Dynamics

Ratik Mittal
*University of South Florida*

Scholar Commons Citation

Mittal, Ratik, "Investigating the Impact of Inverter-Based Resources on Power Grid Dynamics" (2024). *USF Tampa Graduate Theses and Dissertations.*
https://digitalcommons.usf.edu/etd/10542

# Investigating the Impact of Inverter-Based Resources on Power Grid Dynamics

by

Ratik Mittal

A dissertation submitted in partial fulfillment
of the requirements for the degree of
Doctor of Philosophy
Department of Electrical Engineering
College of Engineering
University of South Florida

Major Professor: Zhixin Miao, Ph.D.
Lingling Fan, Ph.D.
Hantao Cui, Ph.D.
Yasin Yilmaz, Ph.D.
Achilleas Kourtellis, Ph.D.

Date of Approval:
June 14, 2024

Keywords: Weak Grid, Series Compensation, EMT Modeling, Analytical Modeling, Grid Following, Grid Forming, Stability Analysis

# Dedication

This dissertation is dedicated to my mom, dad and little sister. For the countless sacrifices, the infinite patience, and the constant encouragement. I could not have done this without you.Your unwavering support deserve honorary degrees!

# Acknowledgments

Firstly, I would like to extend my deepest gratitude to my advisor, Dr. Zhixin Miao, for his invaluable guidance, unwavering support, and insightful critiques throughout my doctoral journey at the Smart Grid Power Systems Lab at the University of South Florida. Your expertise and encouragement were crucial in shaping both the direction and execution of this work.

Furthermore, I owe a special debt of gratitude to Professor Lingling Fan, whose expertise and timely advice were instrumental in overcoming many of the challenges I encountered. Your willingness to go above and beyond in assisting with my research, providing both academic and practical support, has been truly inspiring. Thank you for your patience, mentorship, and the profound impact you have had on my professional development.

I am also profoundly grateful to the members of my dissertation committee: Dr. Yasin Yilmaz, Dr. Hantao Cui, and Dr. Achilleas Kourtellis. Thank you for your thoughtful feedback and rigorous review of my work, which significantly contributed to the refinement of this dissertation.

I wish to express my heartfelt appreciation to my current and past lab teammates, Dr. Yin Li, Dr. Zhengyu Wang, Dr. Li Bao, Dr. Yi Zhou, Dr. Yangkun Xu, Dr. Miao Zhang, Rabi Kar, and Huazhao Ding. Working alongside such dedicated and talented individuals has greatly enriched my research experience. Thank you for your collaboration, camaraderie, and the countless hours we shared in the pursuit of knowledge. Each of you has contributed to my journey in ways that words alone cannot capture. I would also like to extend my sincere gratitude to the Department of Electrical Engineering and its dedicated staff, Diana Hamilton and Gabriela Franco. Your support and invaluable guidance have been indispensable throughout my PhD journey.

I am deeply thankful to all the students I have had the privilege to teach during my time as an Instructor-1 for EGN 3375. Your active engagement and feedback have not only enriched

the learning environment but have also contributed significantly to my personal and professional growth.

I will always be grateful for the unwavering support of my mom, dad and little sister. Their boundless love and encouragement have been my pillars of strength, guiding me through every challenge and triumph. A special shout out to my friends, Utkarsh Misra, Shivani Sharma, Dr. Priyanka Shiveshwarkar, and Sam Brown. Your friendship has been a source of joy and strength, making even the toughest challenges seem surmountable. I also want to express my gratitude to my friend Anshuman Singh from undergraduate school. Your understanding and motivation have been invaluable to me. Thank you for always being there, offering support and encouragement when I needed it most.

## Table of Contents

# List of Tables

# List of Figures

# Abstract

This dissertation explores the stability challenges posed by integrating Inverter-Based Resources (IBR) into power grids, particularly focusing on two major scenarios: IBRs connected to weak grid interconnections and their performance in series compensated networks. With the increasing dependency on renewable energy sources, ensuring the stability of these grids is crucial. A multilayered investigative approach is employed, utilizing Electromagnetic Transient Simulations that model grid systems interfaced with IBRs. These simulations are pivotal as they emulate real-world stability issues and provide a foundational understanding of grid interactions. In this dissertation two major types of IBR control are modeled and analyzed: Grid Following Control and the Grid Forming Controls.

To delve deeper into these challenges, a non-linear analytical model is developed, pinpointing the underlying causes of the identified stability issues. This phase involves conducting various stability studies, including eigenvalue analysis and Bode diagrams, significantly enhancing the understanding of system dynamics and their implications for grid stability. Hardware simulations also play a crucial role, bridging the gap between theoretical models and real-world applications, thus confirming the viability of the proposed solutions.

Additionally, this dissertation introduces a novel coordination and control scheme for multiple IBRs operating in weak grids. This scheme enhances stability margins by modulating reactive current among the IBRs, as demonstrated through rigorous EMT simulations and validated in hardware testbeds. The results show that strategic coordination significantly improves both small-signal and large-signal stability.

Furthermore, a state-of-the-art digital twin framework using a re configurable System-on-Chip dynamically models and analyzes the IBR-grid interface. Implemented on a National Instruments

real-time controller, this digital twin effectively simulates and adjusts to real-time grid disturbances, offering a sophisticated tool for proactive grid management.

This dissertation has led to one published transaction paper, six conference publications, and 2 working papers.

# Chapter 1: Introduction

## 1.1 State of the Modern Power Grid

The renewable energy landscape in North America, particularly in the United States, is rapidly evolving, with renewable sources becoming increasingly integral to the power grid. As of 2023, renewable energy sources contribute approximately 23% of all electricity in the U.S., positioning them as the second-most prevalent source after natural gas. Meanwhile, in India and China, renewable accounts for 20% and 31% of electricity generation, respectively [1].

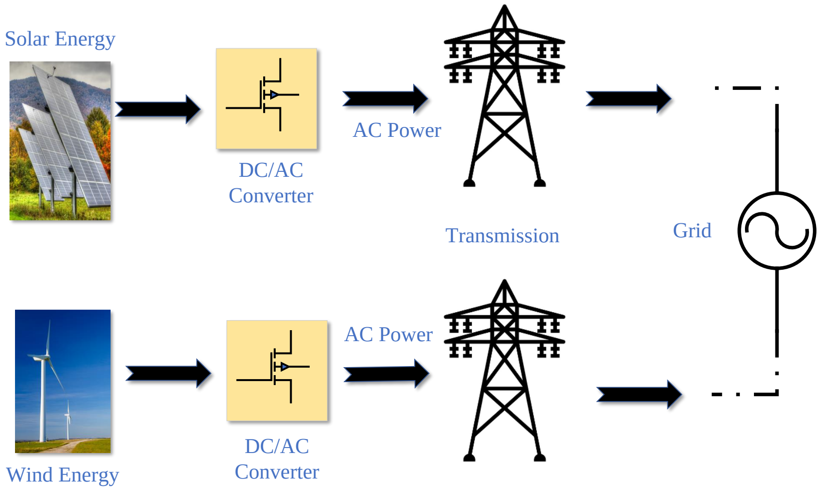

Figure 1.1 Power electronics interfaced modern power grid.

This new energy paradigm involves significant utilization of renewable sources like wind, solar, and hydroelectric power, which are essential within the broader electricity market. These resources primarily depend on power electronics for energy conversion [2]. Power electronics are crucial in managing the variable output from wind turbines and solar panels. For instance, in wind energy systems, power electronics convert the alternating current (AC) produced by the turbines into direct current (DC), and then back to AC to meet grid standards. Similarly, in solar energy systems, converts DC from solar panels into grid-compatible AC. These systems ensure that the electricity fed into the grid is stable and efficient, aiding in the seamless integration of renewable sources into the energy infrastructure. Typically, these power electronics-based systems in wind and solar energy setups are referred to as Inverter Based Resources (IBRs). Figure 1.1, presents a pictorial representation of a modern renewable energy network.

The integration of IBRs into power grids introduces several challenges. The task force paper by the IEEE Power & Energy Society IBR Subsynchronous Oscillation (SSO) task force [3] surveys 19 real-world SSO events linked to IBRs. These events often arise from weak grid interconnections or radial interconnections with series capacitors. Beyond oscillations, IBR operation faces numerous other challenges, such as large phase-locked-loop (PLL) angle deviations, subcycle overvoltage, and AC overcurrent, as documented in various reports [4–7]. Additionally, relay protection becomes more complex with IBRs, since traditional protection schemes may not adequately respond to the fault currents characterized by lower magnitudes and different waveforms produced by inverters [8].

## 1.2 Problem Statement Overview

Driven by the aforementioned operational challenges and issues in IBR-interfaced power grids, this dissertation aims to study the following challenges.

### 1.2.1 IBRs in Weak Grids

Traditionally, these IBR power plants are installed in remote areas far away from local load centers. These power plants are usually installed with extra-long transmission power lines and have very few synchronous generators. This configuration leads to a significant reduction in system strength. According to North American Electric Reliability Corporation [9], the system strength, or the Short Circuit Ratio (SCR), is defined as the ratio between short circuit apparent power ($S_c$)

from a short circuit fault at a given location in the power system to the rating of the inverter-based resource connected at the point of common coupling (PCC) ($S_N$) [10]:

$$SCR = \frac{S_c}{S_N} \approx \frac{1}{X_{gpu}} \tag{1.1}$$

Here, $X_{gpu}$ is the grid impedance in per unit. As per the IEEE Standard 1204-1997 [11], the SCR can be classified as:

1. $SCR > 3$ is classified as a strong grid.
2. $2 < SCR \leq 3$ is classified as a weak grid.
3. $SCR \leq 2$ is classified as a very weak grid.

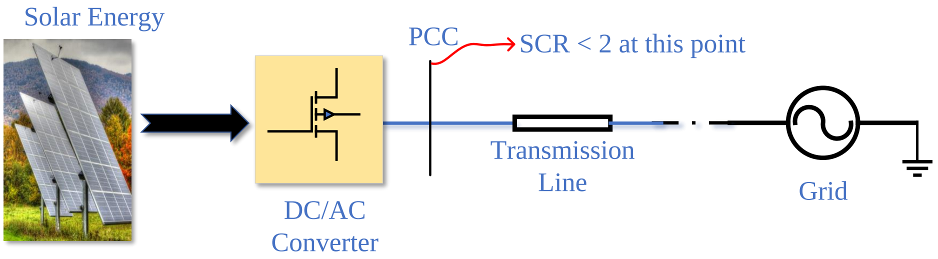

Figure 1.2 Representation of IBR connected to a weak grid.

For this dissertation, the system is assumed to be operating in a very weak grid scenario. Some of the real-world stability issues related to the operation of IBRs in weak grids are [3]:

1. 30 Hz oscillation event in West China, which occurred in 2015. The power plant consisted of Type-4 wind power plants connected via a very long transmission line, making it a weak grid interconnection.
2. 9 Hz oscillation event in 2019 in an offshore wind power plant in Great Britain. The critical reason was poor control system parameters.

3. The Australian Energy Market Operator observed 7 Hz oscillations in 2019. The IBR penetration was high, and the system strength was too low.

4. 2011 4 Hz oscillations occurred when the 138 kV transmission line was out for maintenance, the SCR reduced below 2, and the system experienced undamped oscillations.

Generally, these oscillations are called Subsynchronous Oscillations (SSOs). Over the years, weak grid SSOs have been extensively investigated [12–17]. To summarize the findings from the existing literature, the main reasons are poor control parameters and control system interactions, etc.

Furthermore, weak grid issues also have been defined as steady-state voltage stability issues due to the sensitivity of change in voltage due to power injection [9]. Figure 1.2, presents a system connected to weak grid.

### 1.2.2 IBRs in Series Compensated Networks

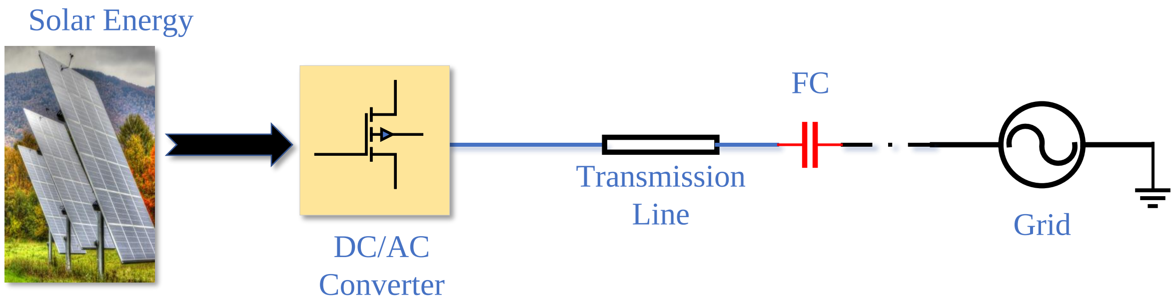

Figure 1.3 Representation of IBR connected to series compensated network.

Another stability issue arises when the IBR power plants are connected to series compensated networks (Figure 1.3). Fixed Series Compensated (FC) networks are pivotal in enhancing the efficiency and stability of long-distance electrical power transmission. These networks involve integrating capacitors in series with power lines, effectively reducing the overall line impedance. The primary objective is to augment transmission capacity and ensure voltage stability across extensive networks, thus enabling increased power flow through the existing infrastructure without necessitating new line constructions. Historically, this method has introduced several stability issues [3]:

1. 9.44 Hz SSO in Minnesota (2007): An overcurrent event occurred where the current magnitude escalated from 100 A to 1000 A within a 0.3-second interval. This was attributed to the installation of 60% series compensation in the network.

2. 20-30 Hz SSO occurrences in Texas during 2009 and 2017: The primary cause was identified as the total installation of 50% series compensation, implemented in two stages.

These types of SSOs are also referred to as Subsynchronous Resonance (SSR). The critical reason behind the SSR instability is mainly due to the introduction of LC resonance. Over time, extensive research has delved into the primary causes of SSRs in Type-3 wind turbines linked to series compensated networks, as evidenced by numerous studies. Studies such as [18, 19] have identified Induction Generator Effect (IGE) as the principal factor driving SSO, rather than torsional interactions.

## 1.3 Research Approach

The stability issues highlighted earlier pose significant challenges to power grids interfaced with Inverter-Based Resources (IBRs). This dissertation adopts a multilayered approach to investigate these challenges:

1. Initially, the grid systems interfaced with IBRs are modeled using Electromagnetic Transient Simulations (EMT). These simulations emulate real-world stability issues by incorporating certain assumptions to focus on critical dynamics.

2. Secondly, a non-linear analytical model is developed to pinpoint the underlying causes of stability issues identified in the EMT simulations. This step facilitates various stability studies, including eigenvalue analysis and Bode diagrams, enhancing the understanding of system dynamics.

3. Third, hardware simulations are conducted to bridge the gap between software simulations and real-world applications, ensuring that findings are practically viable.

4. Lastly, the research proposes mitigation strategies for addressing SSOs, thereby enhancing grid stability.

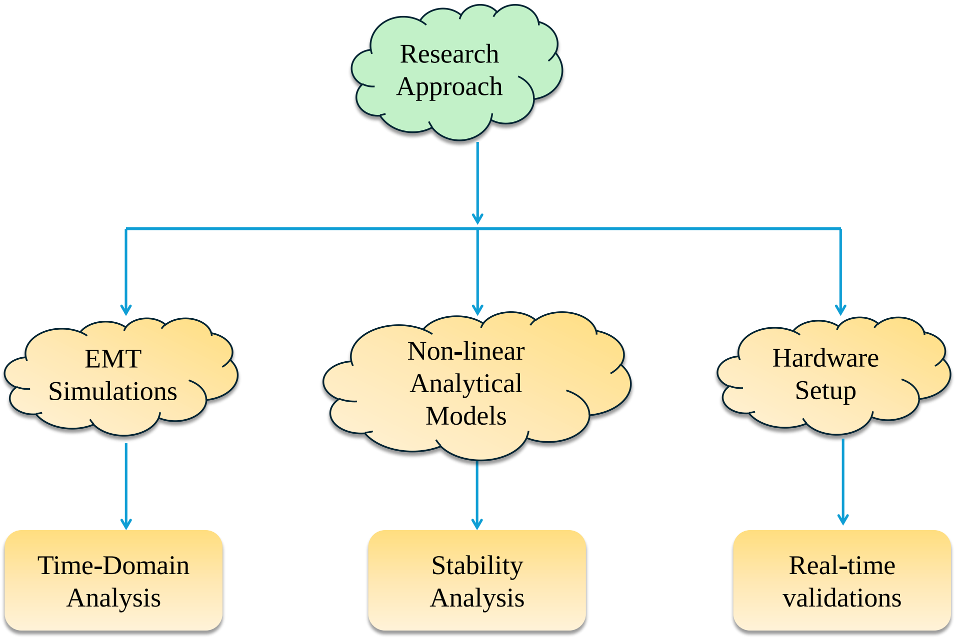

Figure 1.4 Visual summary of the research strategy utilized in this dissertation.

A pictorial representation of the research approach adopted is presented in Figure 1.4.

## 1.4 List of Publications

1. R. Mittal, Z. Miao, and L. Fan, *Stability Enhancement for IBRs Operating in Weak Grids Through Proper Coordination and Control*, accepted, to appear in IEEE Transactions on Energy Conversion.

2. R. Mittal and Z. Miao, *Analytical Model of A Grid-Forming Inverter,* 2022 IEEE Power and Energy Society General Meeting (PESGM)

3. R. Mittal, Z. Miao, and L. Fan, *Grid Forming Inverter: Laboratory-Scale Hardware Test Bed Setup and Weak Grid Operation,* 2021 North American Power Symposium (NAPS), 2021.
4. R. Mittal and V. K. Jain, *Harmonic state-space model of second-order generalized integrator phase-locked loop,* 2021 IEEE Power & Energy Society General Meeting (PESGM), 2021
5. R. Mittal, L. Fan, and Z. Miao, *Fault Detection in Three Phase Power Transmission Lines, a TI Microcontroller Implementation, and a VLSI Architecture,* 2021 North American Power Symposium (NAPS), 2021.
6. R. Mittal and Z. Miao, *Linear Time-Periodic Modeling of Single-Phase Elementary Phase-Locked-Loop,* 2020 52nd North American Power Symposium (NAPS), 2021.
7. R. Mittal and V. K. Jain, *Implementing Digital Filters and DSP Micro-Controller for Estimating the Frequency of a Time-Domain Signal,* SoutheastCon 2021.
8. R. Mittal, Z. Miao, and L. Fan, *Potential Stability Risks of Inverter-Based Resources in Series Compensated Networks*, working paper
9. R. Mittal, Z. Miao, and L. Fan, *A Digital Twin for IBR Interfaced Power System*, working paper

## 1.5 Outline of the Dissertation

The structure of the dissertation is organized as follows:

Chapter 2 presents the modeling approaches adopted in the dissertation, including Electromagnetic Transient (EMT) simulation modeling, non-linear modeling, and hardware testbeds. It also details the fundamentals and types of IBR control systems extensively.

Chapter 3 discusses the performance of IBRs under weak grid conditions. Using a dual IBR-connected grid model, this chapter explores the phenomenon of weak grids and identifies critical factors influencing stability. Additionally, it introduces stability enhancement techniques aimed at mitigating undesired oscillations in weak grid scenarios.

Chapter 4 examines the performance of IBRs when connected to a series compensated networks. Various IBR controls are modeled and analyzed using both EMT simulations and non-linear models. This chapter also includes stability analyses utilizing eigenvalues and Bode diagrams to evaluate the efficacy of these controls.

Chapter 5 explores the development of a digital twin for the IBR power system network. A modified IEEE-9 bus system serves as the basis for this digital twin, which estimates critical power grid parameters and simulates the IBR power plant in real-time, adapting to changes in actual grid conditions.

Chapter 6 presents the conclusions and outlines future research directions.

# Chapter 2: Strategies for Modeling and Analysis

This chapter[1] concentrates on the IBR controls, modeling, and tools utilized to analyze the dynamic behavior of IBRs when integrated with the power grid.

## 2.1 Understanding IBR Control

The general system topology adopted in this dissertation in presented in Figure 2.1.

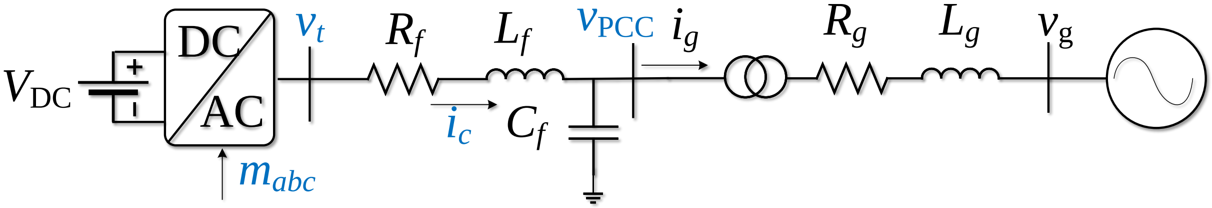

Figure 2.1 System topology used in the dissertation.

The system consists of a three-phase DC-AC inverter (IBR) connected to the power grid via a transmission lines represented by $R_g$ and $L_g$. A choke filter is connected between the terminals of the inverter and the point of common coupling (PCC) bus. The choke filter is represented by $R_f$, $L_f$ and $C_f$. A constant DC voltage source supplies the inverters, and the AC grid is modeled as a constant voltage source (infinite bus). Furthermore, $i_c$ is the converter current, $v_{\text{PCC}}$ is the PCC bus voltage, and $i_g$ is the grid current.

This inverter or IBR, can assume two types of control. The first type is the grid following type (GFL) and the second is the grid forming type (GFM). In this dissertation both types of controls are modeled and analyzed. Fundamentally, GFL control makes the IBR act like a controllable current

---

[1] Much of the content in this chapter has been previously published in IEEE Transactions on Energy Conversion [20], North American Power Symposium, and PESGM [21], [22]. Permissions for reuse are provided in Appendix A.

source, while GFM forces the IBR to dance like a controllable voltage source. Figure 2.2, presents the basic circuit representation of GFL and GFM type of IBRs.

### 2.1.1 Synchronization Unit

When integrated with the power grid, a synchronization unit is essential. This unit delivers crucial information on the phase angle and frequency of the incoming AC signal. It enables IBR to function in synchronism with the grid by supplying the necessary angle and frequency details of the three-phase input. In a GFL type of IBR, this synchronization task is managed by a PLL, whereas in a GFM type, droop control serves as the synchronizing mechanism.

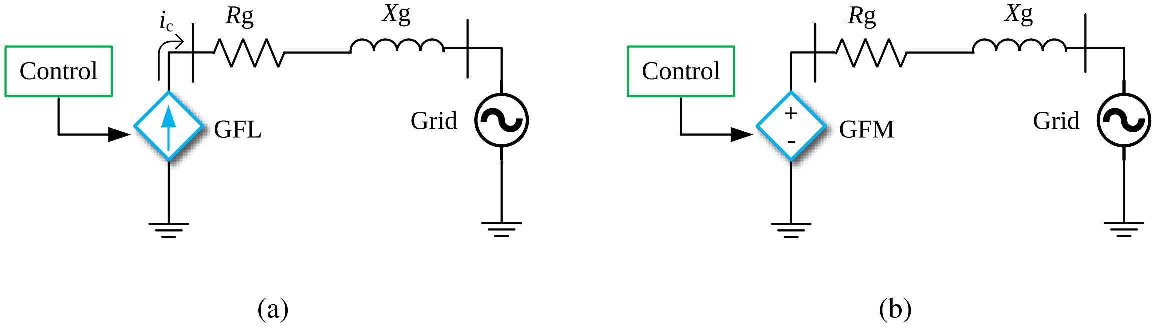

Figure 2.2 Types of IBR control. (a) GFL. (b) GFM

Additionally, the synchronization unit provides the phase angle crucial for other control aspects. This phase angle output facilitates the conversion of the sinusoidal voltage and current signals into a synchronous reference frame or *dq* frame, according to Park's transformation.

### *2.1.1.1 Park's Transformation*

To understand Park's transformation [2, 23], let's assume the three-phase PCC bus voltage is:

$$\begin{aligned} v_{\mathrm{PCC},a}(t) &= V\cos(\omega t+\theta_0) \\ v_{\mathrm{PCC},b}(t) &= V\cos(\omega t-120^\circ+\theta_0) \\ v_{\mathrm{PCC},c}(t) &= V\cos(\omega t+120^\circ+\theta_0) \end{aligned} \tag{2.1}$$

Here, $V$ is the magnitude, $\omega$ is the frequency in rad/s, and $\theta_0$ is the initial phase angle. For this balanced three-phase PCC voltage, the space vector can be described as:

$$\vec{v}_{\mathrm{PCC}} = \frac{2}{3}\left(v_{\mathrm{PCC},a}+v_{\mathrm{PCC},b}e^{j120^\circ}+v_{\mathrm{PCC},c}e^{-j120^\circ}\right) = Ve^{j\theta_0}e^{j\omega t} \tag{2.2}$$

The space vector in (2.2) rotates at a constant angular velocity of $\omega$. To view the space vector in the $dq$ frame (Figure 2.3), we can subtract the angle $\omega t$, thus obtaining the following (assuming $d+jq$ frame):

$$\frac{2}{3}\left(v_{\mathrm{PCC},a}+v_{\mathrm{PCC},b}e^{j120^\circ}+v_{\mathrm{PCC},c}e^{-j120^\circ}\right)e^{-j\omega t} = v_{\mathrm{PCC}d}+jv_{\mathrm{PCC}q} \tag{2.3}$$

Separating the real and imaginary parts:

$$\begin{bmatrix} v_{\mathrm{PCC}d} \\ v_{\mathrm{PCC}q} \end{bmatrix} = \frac{2}{3}\begin{bmatrix} \cos(\omega t) & \cos(\omega t-120^\circ) & \cos(\omega t+120^\circ) \\ -\sin(\omega t) & -\sin(\omega t-120^\circ) & -\sin(\omega t+120^\circ) \end{bmatrix}\begin{bmatrix} v_{\mathrm{PCC},a} \\ v_{\mathrm{PCC},b} \\ v_{\mathrm{PCC},c} \end{bmatrix} \tag{2.4}$$

For $\theta_0 = 0$ and $V$ as 1, we get $v_{\mathrm{PCC}d}$ as 1, and $v_{\mathrm{PCC}q}$ as 0.

This transformation changes sinusoidal and time-varying variables into simpler, DC-like quantities, making it easier to handle and control. This simplification is particularly useful in designing control systems and algorithms for electrical machines, allowing for more straightforward and efficient implementations. The function of the synchronization unit is to provide the angle "$\omega t$" for the transformations.

### 2.1.1.2 Phase-Locked-Loop

In this dissertation, the synchronous reference frame (SRF)-PLL, which is widely used, is adopted. The SRF-PLL includes an *abc* to *dq* conversion block (Park's transformation) and a PI controller. The input is three-phase PCC bus voltage $v_{\mathrm{PCC}abc}$. The purpose of the PI controller is to regulate the $v_{\mathrm{PCC}q}$ signal to zero in steady state. The control block diagram is shown in Figure 2.4.

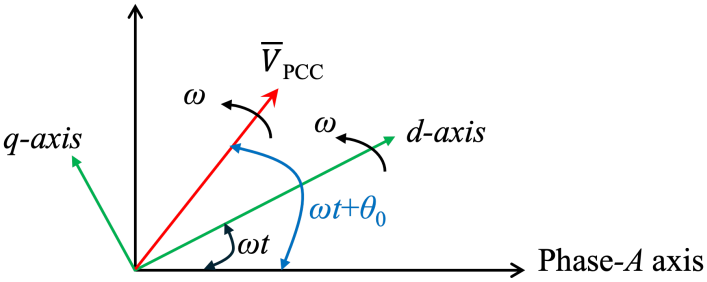

Figure 2.3 Space vector representation of *abc* to *dq* frame transformation.

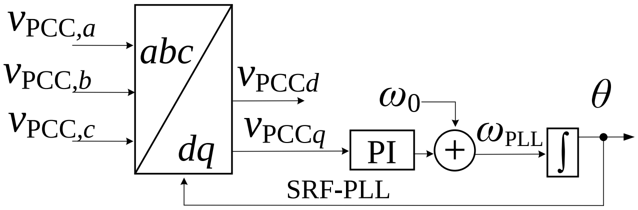

Figure 2.4 SRF-PLL used in GFL control.

For a GFL type of IBR control, which requires grid angle and frequency information for grid connection, the PLL is a critical component of the control structure. Other types of PLLs used in IBR control systems include the Decoupled Double Synchronous Reference Frame PLL and the Double Second-Order Generalized Integrator FLL [24].

#### 2.1.1.3 *Power Synchronization*

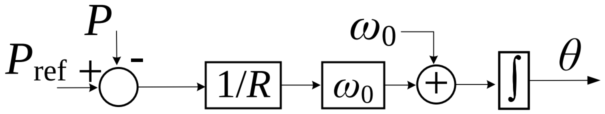

Figure 2.5 Power synchronization used in GFM control.

On the other hand, for GFM technology, the synchronization unit commonly used is frequency active power droop control. Here, the real power deviation generates the frequency deviation. The relationship is linear and is governed by the droop coefficient. Figure 2.5 presents a conventional droop control. Here, $P_{\text{ref}}$ is the real power reference, $R$ is the droop coefficient. Other types of strategies include Virtual Synchronous Machines (VSM) and Virtual Oscillator Control (VOC) [25].

### 2.1.2 Cascaded *dq* Frame Control

Establishing the role of the synchronization unit, this section details the multilayered control used to in IBRs. The second aspect of the IBR control is the main controller. This control may or may not be multi-layered. The majority of the time the fast inner loop is the current controller (tightly regulating the IBR's current), and the outer loop is a slow real power (P) and voltage control or reactive power control. The controllers can be implemented using PI controllers (tracking a DC signal), or PR controllers (proportional resonant controller) tracking an AC signal. In this dissertation, PI controllers are used. With the help of a synchronization unit, the AC signals are converted to constant dq frame variables.

For GFM control, the inner loop is similar to the GFL type, but the outer loop is different, where the outer loop controls the voltage magnitude [26]. The output of the control algorithm is the reference signals ($m_{abc}$) for the converters. Furthermore, the real power $P$ and the reactive power $Q$ are given by:

$$\begin{aligned} P &= v_{\mathrm{PCC}d}\, i_{cd} + v_{\mathrm{PCC}q}\, i_{cq} \\ Q &= v_{\mathrm{PCC}q}\, i_{cd} - v_{\mathrm{PCC}d}\, i_{cq} \end{aligned} \tag{2.5}$$

Here, $v_{\mathrm{PCC}d}$ and $v_{\mathrm{PCC}q}$ are the $dq$ components of $v_{\mathrm{PCC}}$. The magnitude of the PCC bus voltage is obtained as:

$$|V_{\mathrm{PCC}}| = \sqrt{v_{\mathrm{PCC}d}^2 + v_{\mathrm{PCC}q}^2} \tag{2.6}$$

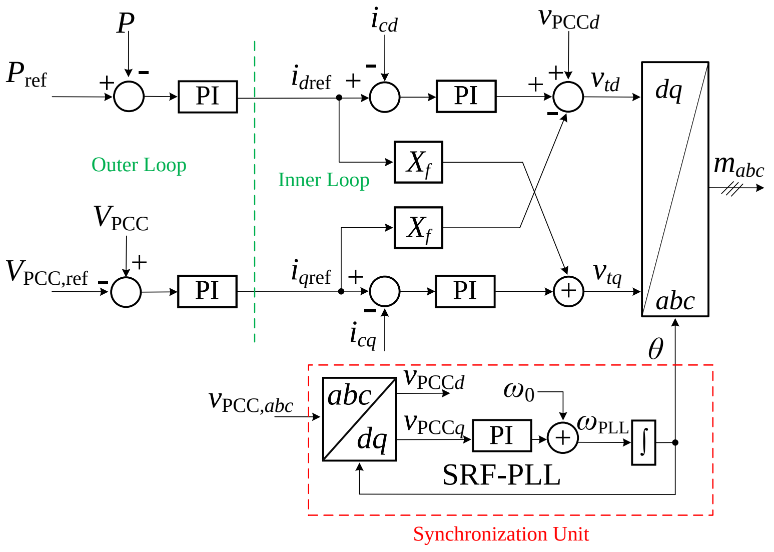

Figure 2.6 Control structure for GFl IBR.

Figure 2.6 and Figure 2.7 presents a block diagram of GFL an GFM control.

## 2.2 Tools

Three tools are utilized for modeling and studying the dynamics of grid-connected Inverter-Based Resources (IBRs): (a) Electromagnetic transient simulations, (b) Non-linear Analytical Models, and (c) Hardware-in-loop simulations.

### 2.2.1 Electromagnetic Transient (EMT) Simulations

EMT simulations are computational methods used to analyze the behavior of power systems during transient events like sudden load changes and fault conditions. These simulations offer a precise dynamic model of a power system network, encompassing components such as power electronic devices, transmission lines, transformers, and generators. Key EMT simulation software includes PSCAD/EMTDC, MATLAB/Simscape Electrical, and EMTP-RV, among others. For this dissertation research MATLAB/Simscape Electrical package has been adopted. MATLAB/Simscape Electrical is a specialized toolbox for modeling and simulating electrical systems. The GUI consists of power electronic devices, machines, sensors, and other passive components. The extensive library of components helps the user to model a physical system in a graphical environment.

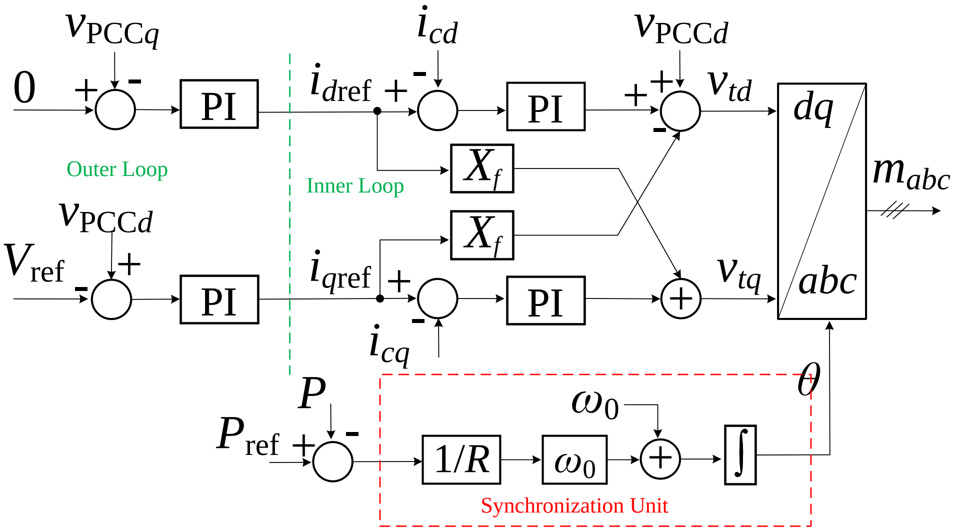

Figure 2.7 Control structure for GFM IBR.

The backbone of an IBR is power electronics-based converters. These converters can either be modeled using a detail switch model or an average model. Each approach has its own set of advantages, and the choice between them often depends on the specific requirements of the simulation, such as the level of detail needed, computational resources available, and the frequency dynamics of interest. For this dissertation work average modeling techniques have been adopted. The reasons are listed below:

1. The average model reduces the computational burden and improves the simulation speed.
2. For this dissertation the main objective is to study IBR control dynamics, fundamental system behavior, and low-frequency oscillations. The average modeling technique is excellent for these applications.

Figure 2.8 presents the MATLAB/Simscape Electrical environment, showcasing an average model of IBR connected to a grid.

### 2.2.2 Non-Linear Analytical Model

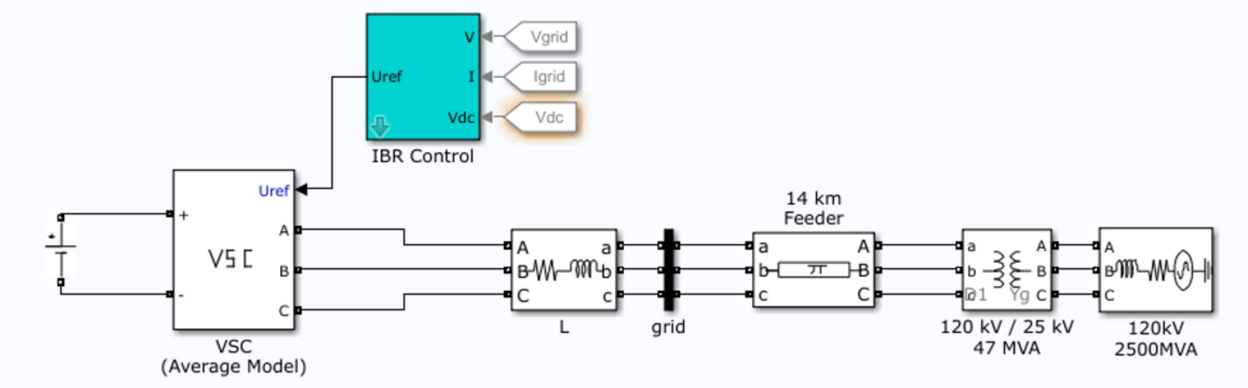

Figure 2.8 Average model of IBR connected to the power grid.

Although EMT models offer precise time-domain insights into IBR networks, they often don’t provide clear explanations for the observed dynamic behaviors. To bridge this gap, nonlinear analytical models are developed. These models account for the nonlinear relationships between system variables using mathematical representations and simulations. The modeling involves first-order differential equations that establish state-space equations as follows:

$$\begin{aligned} \frac{dx}{dt} &= Ax + Bu \\ y &= Cx + Du \end{aligned} \tag{2.7}$$

Here, $x$ is a matrix that includes the state variables, and $u$ is the input. $A$, $B$, $C$, and $D$ are the matrices, defining relationships between the system's inputs, outputs, and internal state.

State-space modeling not only provides results in the time domain but also serves as a powerful tool for conducting modal analysis [27], including eigenvalue analysis, mode shapes, and participation factors. Additionally, nonlinear models facilitate frequency domain analysis using techniques such as Bode diagrams or root locus methods.

As an example, the analytical model building for the GFL type of IBR is presented below. For building the analytical model Figure 2.1, and Figure 2.6 are used.

### 2.2.3 Analytical Model for GFL

The system presented in Figure 2.1 is modeled with four main blocks: a synchronization unit (PLL), inner and outer control, circuit dynamics, and frame conversion, as shown in Figure 2.9. It is noted that, while the signals at the circuit level are based on the grid frame (superscript **g**, rotating at the nominal frequency of $\omega_0$), the signals associated with the control structure are based on the frame or angle provided by the synchronization unit.

The state variables are described as follows: the grid-frame variables associated with circuit dynamics, including the converter current $i^g_{cdq}$, the PCC bus voltage $v^g_{\mathrm{PCC}dq}$, the grid current $i^g_{gdq}$, and the series capacitor voltage $v^g_{dq}$ (circuit dynamics), synchronizing-frame states representing the outer loop PI controllers $x_1$ ($d$-axis) and $x_2$ ($q$-axis) and inner current controls $x_3$ and $x_4$. In the GFL-IBR, the PLL incorporates two state variables: $\Delta\omega$ (associated with the PI controller) and $\Delta\theta$. Consequently, the GFL-IBR testbed comprises 12 state variables.

### 2.2.3.1 Circuit Dynamics

The analytical model of the circuit dynamics is developed in the grid $dq$ frame that rotates at a speed of $\omega_0$. The differential equations for the RLC circuit dynamics are presented as follows:

$$
\begin{aligned}
\frac{di^g_{gd}}{dt} &= -\frac{R_g}{L_g} i^g_{gd} + \frac{1}{L_g} v^g_d - \frac{1}{L_{g1}} v^g_{gd} + \omega_0 i^g_{gq} \\
\frac{di^g_{gq}}{dt} &= -\frac{R_g}{L_g} i^g_{gq} + \frac{1}{L_{g1}} v^g_q - \frac{1}{L_g} v^g_{gq} - \omega_0 i^g_{gd} \\
\frac{di^g_{cd}}{dt} &= -\frac{R_f}{L_f} i^g_{cd} + \frac{1}{L_f} v^g_{td} - \frac{1}{L_f} v^g_d + \omega_0 i^g_{cq} \\
\frac{di^g_{cq}}{dt} &= -\frac{R_f}{L_f} i^g_{cq} + \frac{1}{L_f} v^g_{tq} - \frac{1}{L_f} v^g_q - \omega_0 i^g_{cd} \\
\frac{dv^g_{\mathrm{PCC}d}}{dt} &= \frac{1}{C_f}(i^g_{cd} - i^g_{gd}) + \omega_0 v^g_{\mathrm{PCC}q} \\
\frac{dv^g_{\mathrm{PCC}q}}{dt} &= \frac{1}{C_f}(i^g_{cq} - i^g_{gq}) - \omega_0 v^g_{\mathrm{PCC}d}
\end{aligned}
\tag{2.8}
$$

Here $R_f$, $X_f$, and $B_f$ are the per-unit values of the $RLC$ components of the choke filter and $L_f = X_f/\omega_0$, $C_f = B_f/\omega_0$. Similarly, $R_g$, $X_g$ , and $B_g$ are the per-unit values of the transmission line parameters and $L_g = X_g/\omega_0$, $C_g = B_g/\omega_0$. This block has $v^g_{td}$ and $v^g_{tq}$ (the $dq$ components of the converter terminal voltage $v_t$) and the grid voltage $v^g_{gd}$, $v^g_{gq}$ as input and outputs the converter current, PCC bus voltage, real and reactive power. .

### 2.2.3.2 SRF-PLL

The synchronization unit in testbed-1's GFL-IBR is PLL. For this paper, we have adopted a second-order PLL. The $dq$ frame analytical model of the PLL is adapted from the work presented in [14].

### 2.2.3.3 Frame Conversion

As previously mentioned, the control system operates in a distinct reference frame (angle $\theta$) provided by the synchronization unit, which is a PLL for GFL IBR. The converter control regulates the $dq$ components of converter current $i_c$ and the voltage at the PCC bus $v_{\mathrm{PCC}}$ in the control frame. Due to the different reference frames adopted for the circuit model and the control, appropriate frame conversion is essential for accurate modeling.

The relationship between the grid frame and the control frame can be found by relating the space vector of current or voltage with its grid frame-based and control frame-based vectors. For example, the PCC bus voltage's space vector $\vec{v}_{\mathrm{PCC}}$ can be related to the grid-frame variables and the control-frame variables as follows:

$$\begin{aligned} &\vec{v}_{\mathrm{PCC}} = (v_{\mathrm{PCC}d} + j\,v_{\mathrm{PCC}q})e^{j\theta} = (v^g_{\mathrm{PCC}d} + j\,v^g_{\mathrm{PCC}q})\,e^{j\omega_0 t} \\ &\Longrightarrow (v_{\mathrm{PCC}d} + j\,v_{\mathrm{PCC}q})e^{\Delta\theta} = v^g_{\mathrm{PCC}d} + j\,v^g_{\mathrm{PCC}q}, \end{aligned} \tag{2.9}$$

where $\Delta\theta = \theta - \omega_0 t$. From (2.9), it can be seen that signals in the grid frame can be transformed to the synchronization frame and vice-versa. The complete analytical model is presented in Figure 2.9.

#### *2.2.3.4 Model Initialization*

A proper initialization procedure is needed to develop the analytical model accurately. The initialization is done using power flow in the phasor domain. The complex power at the PCC bus is given: $S = V_{\mathrm{PCC}} I_c{}^*$, where $V_{\mathrm{PCC}}$ is the PCC bus voltage and $I_c$ is the current through the filter inductor in phasors. The real power is: $P$ = real($S$), and the reactive power is: $Q$ = imag($Q$). The PCC bus voltage phasor is defined as $V_{PCC}$ = $|V_{\mathrm{PCC}}|\underline{/\theta}$ and the current $I_c$ is obtained as:

$$I_g = \frac{V_{PCC} - V_g}{R_{g\mathrm{pu}} + i X_{g\mathrm{pu}}}, \quad I_{Cf} = \frac{V_{\mathrm{PCC}}}{-i X_{C\mathrm{pu}}}, \; I_c = I_g + I_{Cf} \tag{2.10}$$

Here, $I_g$ is the current in the transmission line, $I_{Cf}$ is the current through the filter capacitor $C_f$, and $V_g$ = 1. If implemented in $P\,V_{PCC}$ control, the constraints are $P == P_{\mathrm{ref}}$ and $|V_{\mathrm{PCC}}| == V_{\mathrm{PCC,ref}}$. Here, $P_{\mathrm{ref}}$ and $V_{\mathrm{PCC,ref}}$ are the desired operating conditions at the PCC bus. This problem is solved using YALMIP [28]. The optimization problem solves for the value of $Q$ and $\theta$. Given $P$, $Q$, $|V_{\text{PCC}}|$, and $\theta$, the state variables are calculated for initialization.

#### *2.2.3.5 Linear Model*

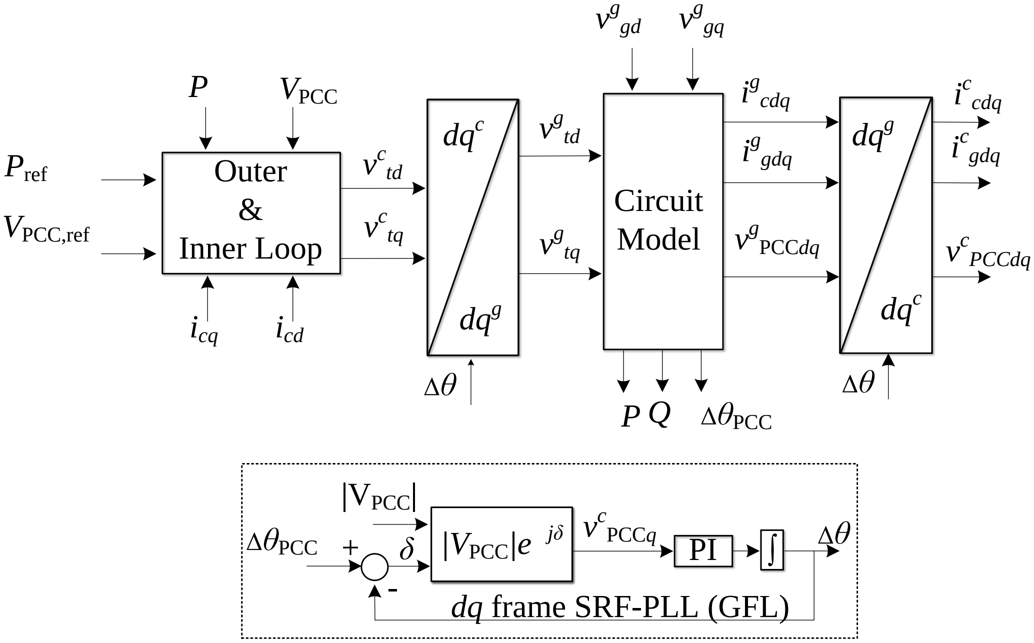

Figure 2.9 Analytical model of GFL IBR.

After initialization, we linearize the analytical model to obtain the Linear Time-Invariant (LTI) model using Jacobian linearization. We will construct the nonlinear analytical model representing the IBR. The model maintains all its state variables (12 in total) constant at steady state to enable Jacobian linearization. The LTI model is derived numerically using MATLAB's `linmod` function, extracting a continuous-time LTI model around the operating point using a block-by-block linearization algorithm [29]. This provides the state-space model as presented in (2.7).

#### *2.2.3.6 Stability Analysis*

The stability analysis of an IBR system is conducted using the state space model. This analysis is accomplished through two methods. The first method involves evaluating "Eigenvalues".

Eigenvalue analysis in the state-space model is a critical aspect of understanding the dynamics and stability of a system. For a state-space system, the eigenvalues of the matrix $A$ (the state matrix) are calculated by:

$$\det(A - \lambda I) = 0 \tag{2.11}$$

where $I$ is the identity matrix and $\lambda$ represents the eigenvalues. In MATLAB, this is achieved by invoking the `eig(A)` function. Eigenvalues are crucial for assessing the stability and dynamics of the system. The eigenvalues are complex numbers where the real part indicates the rate of exponential decay or growth, and the imaginary part (if present) indicates oscillatory behavior with a frequency proportional to the magnitude of the imaginary part. From a stability perspective, if all eigenvalues are in the left half of the complex plane, the system is considered stable. If any eigenvalues lie in the right half of the plane, the system is unstable. Eigenvalues on the imaginary axis indicate marginal stability. Another tool used to analyze the stability of the system is the Bode diagram. A Bode diagram, or Bode plot, is a graphical representation of a linear, time-invariant system's frequency response. It consists of two plots: the magnitude plot (in dB scale) and the phase plot. Stability can be analyzed by evaluating the gain margins and phase margins. Figure 2.10 provides the summary of the non-linear analytical model building.

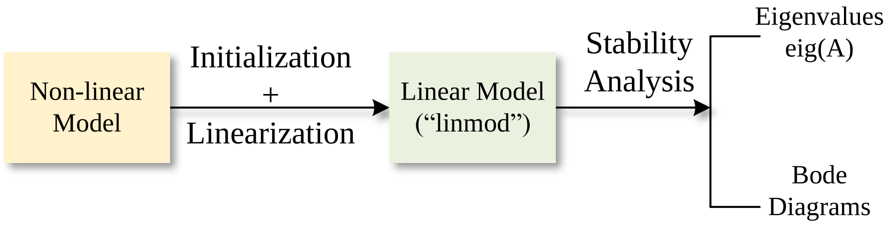

Figure 2.10 Summary of non-linear analytical model building and stability analysis using MATLAB.

### 2.2.4 Hardware-in-Loop Simulations

Hardware-in-loop (HIL) simulations are powerful power system technique that combines real hardware components into a simulation loop to simulate real-time interactions between the hardware and a virtual model. Some common types of HIL simulations are Power HIL (P-HIL), component-HIL (C-HIL), etc. In this dissertation, P-HIL simulations are adopted to study the real-time behavior of power electronics converters integrated into power grids.

A laboratory-scale P-HIL is established. It comprises of a real-time simulator (OP5607), power converters (Imperix Modules), a grid emulator (Chroma 61845), sensors and other passive elements. A sample example of an established P-HIL testbed is presented in Figure 2.11. The hardware components are explained as follows.

1. DC Power Supply: The DC voltage is provided to the VSC system with the help of BK Precision DC regulated power supply, model 1666. The maximum allowable voltage from the device is 40 V, and the current is 5 A.

2. Power Grid: The power grid source is emulated by Chroma Regenerative Grid Simulator 61845. The rated 3-phase power of the simulator is 45kVA, with a rated output voltage as 300 V( L-N). The Chroma simulator is controlled remotely with the help of LabVIEW installed on a host computer. The host computer and the simulator communicate with each other with the help of a GPIB (General Purpose Interface Bus) cable.

3. VSC system: To arrange a three-phase VSC system, Imperix's power module PEB 8024 is used. PEB 8024 is a half-bridge power module featuring two Silicon Carbide (SiC) MOSFETs switches. Three individual PEB 8024 modules are connected to make one three-phase VSC. The power module consists of onboard with DC voltage sensor and current sensors and necessary over-voltage and current protections. The MOSFETs receive the gating pulses via an optic fiber connection.

4. Analog Sensor Units: The onboard current sensors embedded on the imperix power modules measure the three-phase current flowing in the filter inductors. The voltage at the PCC bus and the current flowing in the load are measured by Opal RT's OP8662, a high voltage and current measurement unit.

5. Real-Time Controller: Opal RT's OP5607 acts as a real-time controller. The OP5607 acquires all the measured analog signals from different sensor units. The control algorithm is implemented and executed in OP5607 with the help of RT-Lab. The controller outputs the required PWM signals using digital out channels.

6. Power Interface: Opal RT's power interface allows to control of the imperix power modules with OP5607. The PWM signals generated by OP5607 are fed to the power interface and are relayed to the imperix's power modules with the help of optic fiber cables.

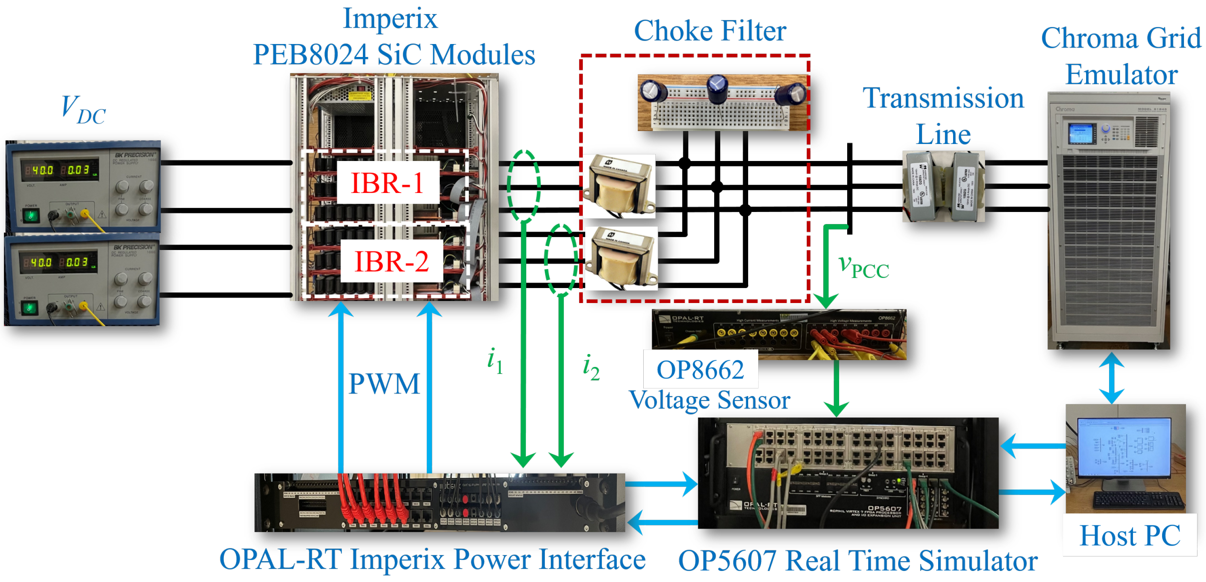

Figure 2.11 Laboratory scale P-HIL testbed to study IBR connected to grid.

# Chapter 3: Performance of IBRs in Weak Grid Connection and Stability Enhancement

In this chapter[2], the analysis focuses on multiple Inverter-Based Resources (IBRs) connected to a weak grid interconnection. The discussion encompasses the dynamic performance of IBRs within this weak grid context, explores the critical factors influencing their performance, and proposes a stability enhancement technique designed to mitigate oscillations and enhance overall system performance.

## 3.1 Introduction

High penetrations of IBRs have been reported in South Australia, Hawaii, Texas, Colorado, Denmark, etc. [30] As a consequence, weak grid oscillation events appeared in real-world operation [31]. In Texas, an ERCOT wind power plant experienced 4-Hz oscillations due to weak grid conditions after a line tripping event [32]. Solar photovoltaic (PV) plants in Hydro One experienced undamped 20 Hz oscillations [33]. Australian Energy Market Operator (AEMO) witnessed 7-Hz oscillations due to a lack of system strength in the west Murray region [34]. These oscillations were identified to be associated with multiple solar farms. More examples of real-world weak grid oscillation events are well documented in the recently published IEEE PES IBR subsynchronous oscillations task force papers [35, 36].

### 3.1.1 Literature Review

Over the years, weak grid stability enhancement methods for grid-following voltage-sourced converter (VSC)-based IBRs have been discussed and reported. These methods can be classified

---

[2] The majority of this chapter has been published in IEEE Transactions on Energy Conversion [20]. Permissions are included in Appendix A.

into three categories: those dealing with phase-locked loops (PLLs), those dealing with inner current controls, and those dealing with outer controls.

It has been known that PLL introduces negative resistance in the low-frequency region in the dq frame [37]. Thus, redesign PLL or tuning PLL parameters have been an active research. In [37], the authors suggest reducing the bandwidth of the PLL to reduce the effect of the negative resistance. Most recently, in [38], the authors propose a double-PLL-based scheme to extend the stability region of the VSC system while operating in very weak grid conditions with the short circuit ratio (SCR) at 1. The new design leads to the VSC exporting 0.9 p.u. real power when the point of common coupling (PCC) voltage is kept at 1 p.u. A very different synchronization approach with the d-axis current as the input to generate angle has been proposed in [39] and shown to boost the stability margin close to the steady-state limit. While operating at SCR of 1 with the proposed control, the VSC-HVDC is able to transfer maximum power of 1.0 p.u. with the terminal voltage at 1.0 p.u.

Recent research indicates that the proportional gain of the inner current control influences weak grid stability [40, 41]. [40] shows that the gain has difficulty to balance the PCC voltage response and the damping capability during weak grid conditions. Thus, the authors resolved with the restructuring of the proportional integral (PI) controller as an integral proportional (IP) controller. The redesigned current control leads to a higher stability margin for the VSC. When operating at SCR of 1, it can inject up to 1 p.u. power with the PCC voltage at 1 p.u. With the effect of the voltage feedforward unit's low-pass filter considered, the proportional gain is shown to aggravate the instability impact of PLL and make weak grid stability worse [41]. The authors indicate that co-design of the current controller and the voltage feedforward controller is necessary.

Research in the third category usually treats the inverter with PLL and current control as an ideal current source, while the main weak grid stability issue is caused by the outer control. For example, in [42], the authors show that a VSC without outer control can operate up to the theoretic limit, while stability issue appears if the outer control is enabled. An advanced vector control is then proposed by adding four decoupling gains between the power and the voltage control loops.

While operating at SCR = 1, the proposed control can deliver a maximum of 0.89 p.u. real power. In [43], the authors propose to modify the power PI controller to compensate the phase lag introduced by the PLL and provide damping to low-frequency oscillations at weak grid conditions. With the suggested modification, the single grid-connected VSC was able to inject 1.0 p.u. real power when SCR is 1.1. In [44], strong coupling between real power and voltage is identified as the main cause of instability. Hence, a power-voltage decoupling scheme is designed and implemented to modulate the real power order by use of voltage deviation feedback. The single IBR can deliver 0.91 p.u. when $X_g = 1.1$ or SCR is 0.91.

### 3.1.2 Goals and Contributions

It can be seen that several designs, e.g., [39, 44], can enhance individual IBR's stability margin close to the steady-state limit. Alternatively, parameter tuning for fixed control structures can be another option for stability enhancement. However, in some scenarios, this option may not be feasible. Take the example of the Texas 4-Hz oscillations [45], oscillations appeared upon tripping of a transmission line which led to the grid strength dropped to short circuit ratio of 2. Reducing the gain in plant-level voltage control can resolve the issue of oscillation, but this tuning slows down voltage recovery. When the grid strength is high, this set of parameters is not desired. Hence, parameter tuning has to be within the design consideration. In some cases, parameter tuning is not enough for stability enhancement.

The objective of this work is to enhance stability further. The following investigation was conducted: With every IBR well-designed and tuned, is there additional room for stability improvement in a multi-IBR system through IBR coordination?

Preliminary research was carried out to determine whether IBRs operating identically in power and voltage control modes offer the best stability in a two-IBR system. The findings indicate that this is not necessarily the case. In fact, with one IBR in voltage control mode and another in reactive power control mode, the entire system can achieve better stability.

Thus, there is room for additional improvement through coordination. In this research, an effective coordination scheme will be designed, implemented, and tested. With the coordination scheme, our tests show that the total power from the two IBRs can achieve 1.06 p.u. for a very weak grid interconnection when the SCR is 1 p.u. Since there is 0.1 p.u. resistance in the grid impedance, the steady-state limit of operation (with voltage kept at 1 p.u.) is about 1.1 p.u. It is found that the coordination scheme can effectively push IBRs to operate close to the steady-state limit.

## 3.2 Testbeds

The schematics of the system under study are presented in Figure 3.1. The system consists of two three-phase DC-AC inverters connected in parallel at the PCC bus, which is further is connected to the power grid via a transmission line represented by $R_g$ and $X_g$. A choke filter is connected between the terminals of the inverter. The choke filter is represented by $R_f$, $X_f$ and $C_f$. A constant DC voltage source supplies each inverter. The AC grid is modeled as a constant voltage source ("infinite bus").

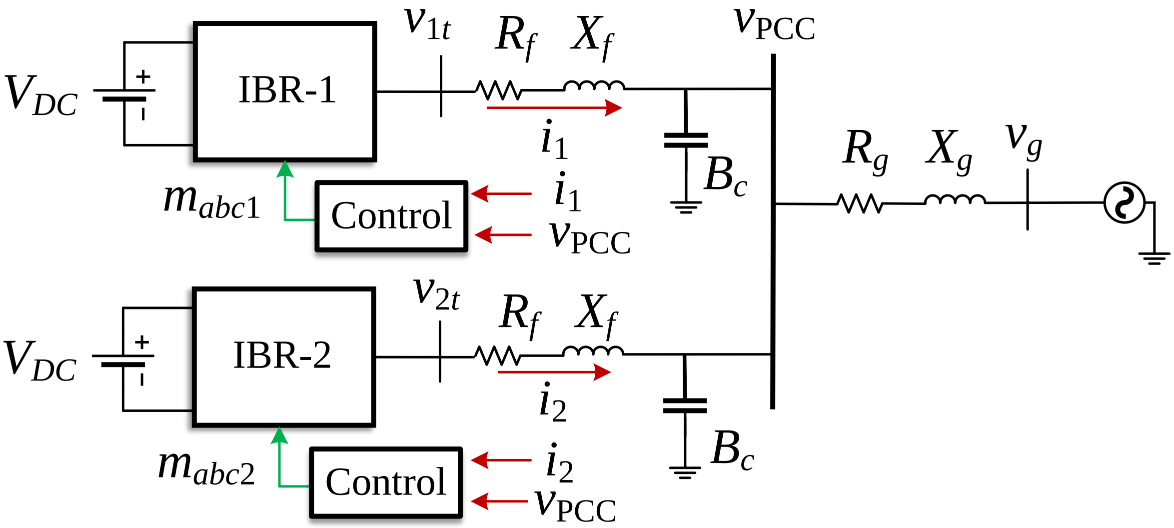

Figure 3.1 Circuit topology of the two-IBR test bed.

Furthermore, $i_1$, and $i_2$ are the converters current for IBR-1 and IBR-2 respectively and $v_{\text{PCC}}$ is the PCC bus voltage. Both the IBRs are grid-following inverters. In this work, three different testbeds are considered for the study. The main difference between the two systems is the control structure. The subscripts “1” and “2” represent IBR-1 and IBR-2 respectively.

1. Testbed-1 : In the first testbed (referred to as Testbed 1), the two IBRs have identical controls. The inner current control is implemented in the PLL-based $dq$ frame, and the outer control regulates real power $P$ and the PCC bus voltage $V_{\text{PCC}}$. The real power control generates $i_{d\text{ref}}$ for the $d$-axis current control and the voltage control generates $i_{q\text{ref}}$ for the $q$-axis current control. A synchronous reference frame-PLL is used to synchronize the PCC voltage to the grid. The output angle ($\theta$) from the PLL is used for frame conversion. The real power $P_1$ and the reactive power $Q_1$ are given by:

   $$\begin{aligned} P_1 &= v_d\, i_{1d} + v_q\, i_{1q} \\ Q_1 &= v_q\, i_{1d} - v_d\, i_{1q} \end{aligned} \tag{3.1}$$

   Here, $v_d$ and $v_q$ are the $dq$ components of $v_{\text{PCC}}$. Similarly, $P_2$ and $Q_2$ are defined. The magnitude of the PCC bus voltage is obtained as:

   $$V_{\text{PCC}} = \sqrt{v_d^2 + v_q^2} \tag{3.2}$$

   Additionally, a feed-forward filter (VFF) has been added to the feed-forward signal $v_q$ in the inner current control to enhance the system stability. The feed-forward filter is a low pass filter and the transfer function is $\frac{1}{T_{vf}\,s+1}$, where $T_{vf}$ is the cutoff frequency.

2. Testbed 2: For Testbed 2, IBR-1 and IBR-2 have different control structures for the outer control. The inner current controls are the same. For IBR-1, the $d$-axis outer control is the real power control, whereas in the $q$-axis control, the outer control is reactive power control. The reactive power order is generated from the plant-level voltage controller. For the

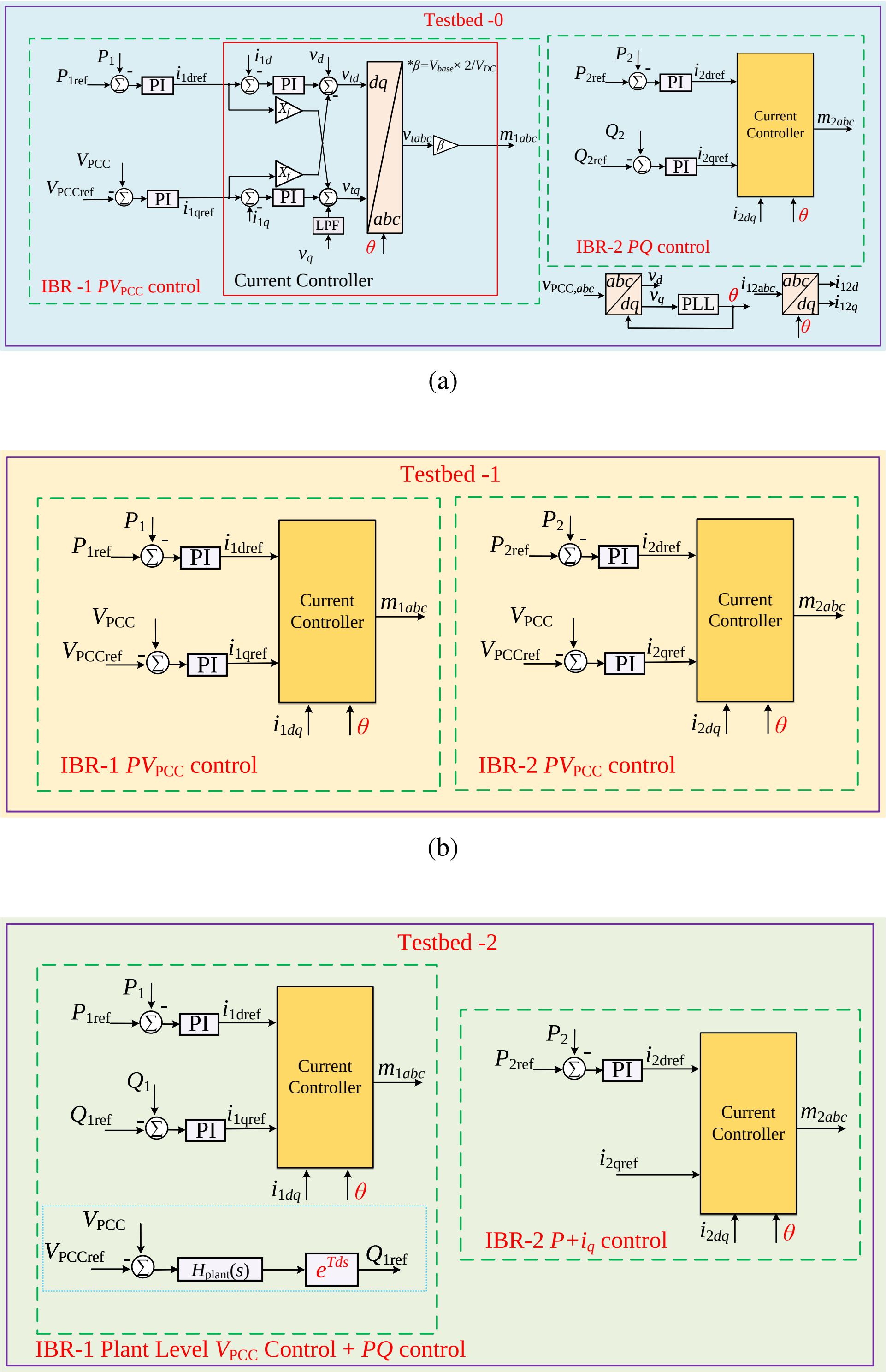

(a)

(b)

(c)

Figure 3.2 Control block diagram for testbed 0, testbed 1, and testbed 2.

plant-level control, the voltage reference order ($V_{\text{PCC,ref}}$) is compared with the measurement $V_{\text{PCC}}$ and passed through an integral controller ($\frac{k_{i\text{Plant}}}{s}$) to generate the reactive power order ($Q_{1,\text{ref}}$). Additionally, a delay ($e^{-T_d s}$) is considered for the plant-level control and inverter-level control communication. IBR-2 shares the same $d$-axis outer loop control structure as IBR-1 but does not have $q$-axis outer loop control and $i_{2,q\text{ref}}* = 0$.

3. Testbed 0: In Testbed-0, IBR-1 and IBR-2 have different outer loop controls, but the inner current control is the same. For IBR-1, the outer loop is real power $P$ and PCC bus voltage $V_{\text{PCC}}$ control, whereas IBR-2 has an outer loop in real power $P$ and reactive power $Q$ control. An SRF-PLL is implemented that synchronizes the converters to the grid. The rest of the control structure is similar to Testbed 1. The detailed controller structures of Testbed 0, Testbed 1, and Testbed 2 are presented in Figure 3.2. The parameters for Testbed 0, Testbed 1, and Testbed 2 are presented in Table. 3.1 and 3.2 . The controller gains are based on the per-unit system.

Table 3.1 Parameters of IBR power plant and control parameters for testbed 1.

| Description | Parameter | Value |
|---|---|---|
| Power Base | $S_b$ | 100 MVA |
| Voltage Base | $V_b$ | 575 V |
| Nominal Frequency | $f_0$ | 60 Hz |
| Grid Voltage | $V_g$ | 575 V |
| DC Voltage | $V_{DC}$ | 1100 V |
| Choke Filter | $X_f$ | 0.15 pu |
|  | $R_f$ | 0.003 pu |
|  | $B_c$ | 0.1 pu |
| Transmission Line Inductance | $X_g$ | 1 pu |
| Transmission Line Resistor | $R_g$ | $0.1X_g$ pu |
| Control Parameters for Testbed 1 and Testbed 0 |  |  |
| Inner Loop Control | $k_{ip}$, $k_{ii}$ | 0.3, 5 |
| Outer Loop Control, $P$ control | $k_{Pp}$, $k_{Pi}$ | 0.4, 40 |
| Outer Loop Control, $V_{\text{PCC}}$ or $Q$ | $k_{Vp}$, $k_{Vi}$ | 0.4, 40 |
| Feed-forward filter | $T_{vf}$ | 0.002 |

Table 3.2 Control parameters for testbed 2 and GFM IBR.

| Description | Parameter | Value |
|---|---|---|
| Control Parameters for Testbed 2 | | |
| Inner Loop Control | $k_{ip}$, $k_{ii}$ | 0.3, 5 |
| Outer Loop Control, $P$ control | $k_{Pp}$, $k_{Pi}$ | 0.4, 40 |
| Outer Loop Control, $V_{\text{PCC}}$ control | $k_{Vp}$, $k_{Vi}$ | 0.4, 40 |
| Feed-forward filter | $T_{vf}$ | 0.001 |
| Plant Level Control | $k_{i\text{Plant}}$ | 10 |
| Plant Level delay | $T_d$ | 5 ms |
| PLL | $k_{\text{PLL}p}$, $k_{\text{PLL}i}$ | 60, 1400 |
| Control Parameters Grid Forming IBR | | |
| Inner Loop Control | $k_{ip}$, $k_{ii}$ | 0.3, 5 |
| Outer Loop Control, | $k_{Vp}$, $k_{Vi}$ | 2, 10 |
| $Pf$ droop | $n_p$ | 0.2 |

## 3.3 Performance of IBRs in Weak Grid

The three testbeds discussed in Section II are modeled and simulated using MATLAB/Simscape Electrical. Electromagnetic Transient (EMT) simulations are conducted with the Short Circuit Ratio (SCR) set at 1.0 p.u., and the system is subjected to changes in real power orders. The results of these simulations are illustrated in Figure 3.3.

Upon exposure to changes in real power orders, the system experiences weak grid oscillations. Testbed 0 exhibits marginal stability at a real power order of 0.94 pu, with an oscillation frequency of 6 Hz. Testbed 1 demonstrates an oscillation frequency of 6.5 Hz at a power order of 0.974 pu, while Testbed 2 shows oscillations at 3.2 Hz when the power order is adjusted to 0.85 pu. These findings suggest that the stability of IBRs can significantly decline under certain operational conditions. The varied oscillation frequencies across the testbeds highlight the sensitivity of IBR systems to changes in power order within weak grid environments. Importantly, these results underscore the necessity for robust control strategies that can effectively manage and mitigate these oscillations, ensuring system stability and reliability. This simulation study clearly demonstrates that an IBR, regardless of its control structure, will experience weak grid oscillations when connected to a weak grid.

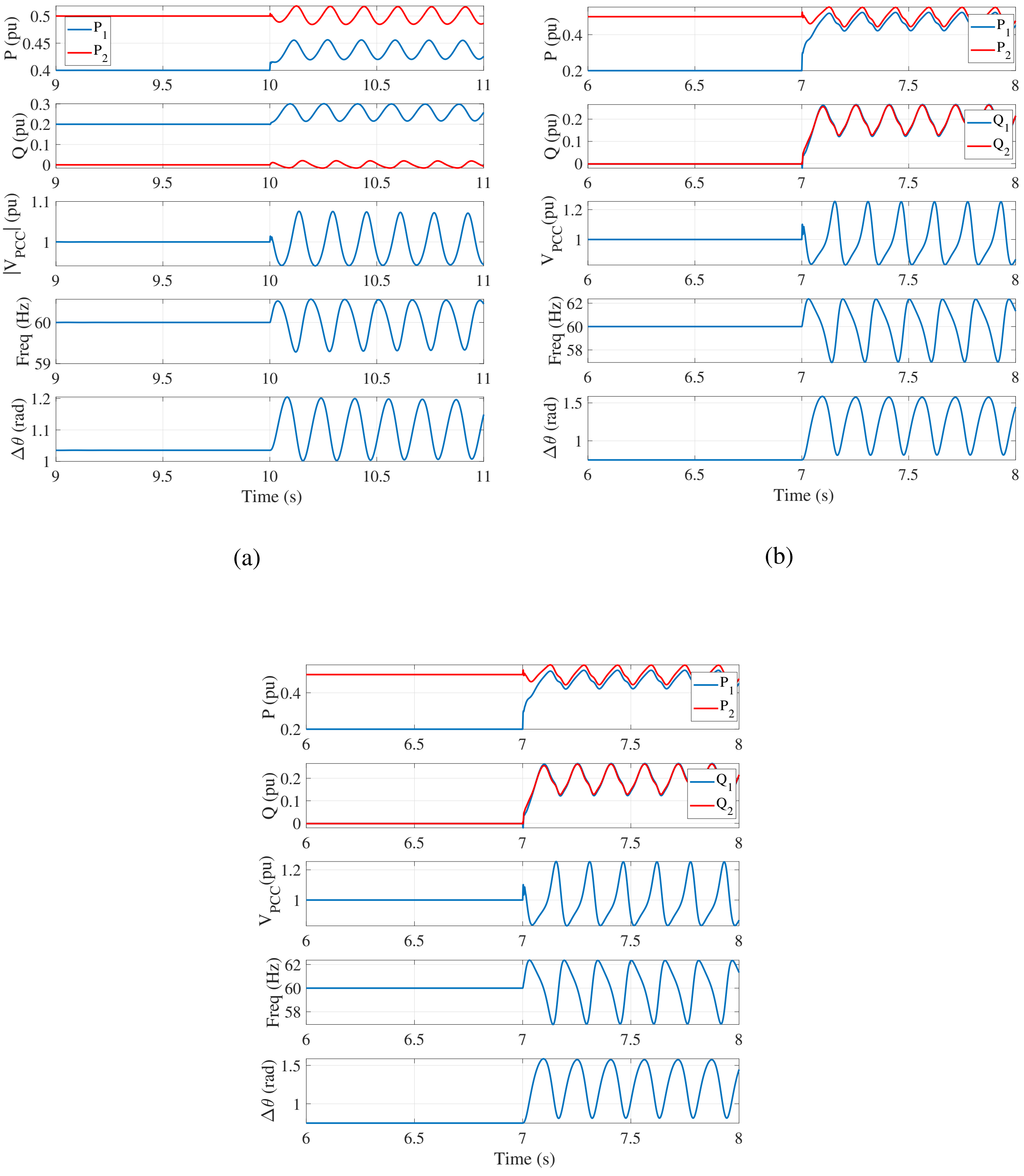

(a)

(b)

(c)

Figure 3.3 Time domain response of $P$, $Q$, $V_{\mathrm{PCC}}$, $f_{\mathrm{PLL}}$ and $\Delta\theta$. The figure presents the system's response under weak grid conditions, when subject to real power order increase. (a) Testbed 0: 6.0 Hz weak grid oscillations. (b) Testbed 1: 6.5 Hz weak grid oscillations. (c) Testbed 2: 3.2 Hz oscillations.

## 3.4 Weak Grid Instability: The Critical Reason

In this section, the critical reason for weak grid oscillations is explained using a two-IBR system presented in Figure 3.4, with each IBR represented as a controllable current source.

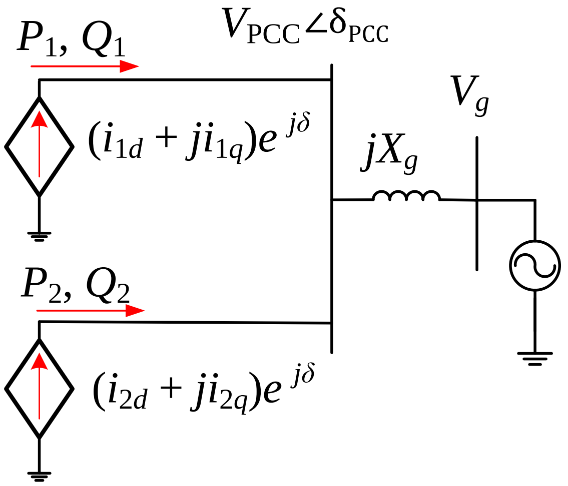

Figure 3.4 Simple representation of a two-IBR system.

The transmission line's resistance and electromagnetic dynamics are neglected. Hence, $jX_g$ is used to represent the transmission line. The two IBRs adopt vector control [2], [46] in the $dq$ frame, where the $d$ axis of the frame is aligned with PCC bus voltage's space vector. This simplified model is adapted from the senior authors' prior work [14]. In [14], the author has developed three linearized models of grid-connected IBR. The conclusion is that the PCC bus voltage phasor is related not only to the $dq$ axis currents but also to the PLL angle ($\delta$). Hence, for a two-IBR system, from the circuit analysis, the following relationship is obtained:

$$V_{\text{PCC}}e^{j\delta_{\text{PCC}}} = jX_g(i_{1d}+ji_{1q}+i_{2d}+ji_{2q})e^{j\delta} + V_g \tag{3.3}$$

Here, $\delta_{\text{PCC}}$ is the PCC bus angle, $\delta$ is the angle from the PLL. Linearizing RHS and LHS (5.6) we get:

$$\begin{aligned} \text{LHS} &= e^{j\delta_{\text{PCC}}}\Delta V_{\text{PCC}} + jV_{\text{PCC}}e^{j\delta_{\text{PCC}}}\Delta\delta_{\text{PCC}} \\ \text{RHS} &= X_g e^{j\delta}[j(\Delta i_{1d}+\Delta i_{2d}) - \Delta i_{1q} - \Delta i_{2q} - \Delta\delta(i_{1d}+i_{2d}+ji_{1q}+ji_{2q})] \end{aligned} \tag{3.4}$$

Assuming $\delta_{\text{PCC}} \approx \delta$, and comparing real and imaginary parts of RHS and LHS, we get:

$$\begin{aligned} \Delta V_{\text{PCC}} &= -X_g(i_{1d}+i_{2d})\Delta\delta - X_g(\Delta i_{1q}+\Delta i_{2q}) \\ \Delta\delta_{\text{PCC}} &= \frac{X_g}{V_{\text{PCC}}}(\Delta i_{1d}+\Delta i_{2d}) - X_g(i_{1q}+i_{2q})\Delta\delta \end{aligned} \tag{3.5}$$

In (3.5), assuming $i_{1q} = i_{2q} = 0$, and $G_{\text{PLL}}(s)$ is the transfer function from $\Delta\delta_{\text{PCC}}$ to $\Delta\delta$, and rearranging (3.5) we arrive at:

$$\Delta V_{\text{PCC}} = -\underbrace{X_g(i_{1d}+i_{2d})\frac{X_g}{V_{\text{PCC}}}}_{c} G_{\text{PLL}}(s)(\Delta i_{1d}+\Delta i_{2d}) - X_g(\Delta i_{1q}+\Delta i_{2q}) \tag{3.6}$$

From equation (3.6), we can conclude that for a two IBR system, $\Delta V_{\text{PCC}}$ has contributions from $\Delta i_{1d}$, $\Delta i_{2d}$, $\Delta i_{1q}$, and $\Delta i_{2q}$, including the PLL dynamics. In this work, PLL is designed to have a bandwidth of 13 Hz, as per the parameters of the PI gains as 60 and 1400. The bode diagram is presented in Figure 3.5.

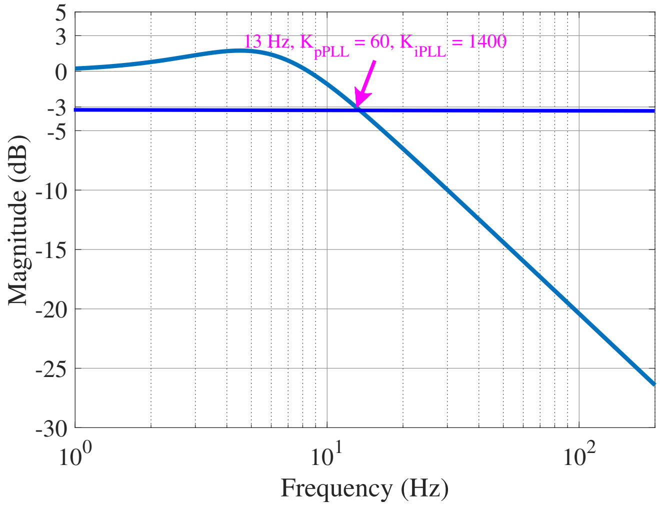

Figure 3.5 Bode diagram of 13 Hz PLL.

For our study, the concerned frequency range is from $0 \approx 10$ Hz. Hence, we can safely assume in this frequency range, PLL does not interfere with the dynamics of the system, i.e., $G_{\mathrm{PLL}}(s) = 1$. A linear relationship is also found for the real power and the reactive power for both IBRs. Similarly, expressions for $\Delta P_2$ and $\Delta Q_2$ are obtained. With the help of (3.6) and (3.7), a linear block system of the two-IBR system is constructed as shown in Figure 3.6.

$$\begin{aligned} \Delta P_1 &= i_{1d0}\Delta V_{\mathrm{PCC}} + V_{\mathrm{PCC}}\Delta i_{1d} \\ \Delta Q_1 &= -i_{1q0}\Delta V_{\mathrm{PCC}} - V_{\mathrm{PCC}}\Delta i_{1q} \end{aligned} \tag{3.7}$$

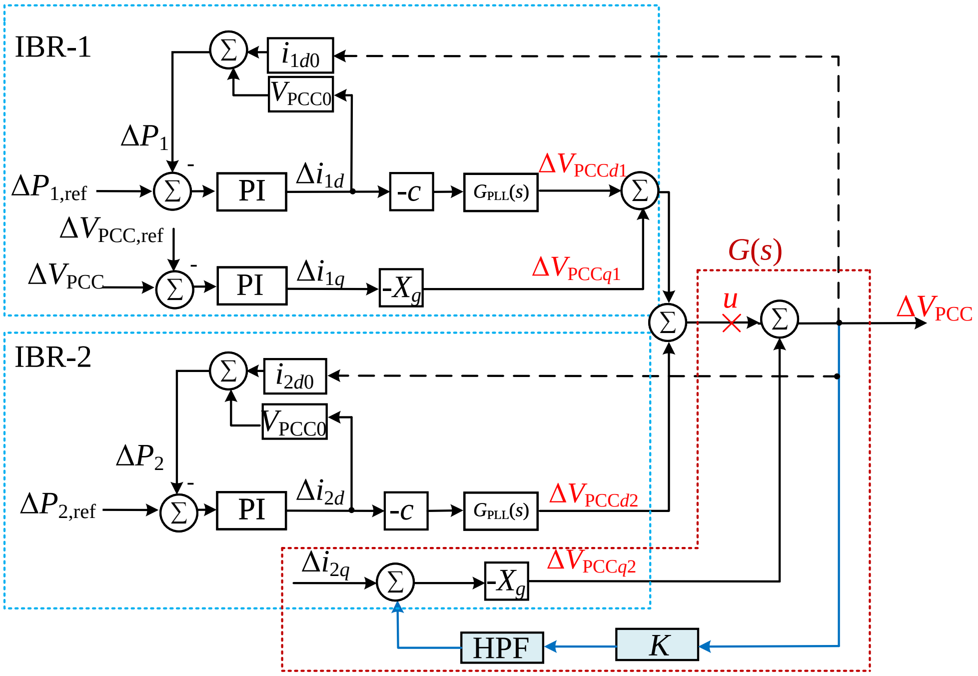

Figure 3.6 Block diagram with the stability enhancement strategy for a two-IBR system.

The block diagram clearly shows the coupling between the real power control and the PCC voltage. At weak grid conditions, $X_g$ is large. For high power transfer, $\delta$ is also large. Thus, a weak grid and high power transfer may lead to a large value of $c$. According to (3.6) and the block diagram, an increase in the power order will result in the increase in $\Delta i_d$ and in turn the reduction of $\Delta V_{\mathrm{PCC}}$.

This may cause $\Delta P$ to reduce. Hence, if the effect of $\Delta i_d$ is overwhelming, $\Delta P$ may not follow the power order, introducing an instability mechanism. More details on the instability mechanism can be found in [47] and [48]. Furthermore, this analysis is in coherence with the NERC reliability guidelines regarding the classical small signal voltage instability of an IBR system operating under weak grid conditions [49].

## 3.5 Importance of Coordinated Control

As mentioned earlier, from the preliminary research, we found that with one IBR in voltage control mode and another in reactive power control mode, the entire system can achieve better stability. To back up the claim, we performed EMT simulations. Testbed 0 has one IBR in $PV_{\text{PCC}}$ control mode and IBR 2 in $PQ$ control mode, while Testbed 1 has both IBR working under $PV_{\text{PCC}}$ control mode. The control structure is presented in Figure 3.2. The results are presented in Figure 3.7. Under similar weak grid conditions (SCR $\approx$ =1), Testbed 0 shows better stability, while Testbed 1 goes to an unstable condition. Hence, with reactive power support, the system in the multi-IBR network performs better. The concept involves modulating one or more IBRs to inject reactive power, thereby boosting system performance and optimally pushing IBRs toward steady-state limits. The underlying principle of coordination draws inspiration from practical insights, as elaborated below.

### 3.5.1 Philosophy of Coordination

The key philosophy of coordination of IBR is developed after examining AEMO's success in identifying the source of 7-Hz oscillations in West Murray [50, 51]. Five solar farms were pinpointed as the negative influencers. The critical technology in identifying the five troublemakers is essentially observing the phase shift between voltage ($V$) and reactive power ($Q$) output from each IBR under 7-Hz perturbation. If $V$ and $Q$ are in phase, this IBR contributes to the oscillation mode. On the other hand, if $V$ and $Q$ are out of phase, this IBR is mitigating the oscillation (other IBRs cause the oscillation).

From the physics point of view, in the low-frequency range (ignoring very fast transmission line electromagnetic dynamics), it is well known that injecting reactive power into a grid can cause an increase in voltage. The mathematical relationship is as follows.

$$\Delta V \approx X_g \Delta Q \tag{3.8}$$

where $X_g$ is the grid reactance. Note that the above simplified relationship has ignored the effect of real power and/or real current $i_d$'s effect on voltage. A relationship between $\Delta V$ and $dq$ current has been presented in (7).

This relationship is based on the well-known relationship between the reactive power injection and voltage. Reference [52] has used the same insight to explaining the wind turbine var oscillations. Also in [53], a similar expression has been used to explain oscillations in parallel a solar PV and a battery energy storage system.

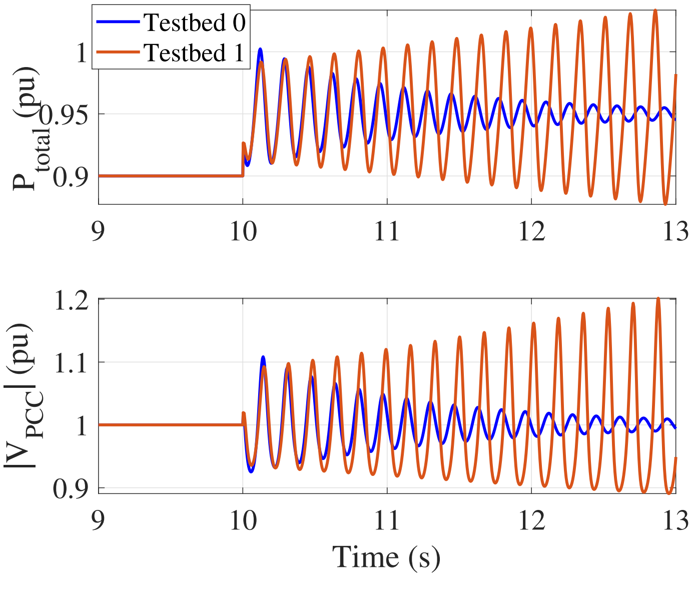

Figure 3.7 Time domain results for total real power $P_{\text{total}}$ at the PCC bus from IBR 1 and IBR 2 and the PCC bus voltage. Testbed 0 and testbed 1 are under very weak grid conditions ($X_g$ =1 pu). The $Q$ controller PI gains for IBR-2 in Testbed 0 are (2,25), whereas, in Testbed 1, $V_{\text{PCC}}$ controller PI gains for IBR-2 is (0.2,25).

If there are two IBRs connected to the point of interconnection, the voltage will have contributions from the reactive power injection from both IBRs. The equation can be modified as:

$$\Delta V \approx \underbrace{X_g \Delta Q_1}_{\Delta V_1} + \underbrace{X_g \Delta Q_2}_{\Delta V_2} \tag{3.9}$$

It is possible that $\Delta V_1$ and $\Delta V$ are in phase while $\Delta V_2$ and $\Delta V$ are out of phase, which implies that IBR1 contributes to oscillations and is the negative influencer while IBR 2 mitigates oscillations and is the positive influencer. Therefore, we have one more means to push the limit besides carefully designing/improving individual IBR controls. We can coordinate IBR controls to make further improvements.

Our philosophy is to have one or more IBRs provide damping through counter reactive power. To achieve this goal, an IBR has to be designed to have its $q$-axis current order modulated by the positive feedback of voltage deviation. For the two-IBR system, IBR2's $q$-axis current order will be modulated.

$$\Delta i_{q2} \approx \Delta i^*_{q2} = k\Delta V, \Longrightarrow \Delta Q_2 \approx -V\Delta i_{q2} \propto -\Delta V \tag{3.10}$$

Based on (3.10), $\Delta Q_2 = -V\Delta i_{q2} - i_{2q0}\Delta V$. Assuming that the initial $q$-axis current is 0 or IBR2 is not providing nor absorbing significant reactive power, $\Delta Q_2 \approx -V\Delta i_{q2}$. Hence, when the $q$-axis current order is modulated to be proportional to $\Delta V$, the resulting reactive power modulation $\Delta Q_2$ counters $\Delta V$ and can mitigate voltage oscillations.

### 3.5.2 Control Implementation

The control strategy includes modulating one group of IBR's $q$-axis current order according to the voltage deviation. This is achieved by the feedback of PCC voltage signal $V_{\text{PCC}}$ after passing through a high-pass filter (HPF) with a transfer function $\frac{\tau s}{\tau s+1}$. Here, $1/\tau$ is the cutoff frequency of the HPF filter. An additional gain $K$ is added to provide flexibility. The control is implemented in the multi-IBR system linear block diagram as shown in Figure 3.6.

The transfer function from $u$ to $\Delta V_{\text{PCC}}$ is given by:

$$G(s) = \frac{1}{1 + X_g \text{HPF}} = \frac{1}{1 + X_g\, K\, \frac{\tau s}{1+\tau s}} = \frac{1 + \tau s}{1 + s\tau(X_g K + 1)} \tag{3.11}$$

From (3.11), we can conclude the transfer function imitates a low-pass filter (LPF). The Bode diagrams of the transfer function for $X_g = 1.0$, $\tau = 0.1$ s and for different parameters of $K$ are presented in Figure 3.8. From Figure 3.8, it is observed that the cutoff frequency for $K = 1$, is around 1.1 Hz.

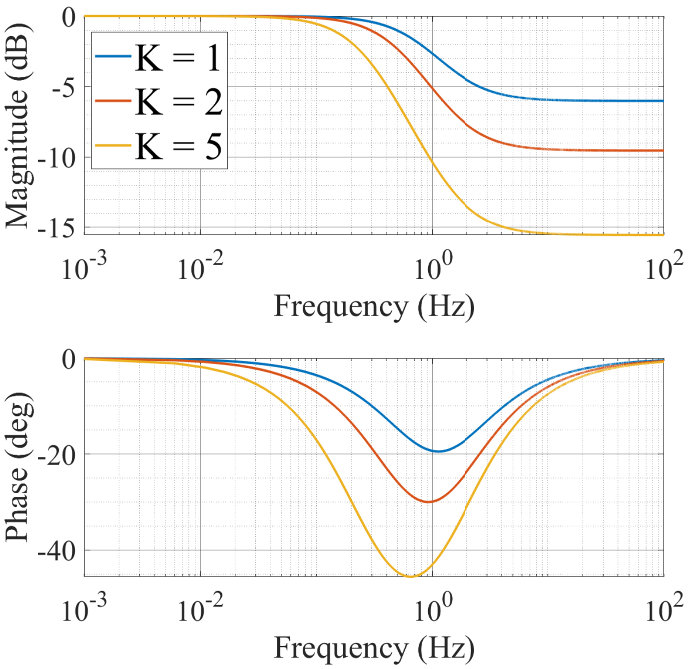

Figure 3.8 Bode diagram of the transfer function $G(s)$ which imitates the behavior of a LPF.

Conclision is that the gain of the transfer function $G(s)$ is unity without the HPF controller. With the feedback controller, the gain of the transfer function is reduced in the region of several

Hz. Hence, the coupling between the $dq$-axis current and the $\Delta V_{\text{PCC}}$ is also decreased. Thus, the HPF controller is beneficial for weak grid voltage stability.

### 3.5.3 Linear Model-Based Analysis

The block diagram presented in Figure 3.6 is built in MATLAB/Simulink. The following operating condition is assumed: $P_{1,\text{ref}} = P_{2,\text{ref}} = 0.5$ p.u. , and $V_{\text{PCC}}$ is maintained at 1 p.u. A small step change of 1% is applied in $\Delta P_{1,\text{ref}}$. The simulation results in Figure 3.9 show that the system undergoes poorly damped oscillations of about 7 Hz. When the HPF control is enabled, the oscillations are damped out. The selected parameters for the stability controller are $\tau = 0.1$ s and $K = 5$.

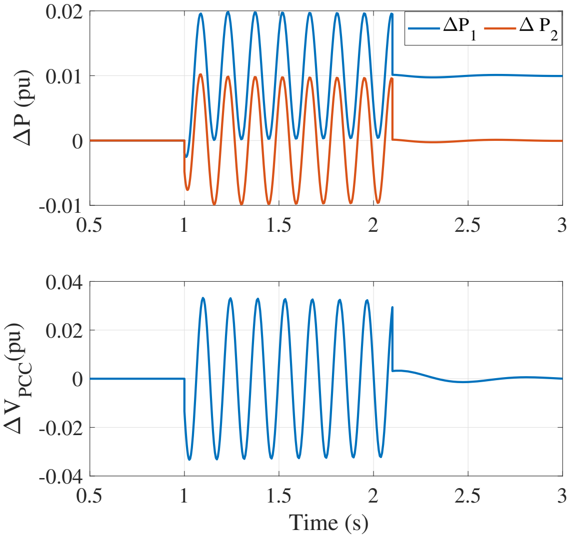

Figure 3.9 Time domain results to demonstrate the effects of stability controller in mitigation of weak grid oscillations. When the controller is disabled 7 Hz oscillations are observed when a step change is introduced $\Delta P_{1,\text{ref}}$ of 0.01 pu at $t = 1$ s. The HPF controller is enabled at $t = 2.1$ s and the oscillations are mitigated.

Further investigation is conducted in the frequency domain by analyzing the open-loop transfer function. The open-loop system is obtained by breaking at the point marked a red cross in Figure 3.6. The transfer function obtained is from $u$ to $u$. The Bode diagram is presented in Figure 3.10. It is observed that without the HPF controller, the phase shifting occurs at 7 Hz and the gain margin at this point is 0 dB, which implies a marginally stable system. After the addition of the HPF controller (red curve), the system is stable at the 7 Hz frequency point with a positive gain margin. This observation is in coherence with the time-domain results presented in Figure 3.9. It can be seen that the HPF controller makes $G(s)$ (from $u$ to $\Delta V_{\text{PCC}}$) act as a LPF and effectively reduce the open-loop gain in the several Hz region. In turn, it enhances stability.

## 3.6 EMT Simulations with HPF Controller

The HPF-based voltage feedback is introduced in IBR2 for both testbeds to modulate its $q$-axis current order, as shown in Figure 3.11. Two tests are conducted for each testbed.

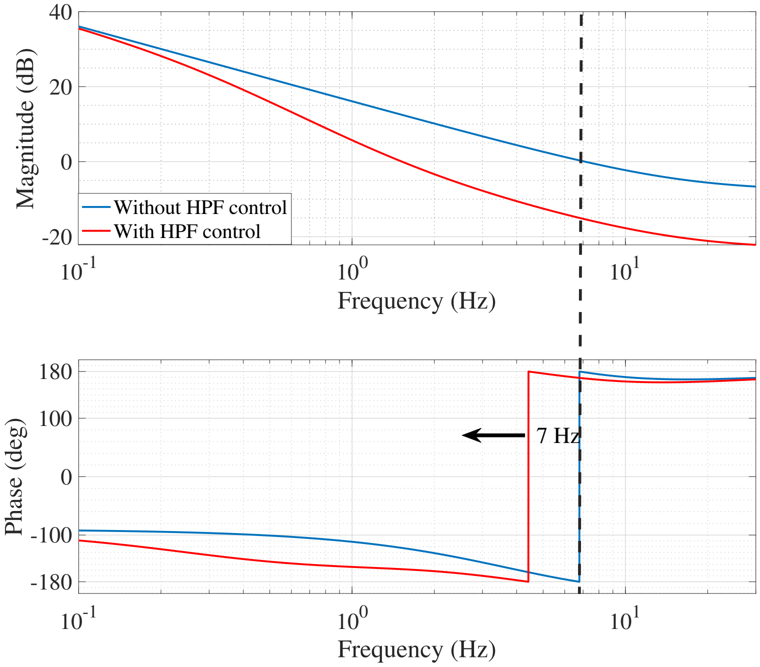

Figure 3.10 Bode diagram of open-loop system from $u$ to $u$. Blue curve presents the open-loop transfer function without the HPF controller and at 7 Hz system is marginally stable. The red curve presents the transfer function with the HPF controller which indicates a stable system at 7 Hz.

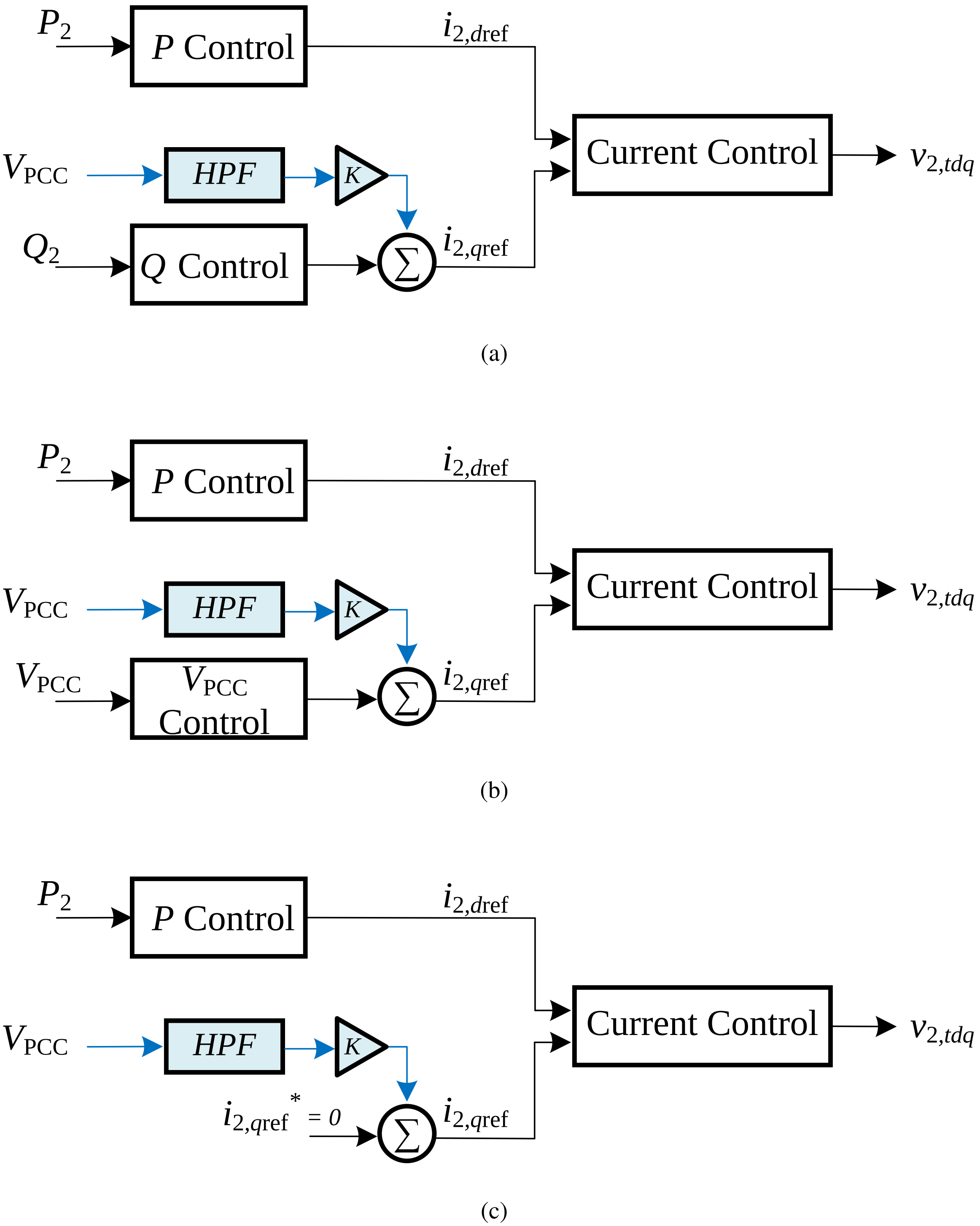

(a)

(b)

(c)

Figure 3.11 IBR-2 with the voltage feedback control. (a) Testbed 0 (b) Testbed 1 (c) Testbed 2.

### 3.6.1 Small Disturbance Test: Power Order Increase

For the first test, the power order of the two IBRs is increased in steps. For Testbed 1, when the power orders of IBR-1 and IBR-2 are 0.474 p.u. and 0.5 p.u. (i.e., total power output is 0.974 p.u.) respectively, the system experiences low-frequency oscillations. The frequency of the oscillations is 6.5 Hz. A similar power order increase is implemented in Testbed 2. When $P_{1,\text{ref}} = 0.55$ p.u. and $P_{2,\text{ref}} = 0.3$ p.u., the system undergoes 3.2-Hz oscillations.

#### *3.6.1.1 Selection of HPF Parameters*

The HPF feedback control is implemented in IBR-2. The parameters for the feedback control are the HPF's time constant $\tau$ and the gain $K$. The selected values for Testbed 0, Testbed 1, and Testbed 2 are listed in Table. 5.1. For Testbed 1, the oscillation frequency is 6.5 Hz, hence the time constant at 0.1 s and the gain at 5 can provide a sufficient gain reduction in the frequency region. On the other hand, Testbed 2 has an oscillation frequency of 3.2 Hz. Though the same control can provide gain reduction at 3.2 Hz, it also introduces a phase lag of more than 20°. To have a smaller phase lag, the time constant 0.2 s and the gain 1 are used for Testbed 2.

Table 3.3 Feedback control parameters selected for testbed 1 and testbed 2.

| | $\tau$ | $K$ | power transfer increase |
|---|---|---|---|
| Testbed 1 | 0.1 | 5 | 9% |
| Testbed 2 | 0.2 | 1 | 14% |

Enabling the feedback control in IBR-2 mitigates the 6.5-Hz oscillations in Testbed 1, and 3.2-Hz oscillations in Testbed 2. The dynamic responses of the real power $P$, reactive power $Q$, PCC bus voltage $V_{\text{PCC}}$, and the output from the PLL (frequency, and the angle $\Delta\theta$) for IBRs are presented in Figure 3.12. It can be clearly seen that the HPF control mitigates the weak grid oscillations in all the cases.

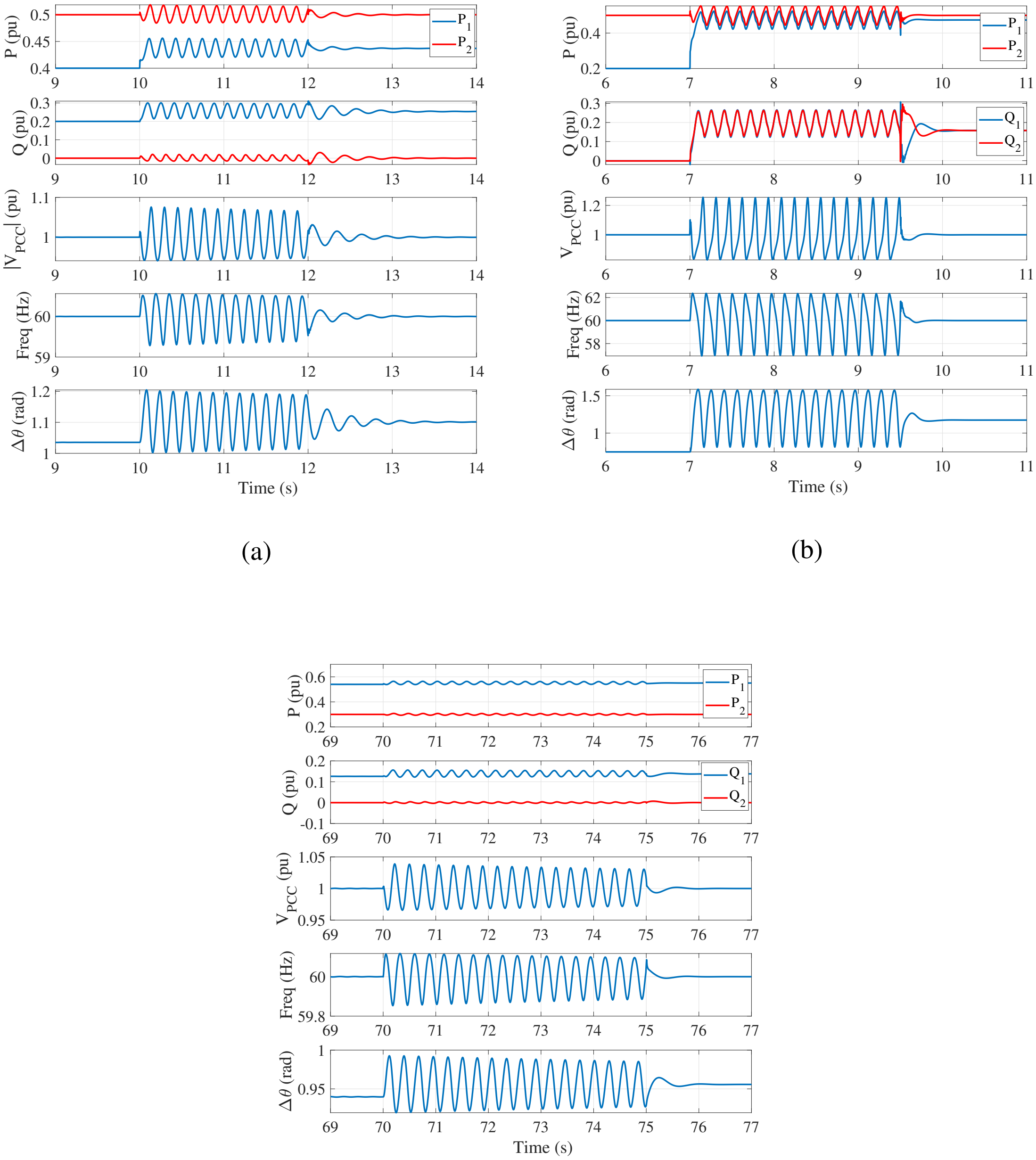

(a)

(b)

(c)

Figure 3.12 Time domain response of $P$, $Q$, $V_{\mathrm{PCC}}$, $f_{\mathrm{PLL}}$ and $\Delta\theta$. The figure presents the system's response with and without the introduction of HPF stability controller when subject to real power order increase. (a) Testbed 0: The HPF voltage control is enabled at $t = 12$ s. The controller mitigates the 6.0 Hz weak grid oscillations. (b) Testbed 1: The HPF voltage control is enabled at $t = 9.5$ s. The controller mitigates the 6.5 Hz weak grid oscillations. (c) Testbed 2: The HPF voltage control is enabled at $t = 75$ s. The controller mitigates 3.2 Hz oscillations.

For Testbed 1, with the added controller, the power exporting capability of the two IBRs increases from 0.974 p.u. to 1.064 pu, a 9% increase. While for Testbed 2, the power transfer capability increases from 0.85 p.u. to 0.97 p.u. i.e., 14% increase. For Testbed 1, the power transfer is close to the steady-state limit (1.1 p.u.) associated with $X_g$ = 1 p.u. The simulation results for the three testbeds working at the marginal stable conditions are presented in Figure 3.13.
The remarks that can be made include:

1. The HPF controller is able to mitigate weak grid oscillations (6.5 Hz and 3.2 Hz) for different scenarios. This capability shows the robustness of the control.
2. The HPF control helps increase the stability margin of multi-IBR systems.
3. The HPF control does not change steady-state operating conditions.

### 3.6.2 Large Disturbance Test: Line Tripping

Furthermore, large disturbance tests are conducted to emulate a transmission line tripping event. For both testbeds, $X_g$ changes from 0.5 (SCR $\approx$ 2) to $X_g$ = 1.0 (SCR $\approx$ 1). Without the feedback control strategy, the system loses its synchronism and becomes unstable. With feedback control, the system remains stable and sustains the large disturbance. The results for the line tripping event are presented in Figure 3.14. For Testbed 1, at $t$ = 2$s$, $X_g$ changes from 0.5 p.u. to 1.0 p.u. The total power output from both IBRs is 0.95 pu ($P_1$ = 0.45 pu, and $P_2$ = 0.5 pu). While for Testbed 2, the line trip event happens at $t = 5$ s, and the total power output is 0.77 pu ($P_1$ = 0.45 p.u., and $P_2$ = 0.32 p.u.).

### 3.6.3 Grid Forming Converter

Further investigation is done on the effectiveness of a stability enhancement strategy for a single grid-forming inverter operating under weak grid conditions [21, 22]. The system topology and control structure used in the study is depicted in Figure 3.15, with the control structure being

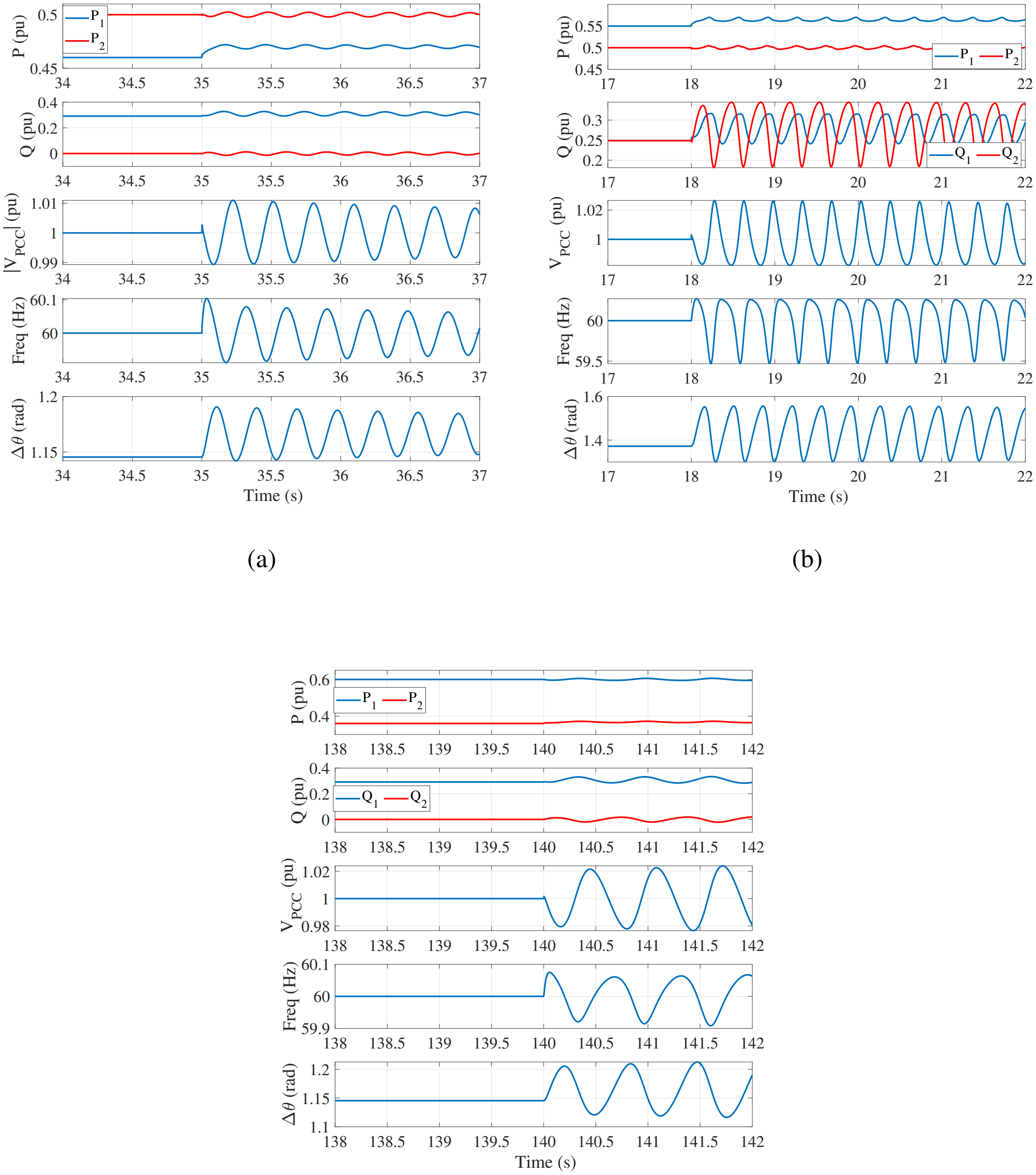

(a)

(b)

(c)

Figure 3.13 Time-domain responses of real power $P$, reactive power $Q$, $V_{\mathrm{PCC}}$, frequency and PLL angle $\Delta\theta$. The results indicate that the power transfer capability increased after the stability controller's introduction. (a) Testbed 1 is able to push 1.06 p.u. power where, as (b) Testbed 2 can push around 0.97 p.u. power.

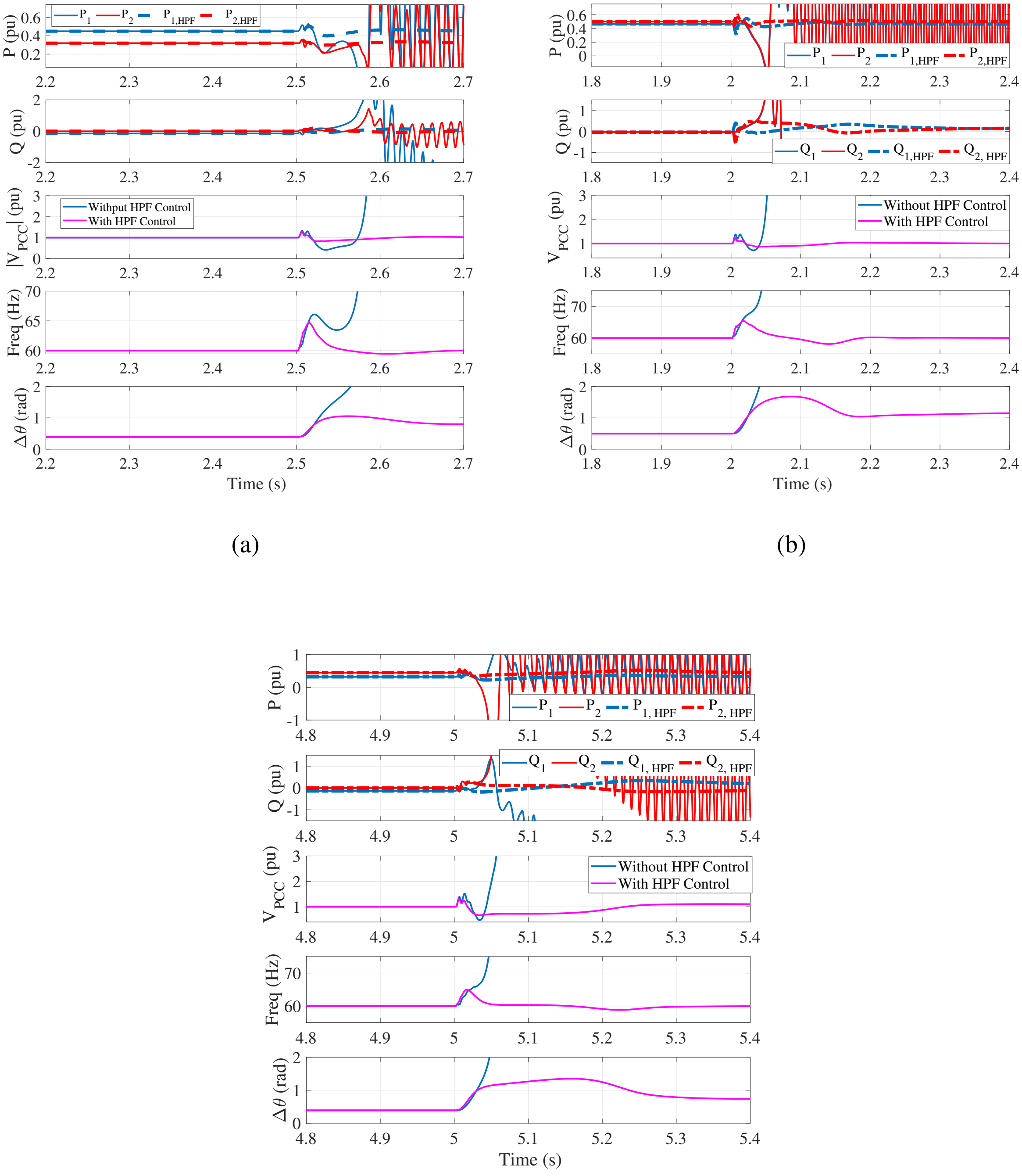

(a)

(b)

(c)

Figure 3.14 Line tripping event. $P$, $Q$, $V_{\text{PCC}}$, $f_{\text{PLL}}$ and $\Delta\theta$ when $X_g$ changes from 0.5 p.u. to 1 p.u. (a) Testbed0 (b) Testbed 1 (c) Testbed 2.

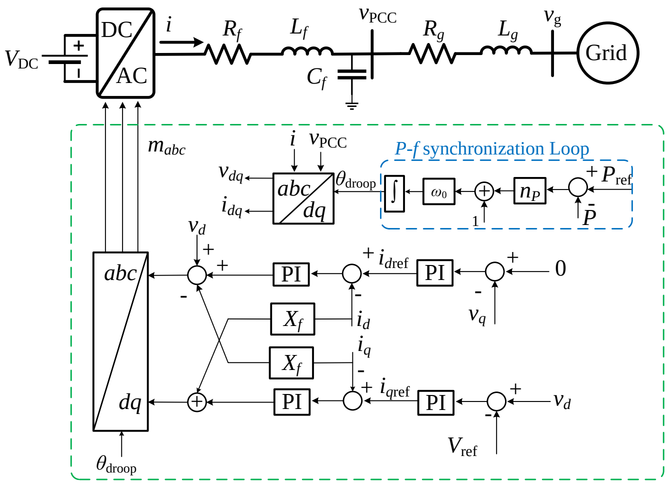

Figure 3.15 System topology of grid-connected grid forming converter.

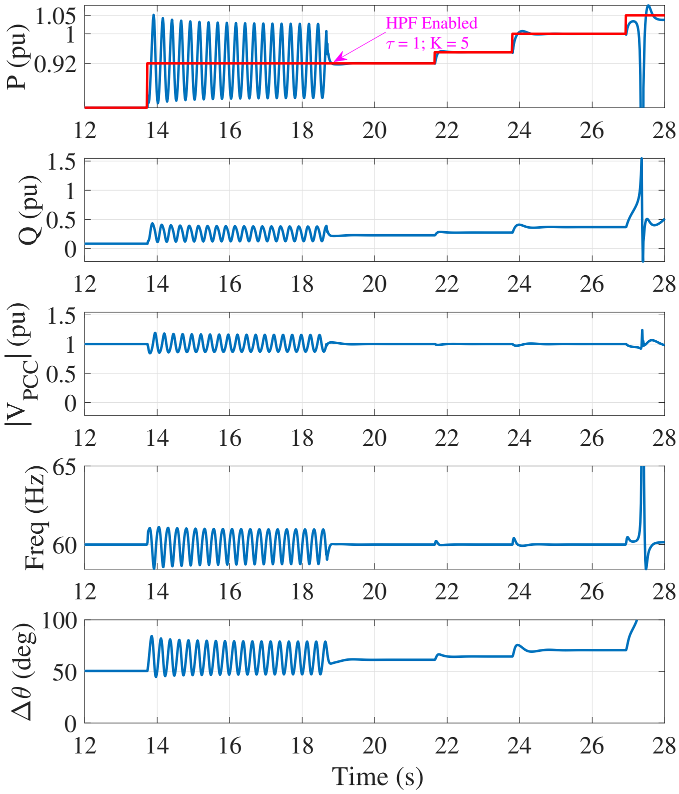

Figure 3.16 Time-domain responses of real power $P$, reactive power $Q$, $V_{PCC}$, frequency and PLL angle $\Delta\theta$. The results indicate that the power transfer capability increased after the stability controller's introduction.

adapted from the works of [23, 54]. Detailed parameters are provided in Table. 3.2. Under weak grid conditions, when the reference power output, $P_{\text{ref}}$, was set to 0.92, the system exhibited poorly damped oscillations with a frequency of approximately 4 Hz. We enabled the HPF controller, which effectively mitigated the oscillations. Consequently, the system could now sustain a power output of around 1.04 per unit (pu) before encountering instability. The results are presented in Figure 3.16.

## 3.7 Hardware Validation

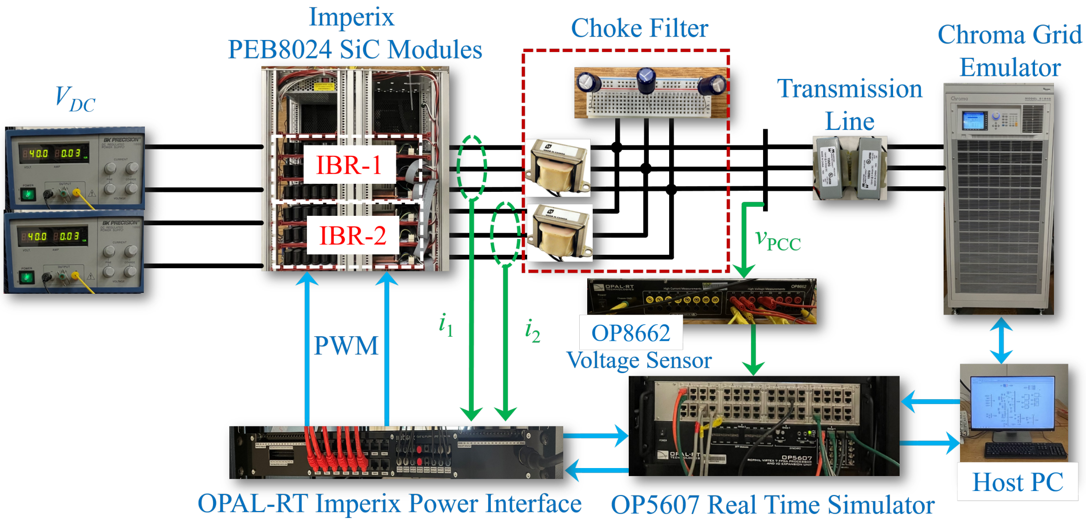

Figure 3.17 Laboratory scale hardware testbed for experimental validation.

To further substantiate the proposed stability feedback control scheme, a laboratory-scale hardware testbed is established. The hardware testbed includes two three-phase converters consisting of 6 Imperix PEB8024 half-bridge power modules, Chroma Regenerative Grid Simulator 61845 acting as power grid source, Opal RT's OP5607 real-time simulator for control algorithm implementation, analog voltage and current sensors, DC power supply and other passive elements. The detailed structure of the hardware testbed is presented in Figure 3.17. The control algorithm is implemented using MATLAB-based RT-Lab on the host PC. Similarly, the Chroma Grid emulator is also controlled remotely using LabVIEW. Both the inverters are in real power and PCC voltage

Table 3.4 Parameters used for experimental validation.

| Description | Parameter | Value |
|---|---|---|
| Power Base | $S_b$ | 50 VA |
| Voltage Base | $V_b$ | 20 V |
| Nominal Frequency | $f_0$ | 60 Hz |
| Grid Voltage | $V_g$ | 20 V |
| DC Voltage | $V_{DC}$ | 40 V |
| Choke Filter | $X_f$ | 0.0707 pu |
|  | $R_f$ | 0.0034 pu |
|  | $B_c$ | 0.1417 pu |
| Transmission Line Inductance | $X_g$ | 0.457 pu |
| Transmission Line Resistor | $R_g$ | 0.0950 pu |
| Inner Loop Control | $k_{ip}$, $k_{ii}$ | 1, 10 |
| Outer Loop Control,$P$ control | $k_{Pp}$, $k_{Pi}$ | 0.25, 25 |
| Outer Loop Control,$V_{\text{PCC}}$ | $k_{Vp}$, $k_{Vi}$ | 0.25, 25 |
| Feed-forward filter | $T_{vf}$ | 0.002 |
| PLL | $k_{\text{PLL}p}$, $k_{\text{PLL}i}$ | 60, 1400 |
| Switching Frequency | $f_{SW}$ | 5 kHz |

regulation mode. The system strength as observed by the two IBRs at the PCC bus is 2.18 ($X_g$ = 0.457 p.u.). The steady-state power limit corresponding to $X_g$ = 0.457 p.u. and $R_g$ = 0.0950 p.u. is 2.578 p.u. The testbed parameters are tabulated in Table 3.4.

The power order is increased in small steps for IBR-1, while the power order for IBR-2 is kept at $P_{2,\text{ref}}$ = 0.5 p.u. Initially, the stability control is disabled. When the power output from IBR-1 is 1.62 p.u the system undergoes poorly damped 4-Hz oscillations. After the occurrence of the oscillations, the HPF stability control is enabled at $t = 141.5$ s, which mitigates the oscillations. The results are shown in Figure 3.18(a). The parameters selected for the HPF stability control are $K = 2$, and $\tau = 0.1$ s.

Furthermore, with the stability control enabled, the system is marginally stable when IBR-1 power output level is 1.83 p.u. while the IBR-2 is still exporting 0.5 p.u., as shown in Figure 3.18(b). The experimental validation demonstrates the efficacy of the proposed stability controller. With the stability control, the total power output increased from 2.05 p.u. to 2.3 p.u., $\approx$ a 12% increase. The steady-state limit is 2.578 p.u.

## 3.8 Conclusions

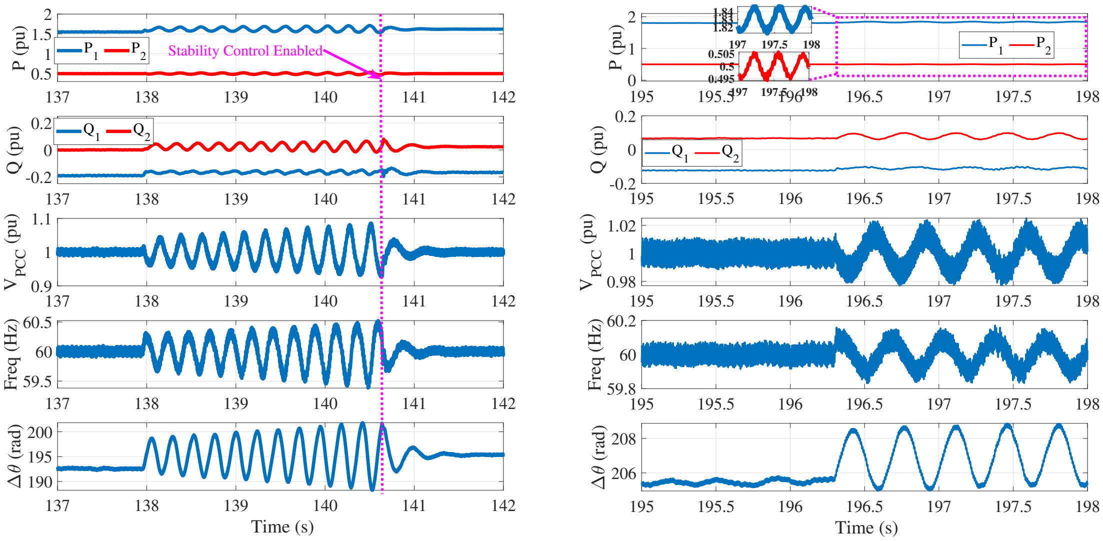

(a) (b)

Figure 3.18 Hardware experiment results. (a) Time domain responses when the power order is increased. The results show the performance of the stability controller in mitigating the 4 Hz oscillations. (b) The results show the stability controller's performance in terms of increased power transfer capability of the system. The steady-state power transfer limit for the hardware testbed is 2.58 p.u.

By employing a suitable coordination scheme, a multi-IBR system has increased stability margin while operating in very weak grid conditions. With one group of IBR's $q$-axis current orders modulated by a voltage feedback, the effect is similar as reducing the coupling between the VSC's real power control and the PCC voltage. This effect helps enhance weak grid voltage stability. The coordination can be implemented by feedbacking of the PCC bus voltage after passing it through a high-pass filter. Linear analysis, EMT-based computer simulation, and hardware experiments all confirm the efficacy of the stability enhancement strategy. In addition, the strategy is simple and straightforward for implementation and is robust against the host system. Therefore, it leads to high practical values.

This research focuses on grid-following (GFL)-based IBRs. While grid-forming (GFM) technology is promising, GFL converters will continue to have a large market share in the future grid. In essence, GFM aims for better voltage and frequency support. Given that GFL technology is mature and has been deployed in power grids for many years, active research has also been carried out to improve GFL's performance and achieve GFM type performance, e.g., [55, 56]. In addition, the proposed coordination strategy is based on a physical law of grid characteristics, regardless GFL or GFM. Therefore, this strategy is generic and can be certainly applied for GFM-based IBRs.

# Chapter 4: Performance of IBRs in Series Compensated Networks

In this chapter IBRs modeling is done when the system is connected to a series compensated network. Stability analysis is done for both GFL and GFM IBR technologies.

## 4.1 Introduction

Series compensation in power grids expands the system's power flow limit and transient stability. While this approach proves economically beneficial, introducing series capacitors brings forth challenges, notably subsynchronous resonances (SSR). A pivotal case study in 1973 at the Mohave Generating stations highlighted the connection between the LC resonance mode of transmission lines, the induction generator effect (IGE) of synchronous generators, and rotor shaft oscillation modes, resulting in sustained oscillations and shaft failures [57].

There has been a paradigm shift in the evolving landscape of power grids, integrating IBRs such as type-3 wind turbines, type-4 wind turbines, and solar photovoltaic (PV) systems. However, the increased penetration of IBR sources has introduced unwanted dynamics, including weak grid oscillations and series capacitor related oscillations. The task force paper by the IEEE Power & Energy Society IBR subsynchronous oscillation (SSO) task force [58] provides a survey of 19 real-world SSO events associated with IBRs due to either weak grid interconnection or radial interconnection with series capacitors. A recently published article [59] reviews operational challenges in the IBR interfaced grid and also recommends the examination of series compensation conditions.

Over the years, the root cause of SSO in type-3 wind farms radially connected to series compensated networks has been extensively investigated in literature [18, 19, 60–63]. For instance, [18, 19] have shown that IGE, instead of torsional interactions is the main contributor to SSO due to the negative equivalent rotor resistance of the doubly-fed induction generator in the subsynchronous frequency region, and converter current control exacerbates the effect. More recently, [63] shows that phase-locked-loop (PLL) dynamics can worsen SSO stability.

While the interactions of series capacitor and a type-3 wind farm have been thoroughly investigated in the literature, there exists a few literature investigating potential interactions of series capacitor with grid-connected converters popularly adopted in type-4 wind farms, solar PV farms, and battery energy storage systems.

### 4.1.1 Related Literature

Back in 2012, with type-3 wind farms being vulnerable to interactions with series capacitors, a paper from Siemens [64] suggests that type-4 wind farms are immune to series capacitor SSOs based on electromagnetic transient (EMT) simulation results. In the testbed presented in [64], the interconnected grid is assumed to be very strong. In 2019, potential risks of series capacitor to type-4 wind farm were reported in [65]. Authors of [65] adopted frequency-domain admittance-based approach to investigate stability issues in a type-4 wind farm radially connected to a series compensated network. Non-passivity of the type-4 wind farm's admittance in the subsynchronous frequency range is found to contribute to oscillatory instability.

Reference [65] has pointed out instability and attributed instability to inverter admittance being non-passive. On the other hand, non-passivity alone cannot be used to explain why a series compensated network introduces instability, while a non-compensated network does not. Additionally, characteristics of such oscillations have not been analyzed. For example, in type-3 wind farms, an increased compensation level leads to higher oscillation frequency in the phase current and voltage. How does compensation level influence oscillations in type-4 wind farms?

This question has been answered in [66], which provides more granular-level analysis results. The authors particularly pointed out that PLLs may interact with series compensation and cause oscillations. Additionally, the oscillation frequency is associated with the PLL bandwidth, instead of series compensation level. In another word, the series compensation related LC mode can push the PLL mode to instability. In short, [66] has clearly pointed out the potential interactions of series compensation with the synchronizing unit in a GFL-IBR.

With a paradigm shift in the current power grid, more and more grid-forming IBRs are being integrated. Grid-forming controls (GFM) are recommended by grid reliability authority to provide frequency and voltage support [67]. This control is very different from the conventional grid-following control (GFL). While the GFL control has a PLL acting as the synchronizing unit, the GFM control has a power-based synchronization scheme. Will series compensation interacts with GFM-IBRs?

### 4.1.2 Goals and Contributions

This work aims to fill the gaps and address how series compensation may interact with IBRs by providing thorough analysis and validations. In the work, the behavior of GFL-IBRs and GFM-IBRs when they are radially connected to a series compensated network is analyzed. The analysis is done in two steps. First, the stability issue with the help of EMT simulations is identified. Second, nonlinear state-space models are developed to perform in-depth analysis. Tools like eigenvalues and participation factors are used to understand the root cause of the stability issues. Although the primary focus is identifying stability issues in GFM-based IBRs, we also revisit GFL-IBRs and provide more detailed explanations. The analysis shows that similar to GFL-IBRs, GFM-IBRs are also prone to oscillatory behavior due to series compensation.

## 4.2 System Topology

The topology is presented in Figure 4.1. The system consists of a three-phase DC-AC inverter connected to the power grid via a parallel combination of transmission lines represented by $R_g$, $L_g$, and $C_g$, where $C_g$ is the series compensation. A choke filter is connected between the terminals of the inverter. The choke filter is represented by $R_f$, $L_f$ and $C_f$. A constant DC voltage source supplies the inverters, and the AC grid is modeled as a constant voltage source (infinite bus). Furthermore, $i_c$ is the converter current, $v_{\text{PCC}}$ is the PCC bus voltage, and $i_g$ is the grid current. In this work, two testbeds are considered. Testbed-1 has an IBR system operating in the GFL mode with a PLL as the synchronizing unit, and testbed-2 has an IBR operating in the GFM mode with a power-based synchronization unit.

### 4.2.1 Control Structure

#### *4.2.1.1 GFL*

Testbed-1 has the IBR operating in GFL mode. The inner loop is the current control loop in *dq* frame, and the outer loop is real power $P$ and PCC bus voltage magnitude $|V_{\text{PCC}}|$ control. The real power control generates $i_{d\text{ref}}$ for the $d$-axis current control loop and $|V_{\text{PCC}}|$ generates $i_{q\text{ref}}$ for the $q$-axis current control loop. A PLL is used to measure the PCC bus angle $\theta_{PCC}$ and PLL's output angle $\theta$ is used for synchronization. The *dq* converter voltage references generated by the inner control is converted to the *abc* reference using the PLL's angle $\theta$. Furthermore, the real power $P$ and the reactive power $Q$ are given by:

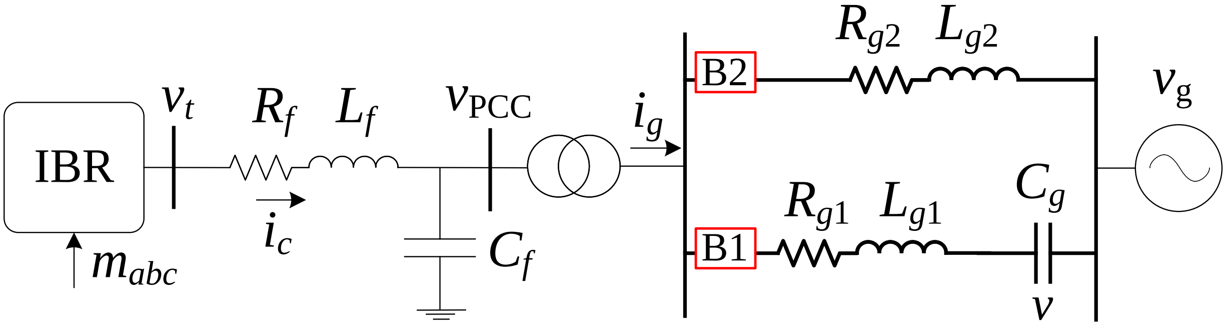

Figure 4.1 System topology for a grid-connected IBR power plant.

$$\begin{aligned} P &= v_{\text{PCC}d}\, i_{cd} + v_{\text{PCC}q}\, i_{cq} \\ Q &= v_{\text{PCC}q}\, i_{cd} - v_{\text{PCC}d}\, i_{cq} \end{aligned} \tag{4.1}$$

Here, $v_{\text{PCC}d}$ and $v_{\text{PCC}q}$ are the $dq$ components of $v_{\text{PCC}}$. The magnitude of the PCC bus voltage is obtained as:

$$|V_{\text{PCC}}| = \sqrt{v_{\text{PCC}d}^2 + v_{\text{PCC}q}^2} \tag{4.2}$$

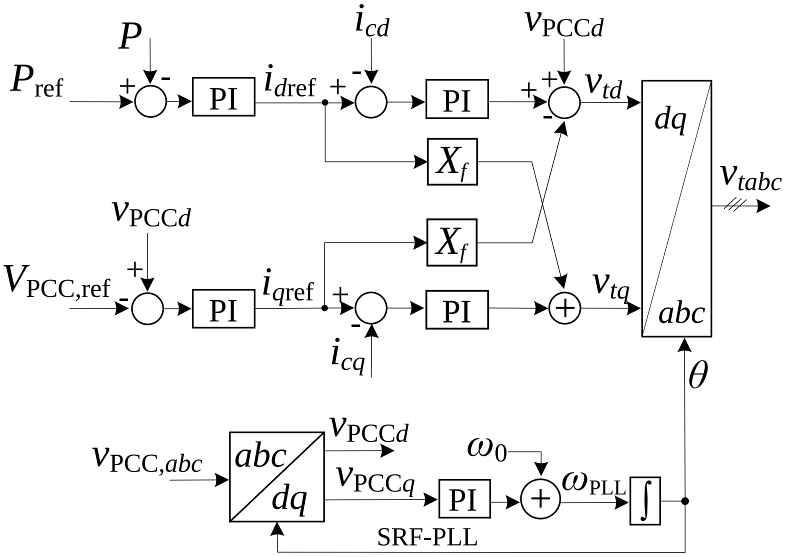

Figure 4.2 Control structure for GFL IBR.

The control structure for the GFL IBRs is presented in Figure 4.2.

#### *4.2.1.2 GFM*

In Testbed-2, the IBR is operating in GFM mode. The control structure is adapted from the works of [23,26]. The inner loop and the $q$-axis outer control are similar as those in testbed-1. The synchronizing angle is generated by the $P-f$ droop and the objective of the $d$-axis outer control is to have the PCC bus voltage space vector aligned with and the synchronizing frame. The control enforces the PCC voltage's $q$-axis projection on the synchronizing frame $v_q$ to be 0. This $v_q$ control generates $i_{d\text{ref}}$ for the $d$-axis inner current control. The $P-f$ droop regulates the PCC bus's real power and provides the synchronizing angle $\theta$. Here, $R$ is the droop gain defining the per unit

Table 4.1 Circuit parameters used for testbed-1 and testbed-2.

| Description | Parameter | Value | Bandwidth |
|---|---|---|---|
| Power Base | $S_b$ | 100 MVA | |
| Voltage Base | $V_b$ | 575 V | |
| Nominal Frequency | $\omega_0$ | $2\pi 60$ rad/s | |
| Grid Voltage | $V_g$ | 1 pu | |
| Choke Filter | $X_f$ | 0.15 pu | |
| | $R_f$ | 0.003 pu | |
| | $B_c$ | 0.25 pu | |
| Line Inductance | $X_{g1}, X_{g2}$ | vary | |
| Line Resistor | $R_{g1}, R_{g2}$ | $0.1X_{g1}$, $0.1X_{g2}$ | |
| Control Parameters for GFL IBR | | | |
| Inner current | $k_{ip}$, $k_{ii}$ | 0.3, 5 | 114 Hz |
| $P$ control | $k_{Pp}$, $k_{Pi}$ | 0.4, 40 | 5 Hz |
| $V_{\text{PCC}}$ | $k_{Vp}$, $k_{Vi}$ | 0.4, 40 | SCR dependent |
| PLL | $k_{p\text{PLL}}$, $k_{i\text{PLL}}$ | 150, 10000 | 33 Hz |
| | | Resonance point | 15 Hz |
| Control Parameters for GFM IBR | | | |
| Inner current | $k_{ip}$, $k_{ii}$ | 0.3, 5 | 114 Hz |
| $v_d$ control | $k_{Pp}$, $k_{Pi}$ | 0.5, 20 | SCR dependent |
| $v_q$ control | $k_{Vp}$, $k_{Vi}$ | 0.5, 20 | SCR dependent |
| $P$-$f$ droop | $R$ | 0.05 | |

change in frequency for one per unit change in power. The control structure for the GFM IBRs is presented in Figure 4.3.

Table 4.1 presents the parameters used for testbed-1 and testbed-2. Note that for testbed-1, the GFL has a PLL with a relatively large integral gain. This leads to a bandwidth of 33 Hz for the PLL"s angle-tracking closed-loop system. The resonance frequency of this closed-loop system is 15 Hz. The particular set of parameters is chosen to create oscillations at 15 Hz when the GFL-IBR is radially connected to an RLC circuit, as shown in Figure 4.4.

### 4.2.2 EMT Simulation Results

EMT simulations are conducted using MATLAB/Simscape Electrical Specialized Power Systems. The two testbeds are subjected to a line-tripping event at $t = 30$ s. Two types of line-tripping events are examined. In case 1 (breaker B2 opens), the RL circuit is tripped leaving the IBR radially connected to the RLC circuit. In case 2 (breaker B1 open1), the RLC circuit is tripped leaving the IBR radially connected to the RL circuit. Furthermore, the RL circuit and the RLC circuit have the same effective grid reactance. The operating conditions are as follows: $P_{\text{ref}} = 0.5$ pu, and $V_{\text{PCC,ref}} = 1$ pu. The line parameters for the testbeds are shown in Table 4.2.

Table 4.2 Line parameters for the testbeds in two cases.

| | RLC circuit | RL circuit |
|---|---|---|
| testbed-1 | $X_{g1} = 1$ pu, $X_{Cg} = 0.62$ pu | $X_{g2} = 0.38$ pu |
| testbed-2 | $X_{g1} = 1$ pu, $X_{Cg} = 0.365$ pu | $X_{g2} = 0.635$ pu |

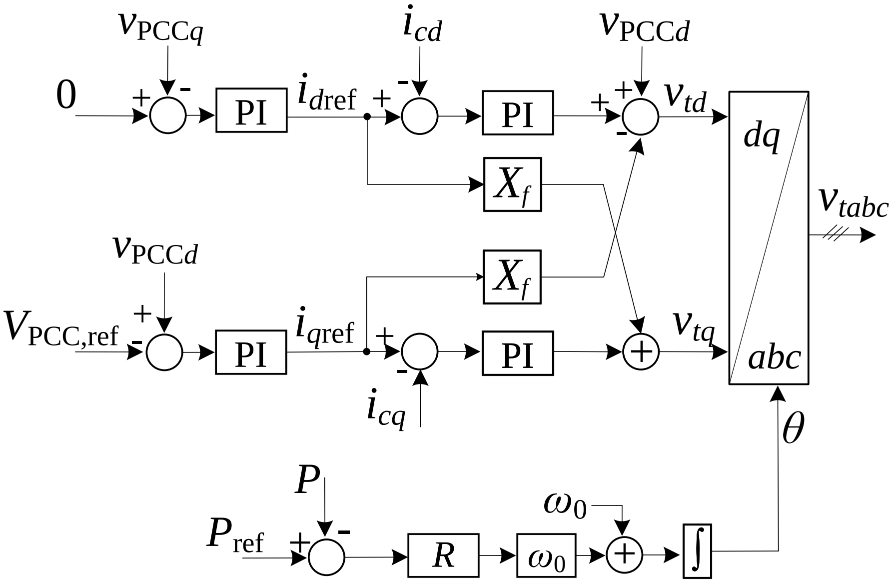

Figure 4.3 Control structure for GFM IBR.

The time-domain simulation results are shown in Figure 4.4 for the two specified cases. For testbed-1 with a GFL-IBR, the initial grid reactance is 0.19 pu. When the line is tripped at $t = 30$ s, for case 1 (RLC), the system is connected to a series compensated network ($K = 62\%$) and the total grid reactance of 0.38 pu. Similarly, for case 2, the grid reactance changes from 0.19 pu to 0.38 pu. On observing results presented in Figure 4.4a, we can see that for similar operating conditions, when the GFL-IBR is connected to the RLC network, undamped 15 Hz oscillations appear. When the GFL-IBR is connected to RL network, the system is stable. Hence, it can be said that the series compensation introduces unwanted stability issues.

Similarly, the same can be said on observing results presented in Figure 4.4b for testbed-2 of the GFM-IBR. For case 1, when the system is connected to the series compensated network (RLC, $K = 36.5\%$), the system undergoes an undamped oscillation of around 6 Hz. However, when connected to the RL network, a line tripping event (total grid impedance changes from 0.317 pu to 0.635 pu), the system is stable and the 6-Hz oscillations can be quickly damped out. Hence, the EMT simulation results demonstrate the interactions of a series compensated line with an IBR in either GFL or GFM modes.

## 4.3 Analytical Modeling and Analysis Results

In this section, we examine the influencing factors of the observed 15-Hz and 6-Hz oscillations in the two testbeds. While EMT simulation results show that series capacitor is the main influencer, we are not able to obtain further insights regarding how inverter control blocks contribute to the oscillations. The EMT simulation results of testbed-1 show that reactive power measurements have more obvious oscillations compared to the real power measurements, implicating $q$-axis control and PLL may play a role. On the other hand, to have a clear view of the influencing factors, eigenvalue-based analysis is necessary. To have linear time invariant (LTI) model through Jacobian linearization, we will build a nonlinear analytical model representing the IBR radially connected to an RLC circuit. The model has all its state variables constant at steady state to ensure Jacobian linearization.

### 4.3.1 Analytical Model

The analytical model is developed in the $dq$ domain. The system presented in Figure 4.1 is modeled with four main blocks: a synchronization unit (PLL or $P$-$f$ droop), inner and outer control, circuit dynamics, and frame conversion, as shown in Figure 4.5. It is noted that, while the signals at the circuit level are based on the grid frame (superscript **g**, rotating at the nominal frequency of $\omega_0$), the signals associated with the control structure are based on the frame or angle provided by the synchronization unit.

The state variables for both testbeds are described as follows: the grid-frame variables associated with circuit dynamics, including the converter current $i^g_{cdq}$, the PCC bus voltage $v^g_{\mathrm{PCC}dq}$, the grid current $i^g_{gdq}$, and the series capacitor voltage $v^g_{dq}$ (circuit dynamics), synchronizing-frame states representing the outer loop PI controllers $x_1$ ($d$-axis) and $x_2$ ($q$-axis) and inner current controls $x_3$ and $x_4$. In the GFL-IBR, the PLL incorporates two state variables: $\Delta\omega$ (associated with PI controller) and $\Delta\theta$. Conversely, in the GFM-IBR, the synchronization unit has one state variable $\Delta\theta$. Consequently, the GFL-IBR testbed comprises 14 state variables, while the GFM IBR system consists of 13 state variables.

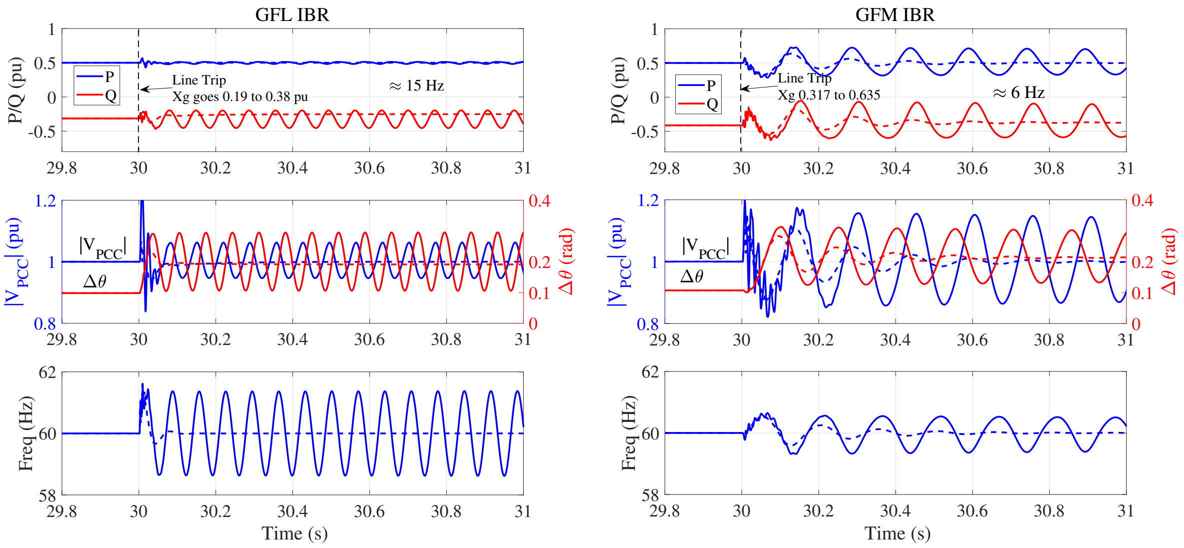

(a)

(b)

Figure 4.4 Time-domain responses for the real power $P$, $Q$, $|V_{\mathrm{PCC}}|$, $\Delta\theta$,and frequency (Hz). Solid lines: with series compensation. Dashed lines: without series compensation. The line tripping occurs at $t = 30$ s. (a) GFL (b) GFM.

#### 4.3.1.1 Circuit Dynamics

The analytical model of the circuit dynamics is developed in the grid $dq$ frame that rotates at a speed of $\omega_0$. The differential equations for the RLC circuit dynamics are presented as follows:

Here $R_f$, $X_f$, and $B_f$ are the per unit values of the $RLC$ components of the choke filter and $L_f = X_f/\omega_0$, $C_f = B_f/\omega_0$. Similarly $R_{g1}$, $X_{g1}$ , and $B_g$ are the per-unit values of the transmission line parameters and $L_{g1} = X_{g1}/\omega_0$, $C_g = B_g/\omega_0$. This block has $v^g_{td}$ and $v^g_{tq}$ (the $dq$ components of the converter terminal voltage $v_t$) and the grid voltage $v^g_{gd}$, $v^g_{gq}$ as input and outputs the converter current, PCC bus voltage, real and reactive power.

$$\begin{cases} \frac{di^g_{gd}}{dt} &= -\frac{R_{g1}}{L_{g1}} i^g_{gd} + \frac{1}{L_{g1}} v^g_d - \frac{1}{L_{g1}} v^g_{gd} + \omega_0 i^g_{gq} \\ \frac{di^g_{gq}}{dt} &= -\frac{R_{g1}}{L_{g1}} i^g_{gq} + \frac{1}{L_{g1}} v^g_q - \frac{1}{L_{g1}} v^g_{gq} - \omega_0 i^g_{gd} \\ \frac{di^g_{cd}}{dt} &= -\frac{R_f}{L_f} i^g_{cd} + \frac{1}{L_f} v^g_{td} - \frac{1}{L_f} v^g_d + \omega_0 i^g_{cq} \\ \frac{di^g_{cq}}{dt} &= -\frac{R_f}{L_f} i^g_{cq} + \frac{1}{L_f} v^g_{tq} - \frac{1}{L_f} v^g_q - \omega_0 i^g_{cd} \\ \frac{dv^g_{\mathrm{PCC}d}}{dt} &= \frac{1}{C_f}(i^g_{cd} - i^g_{gd}) + \omega_0 v^g_{\mathrm{PCC}q} \\ \frac{dv^g_{\mathrm{PCC}q}}{dt} &= \frac{1}{C_f}(i^g_{cq} - i^g_{gq}) - \omega_0 v^g_{\mathrm{PCC}d} \\ \frac{dv^g_d}{dt} &= \frac{1}{C_g}(i^g_{gd}) + \omega_0 v^g_q \\ \frac{dv^g_q}{dt} &= \frac{1}{C_g}(i^g_{gq}) - \omega_0 v^g_d \end{cases} \tag{4.3}$$

Similarly, the modeling block for the RL circuit is also developed.

#### 4.3.1.2 SRF-PLL

The synchronization unit in testbed-1's GFL-IBR is PLL. For this work, a second-order PLL is adopted. The $dq$ frame analytical model of the PLL is adapted from the work presented in [14].

#### 4.3.1.3 Frame Conversion

As previously mentioned, the control system operates in a distinct reference frame (angle $\theta$) provided by the synchronization unit, which is a PLL for testbed-1 and a $P$–$f$ droop for testbed-2. The converter control regulates the $dq$ components of converter current $i_c$ and the voltage at the

PCC bus $v_{\text{PCC}}$ in the control frame. Due to the different reference frames adopted for the circuit model and the control, appropriate frame conversion is essential for accurate modeling.

The relationship between the grid frame and the control frame can be found by relating the space vector of current or voltage with its grid frame-based and control frame-based vectors. For example, the PCC bus voltage's space vector $\vec{v}_{\text{PCC}}$ can be related to the grid-frame variables and the control-frame variables as follows:

$$\begin{aligned} &\vec{v}_{PCC} = (v_{\text{PCC}d} + j\, v_{\text{PCC}q})e^{j\theta} = (v^g_{\text{PCC}d} + j\, v^g_{\text{PCC}q})\, e^{j\omega_0 t} \\ \Longrightarrow &(v_{\text{PCC}d} + j\, v_{\text{PCC}q})e^{\Delta\theta} = v^g_{\text{PCC}d} + j\, v^g_{\text{PCC}q}, \end{aligned} \tag{4.4}$$

where $\Delta\theta = \theta - \omega_0 t$. From (4.4), it can be seen that signals in the grid frame can be transformed to the synchronization frame and vice-versa. The complete analytical model is presented in Figure 4.5.

### 4.3.2 Eigenvalue and Participation Factor Analysis

This subsection presents linear system analysis results based on the developed analytical models. We examine the impact of compensation levels (case study 1) and the effects of grid impedance under non-compensated condition (case study 2) for both testbeds. Table 4.3 documents the four types of scenarios.

Table 4.3 Case studies examined for eigenvalue analysis.

| | case study 1 | case study 2 |
|---|---|---|
| GFL | with the RLC circuit only | with the RL circuit only |
| GFM | with the RLC circuit only | with the RL circuit only |

#### 4.3.2.1 *Case Study 1: Effect of Series Compensation Level*

The eigenvalue loci with varying levels of series compensation ($K$) are presented in Figure 4.6. Here, the compensation level varies with a step size of 1%. The eigenvalue loci analysis reveals two modes affected by changes in the compensation level. Mode 1 is situated around the 60 Hz frequency, while Mode 2 is found at 15 Hz for the GFL-IBR and 6 Hz for the GFM-IBR. Mode 1 consistently remains in the Left-Hand Plane (LHP), indicating stability. In contrast, Mode 2 shifts to the Right-Hand Plane (RHP) as the compensation level increases, signifying instability. For the GFL-IBR, the system loses stability when the level of series compensation is more than 66%, whereas in the case of GFM-IBR, the limit is 40%.

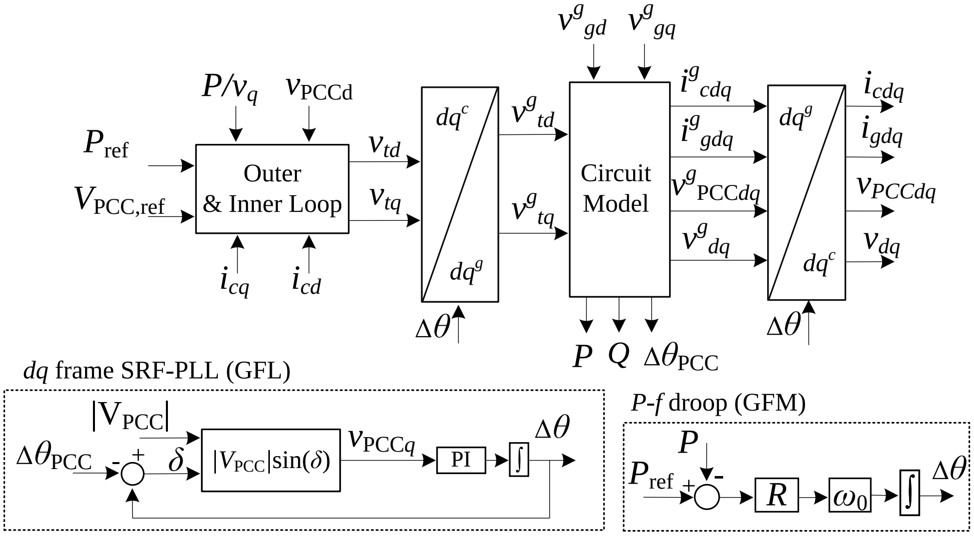

Figure 4.5 The $dq$ frame analytical model for GFL and GFM IBR.

These findings are consistent with the EMT simulation results. When an IBR is directly connected to a series-compensated line, it exhibits undamped oscillations. Specifically, the GFL-IBR oscillates at 15 Hz, while the GFM-IBR oscillates at 6 Hz.

Participation factors (PFs) are numerical measures that indicate the degree to which individual state variables contribute to a specific mode of the system. For Case Study 1, PFs are computed for two modes, Mode 1 and Mode 2, at $K = 66\%$ for the GFL-IBR and $K = 40\%$ for the GFM-IBR. The PFs are listed in Table 4.4, and Table 4.5.

Table 4.4 Participation factors of testbed-1 (GFL-IBR) at $K$ = 66%.

| | State Variables | Mode 1<br>60 Hz | Mode 2<br>15 Hz |
|---|---|---|---|
| Circuit Dynamics | $i^g_{cd}$ | 0.0837 | 0.0049 |
| | $i^g_{cq}$ | 0.0102 | 0.0488 |
| | $i^g_{gd}$ | 0.04 | 0.0018 |
| | $i^g_{gq}$ | 0.1979 | 0.2676 |
| | PCC volt $v^g_{\text{PCC}d}$ | f0.2438 | 0.0062 |
| | PCC volt $v^g_{\text{PCC}q}$ | 0.0199 | 0.0128 |
| | series cap $v^g_d$ | 0.2082 | 0.1967 |
| | series cap $v^g_q$ | 0.4634 | 0.0133 |
| PLL | $\Delta\theta$ | 0.0191 | 0.5512 |
| | $\Delta\omega$ | 0.003 | 0.3217 |
| Outer Loop | $x_1$ | 0.0131 | 0.0072 |
| | $x_2$ | 0.018 | 0.028 |
| Inner Loop | $x_3$ | 0.0041 | 0.0148 |
| | $x_4$ | 0.0007 | 0.0597 |

Table 4.5 Participation factors of testbed-2 (GFM-IBR) at $K$ = 40%.

| | State Variables | Mode 1<br>60 Hz | Mode 2<br>6 Hz |
|---|---|---|---|
| Circuit Dynamics | $i^g_{cd}$ | 0.0257 | 0.025 |
| | $i^g_{cq}$ | 0.0023 | 0.006 |
| | $i^g_{gd}$ | 0.0526 | 0.0117 |
| | $i^g_{gq}$ | 0.0443 | 0.1056 |
| | PCC volt $v^g_{\text{PCC}d}$ | 0.1338 | 0.0101 |
| | PCC volt $v^g_{\text{PCC}q}$ | 0.0033 | 0.0012 |
| | Series cap $v^g_d$ | 0.3002 | 0.044 |
| | Series cap $v^g_q$ | 0.4465 | 0.0026 |
| Droop | $\Delta\theta$ | 0.0037 | 0.4466 |
| Outer Loop | $x_1$ | 0.008 | 0.405 |
| | $x_2$ | 0.008 | 0.171 |
| Inner Loop | $x_3$ | 0.0021 | 0.0109 |
| | $x_4$ | 0.0017 | 0.1378 |

The computed PFs reveal that Mode 1 is closely associated with the series capacitor. Conversely, for Mode 2, the primary contribution stems from state variables linked to the synchronization unit. Specifically, in the GFL-IBR, the PLL plays a significant role, while in the GFM-IBR, the synchronizing units including the $P - f$ droop-based angle generation and the $d$-axis outer control to align the PCC bus voltage to the synchronizing frame, influences Mode 2 dynamics.

#### *4.3.2.2 Case Study 2: Grid Reactance Change*

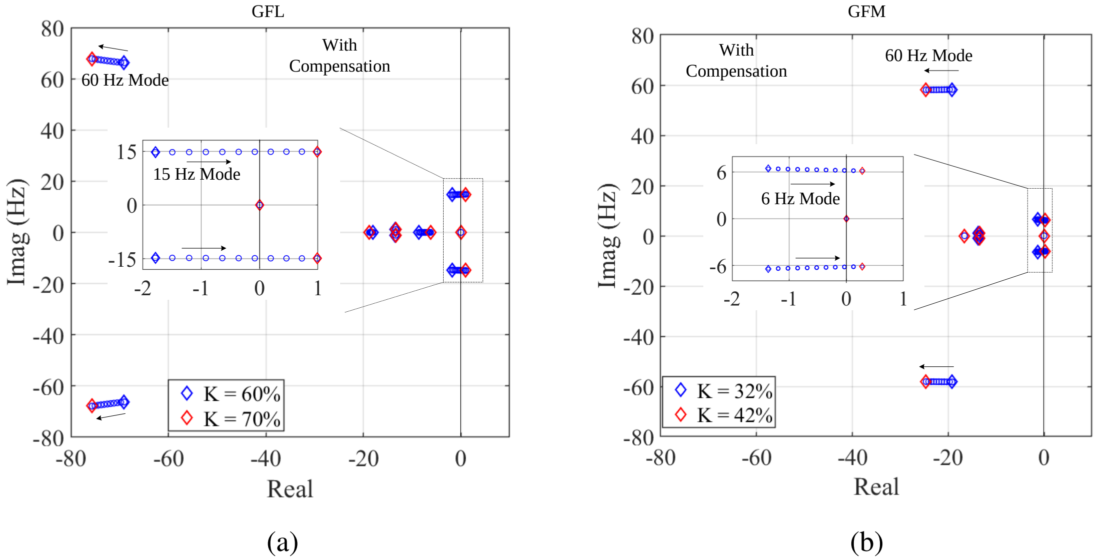

Figure 4.6 The eigenvalue loci with increasing series compensation levels with a step size of 1%. (a) GFL (b) GFM.

In Case Study 2, we analyze an IBR power plant connected to the grid through the RL circuit. The eigenvalue loci, which vary with grid reactance $X_{g2}$, are illustrated in Figure 4.7. One notable distinction in our findings is the absence of Mode 1, previously identified in an RLC circuit, in both testbed-1 and testbed-2 configurations. In testbed-1, the mode at 20 Hz shifts towards right, when the grid strength reduces. The system is stable even for a grid reactance of 1. In testbed 2, the 6-Hz mode resides in the LHP, suggesting a stable system. The eigenvalue loci plots show that without series compensation, the systems are stable.

Additionally, PFs are computed for Mode 2 at $X_{g2} = 1$ pu for the GFL-IBR and GFM-IBR. The PFs are listed in Table 4.6. In the case of GFL-IBR, Mode 2 is associated with the PLL state variable and the $q$-axis grid current. On the other hand, for GFM-IBR, Mode 2 is associated with the droop control and outer loop $v_q$ control.

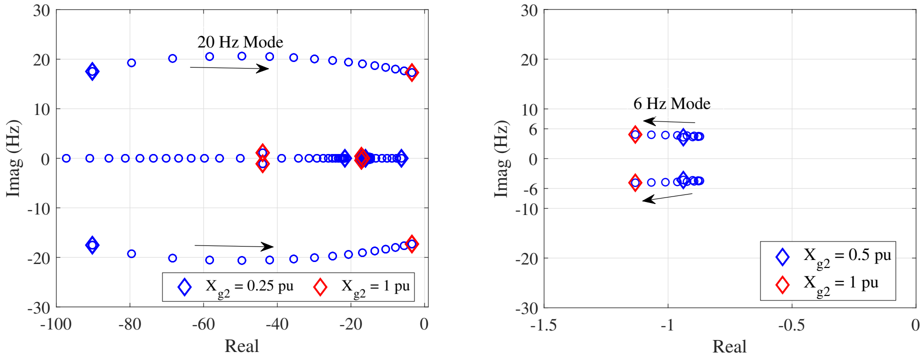

(a) (b)

Figure 4.7 The eigenvalue loci with increasing grid reactance (uncompensated network) with a step size of 5%. (a) GFL. (b) GFM.

Essentially, Mode 2 is associated with the synchronization unit in an IBR. Remarks: Comparison of the eigenvalue loci for the testbeds with and without series compensation shows that the LC mode at 60 Hz introduced by the series capacitor pushes the mode in the lower frequency region associated with the synchronization unit to the RHP, causing instability issues.

The remarks that can be made include:

1. This section's analytical results show that for an IBR (GFL or GFM) grid-integrated system, a radial connection with a series capacitor introduces a 60-Hz mode in the $dq$-frame. This mode does not exist if the IBR is radially connected to an RL circuit. Eigenvalue loci show that when the series compensation level increases, the 60-Hz mode is pushed to the LHP while the mode associated with synchronization is pushed to the RHP.

Table 4.6 Participation factors of mode 2 in GFM and GFL IBRs at $X_{g2} = 1$ pu in case study 2.

|  | State Variables | GFL<br>20 Hz | GFM<br>6 Hz |
|---|---|---|---|
| Circuit Dynamics | $i_{cd}^{g}$ | 0.0386 | 0.0259 |
|  | $i_{cq}^{g}$ | 0.0659 | 0.0037 |
|  | $i_{gd}^{g}$ | 0.039 | 0.0079 |
|  | $i_{gq}^{g}$ | **0.3462** | 0.0699 |
|  | $v_{\mathrm{PCC}d}^{g}$ | 0.0897 | 0.009 |
|  | $v_{\mathrm{PCC}q}^{g}$ | 0.0192 | 0.0011 |
| PLL/ Droop | $\Delta\theta$ | **0.5083** | **0.5133** |
|  | $\Delta\omega$ | 0.2694 | N/A |
| Outer Loop | $x_1$ | 0.0819 | **0.4245** |
|  | $x_2$ | 0.1072 | 0.1259 |
| Inner Loop | $x_3$ | 0.0029 | 0.0118 |
|  | $x_4$ | 0.0636 | 0.1123 |

2. It can be seen that compared to a type-3 wind farm system, where series compensation introduces super- and a sub-synchronous modes (both associated with the LC resonance) [18, 68], IBR systems such as solar PVs, type-4 wind farms, and battery energy storage systems do not have those kinds of modes introduced by series compensation. The reason speculated is that a type-3 wind farm may be viewed as a voltage source for the RLC circuit while the rest IBRs are more suitable to be viewed as current sources. The former then introduces super- and sub-synchronous modes in the current when viewed in the $dq$ frame, while the latter introduces a 60-Hz mode in the voltage viewed in the $dq$ frame.

## 4.4 Block Diagrams and Frequency-Domain Analysis

The developed analytical model can provide further insights into the system by analyzing the frequency domain's open-loop transfer functions (gains). Open-loop gain can provide us with a substantial understanding of the system stability. From the previous results presented in the form of eigenvalues and participation factors, we found that when the system is radially connected to a series compensation network (RLC circuit), the system may lead to instability when the synchronization unit interacts with the RLC circuit. Hence, a feedback system with two blocks will be constructed with the synchronization unit (PLL in testbed-1 and $P$–$f$ droop in testbed-2) connected to the rest of the system.

Figure 4.8 presents the block diagram representation of the decoupled open-loop system, which enables us to study the interaction of the synchronization unit with the rest of the system. The stability assessment is done by evaluating the gain margin from the magnitude plot of the frequency response at the frequency when phase shift happens from -180° to 180°.

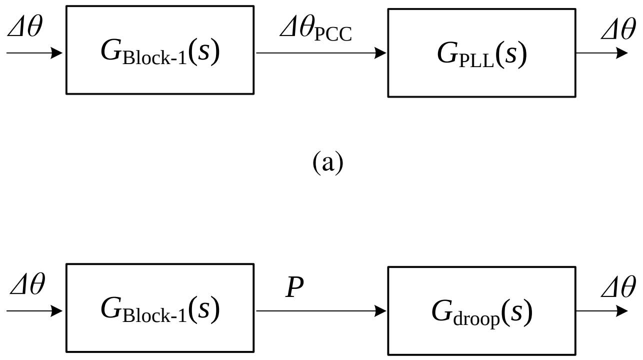

(a)

(b)

Figure 4.8 Block diagram representation for frequency-domain analysis. (a) GFL. (b) GFM.

Here, “Block-1” represents the transfer function from the synchronizing angle $\Delta\theta$ to the PCC bus voltage angle $\Delta\theta_{PCC}$ or the real power measurement $P$. This block can be found in the analytical model by treating the synchronizing angle as a constant and conducting linearization. The total open-loop transfer functions $G_{\text{OL}}(s)$ for testbed-1 and testbed-2 are given by:

$$\begin{aligned} G_{\text{OL}}(s) &= -G_{\text{Block-1}}(s) \times G_{\text{PLL}}(s), \\ G_{\text{OL}}(s) &= -G_{\text{Block-1}}(s) \times G_{\text{droop}}(s). \end{aligned} \tag{4.5}$$

The transfer function of the PLL and droop control is given by:

$$\begin{aligned} G_{\text{PLL}}(s) &= \frac{k_{p\text{PLL}}s + k_{i\text{PLL}}}{s^2 + k_{p\text{PLL}}s + k_{i\text{PLL}}} \\ G_{\text{droop}}(s) &= -\frac{R}{s} \times \omega_0 \end{aligned} \tag{4.6}$$

For GFL-IBR, on observing just the Bode diagram of block-1 in Figure 4.9(a), we can see that for an RLC network, the gain in the range of 1 Hz to 50 Hz is greater than that of the RL network. For the total open-loop gain, including the PLL, the system is marginally unstable for RLC interconnection and stable for RL interconnection, as shown in Figure 4.9(b). Since the phase shifting happens at 15 Hz, it is expected to have 15-Hz oscillation mode. This observation aligns with the eigenvalue analysis results in Figure 4.6a, showing a 15-Hz mode in the RHP when the compensation level increases. When the GFL is radially connected to the RL circuit, the phase shifting happens at 20 Hz, implicating a 20-Hz oscillation mode. This again corroborates the eigenvalue loci shown in Figure 4.7a, where a 20-Hz oscillation mode moving towards right when the grid strength reduces, without losing stability for 50% of power exporting level.

(a)

(b)

Figure 4.9 Frequency-domain responses. (a) GFL Block-1. (b) $G_{\text{OL}}$. The red curve is the response with the RL network, and the blue curve is with the RLC network. The effective grid reactance is 0.34 pu for both the RLC and RC circuits.

For the GFM-IBR testbed, the Bode diagram of block-1 (shown in Figure 4.10a) indicates a more significant gain and phase lag for an RLC network compared to an RL network in the range of 1-10 Hz for the same effective grid reactance of 0.6 pu (corresponds to a compensation level of 40%). For the total loop gain, including the droop control, the phase shift occurs at around 6 Hz. At this frequency, GFM with an RLC network is unstable since the gain is more than 0 dB, while for the RL network, the system exhibits stability, as shown in Figure 4.10b. Observations made using the frequency-domain analysis align with the EMT results shown in Figure 4.4b and the eigenvalue analysis results in Figs 4.6b and 4.7b. Based on the frequency responses of the subsystem relating the PCC bus voltage angle or real power to the synchronizing angle, the following remarks are made.

1. Series compensation increases the sensitivity of the PCC bus voltage angle towards the synchronizing angle, thereby making the GFL-IBR system more prone to instability.

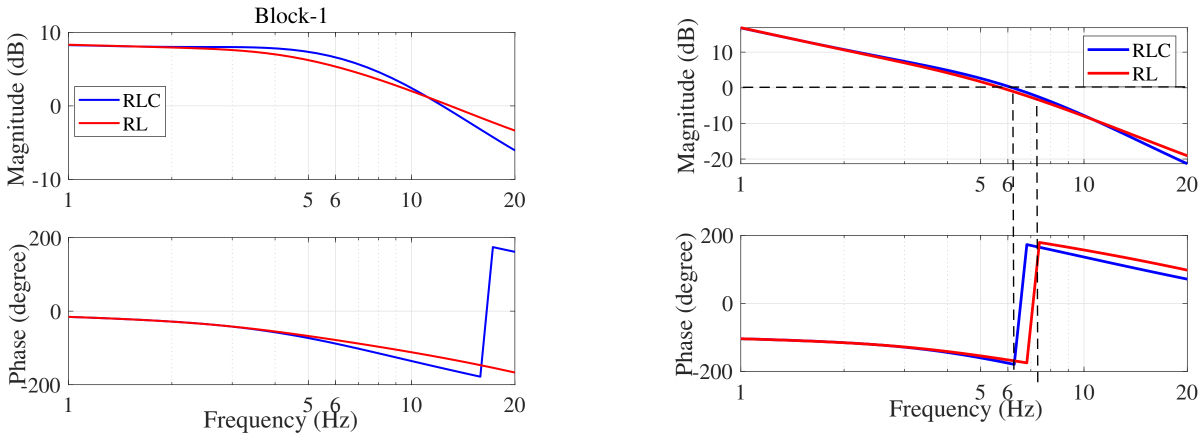

(a) (b)

Figure 4.10 Frequency-domain responses. (a) GFM Block-1. (b) $G_{\mathrm{OL}}$. The red curve is the response with the RL network, and the blue curve is with the RLC network. The effective grid reactance is 0.6 pu.

2. Series compensation introduces more phase lag from the synchronizing angle to the real power measurement, thereby making the GFM-IBR system more prone to instability.

## 4.5 Discussion

### 4.5.1 GFL with $f$-$P$ Droop

The effect of frequency support control is examined for the GFL-IBR when it radially connects to an RLC circuit. Here, additional droop control is added to generate the $P_{\text{ref}}$ for the outer loop, shown in Figure 4.11. The frequency measurement from the PLL is compared with the nominal frequency. Their error is amplified by $1/R$ times to produce the reference power.

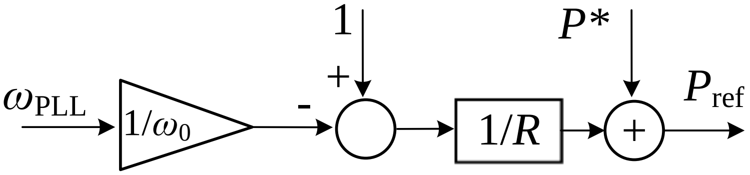

Figure 4.11 Control block diagram of $f-P$ droop adopted for GFL IBR.

The time-domain simulation results showing the comparison of GFL-IBR with and without droop control are shown in Figure 4.14. The RLC circuit has a compensation level of 62%. Observation from the time-domain plots shows that with the introduction of $f$–$P$ droop, the system is more stable compared to a GFL-IBR without the droop control. The frequency-domain analysis can further explain the effect of droop control. The block diagram for GFL-IBR with $f-P$ droop is illustrated in Figure 4.13. In this diagram, "Block-1" is defined using three transfer functions: $G_1(s)$, $G_2(s)$, and $G_3(s)$, where $G_3(s)$ represents the droop transfer function $-s/(\omega_0 \times R)$, and $G_2(s)$ is the transfer function from $P_{\text{ref}}$ to $\Delta\theta_{\text{PCC}}$.

Without the frequency droop control, the net transfer function for "Block-1" is $G_1(s)$. With droop, the transfer function becomes $G_1(s) + G_2(s) \times G_3(s)$. This additional path results in a reduction of the gain of “Block-1” in the frequency range of 1-30 Hz. This reduction is evident from the Bode diagram depicted in Figure 4.12a.

This addition provides additional stability. The Bode diagram of the total loop gain for a compensation level of 63% is presented in Figure 4.12b, where the phase shift occurs at around 15 Hz. At this frequency, GFL without droop control is marginally stable, whereas, with droop control, it indicates stability. This observation coincides with the EMT simulation results in Figure 4.14. The addition of $f-P$ droop in a GFL-IBR can help reduce the sensitivity of the PCC bus voltage angle towards the synchronization angle, thereby mitigating the interaction of series compensation and PLL and enhancing stability.

### 4.5.2 GFM with VSG Control

An alternative control method to synchronize the GFM to the grid is explored: the Virtual Synchronous Generator (VSG) control. VSG control is a widely adopted control mechanism for the synchronization of GFM-based IBR to the grid.

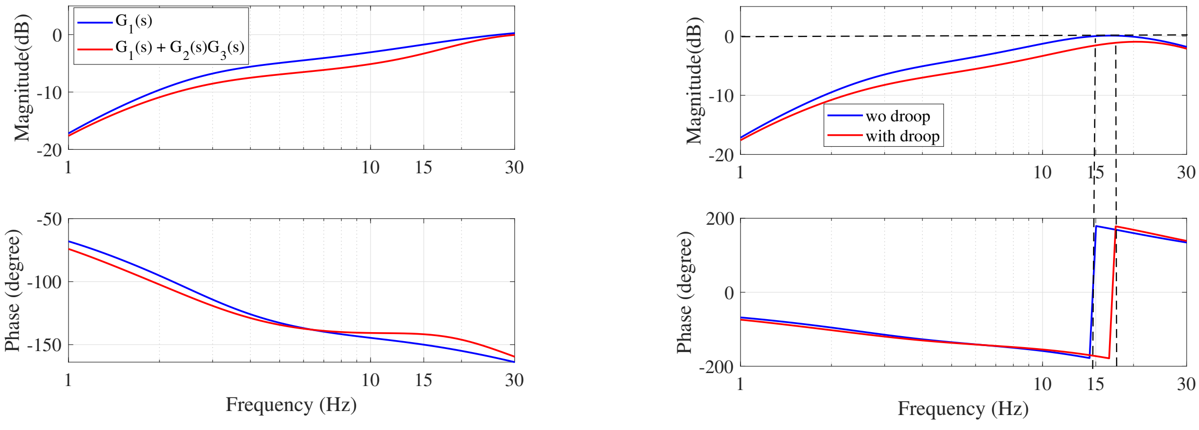

(a)

(b)

Figure 4.12 Frequency domain responses. (a) GFL Block-1. (b) $G_{\text{OL}}$. The red curve represents the response of the system with additional droop control, whereas the blue curve is without droop control. The series compensation level is 63%.

The synchronizing mechanism is similar to that of a synchronous generator and it power-angle relationship is determined by the second-order swing equation [69, 70].

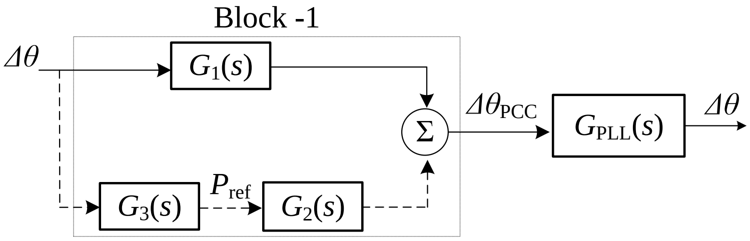

Figure 4.13 Block diagram for frequency-domain analysis of GFL-IBR with additional droop control.

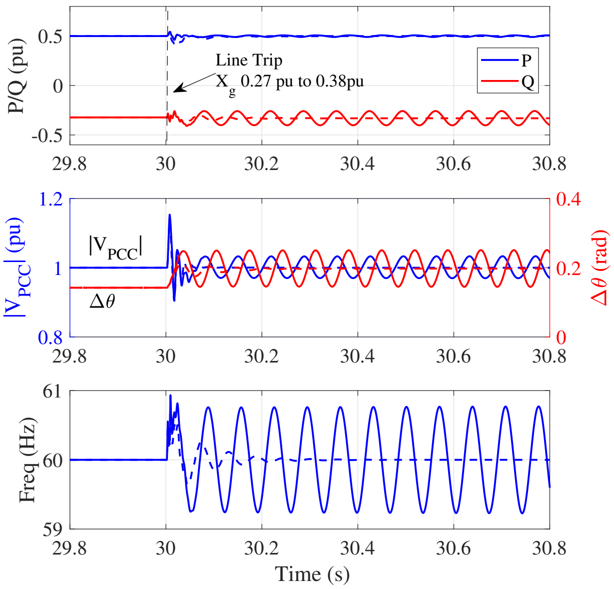

Figure 4.14 Comparison of GFL with and without droop control during the series compensated network. Time-domain responses for the real power $P$, $Q$, $|V_{\text{PCC}}|$, $\Delta\theta$, and frequency(Hz). Solid lines: no droop. Dashed line: with droop. At $t = 30$ s, a line tripping event occurs leaving the IBR radially connected to the RLC network. The effective grid reactance goes from 0.19 pu to 0.38 pu.

The control implementation block diagram is provided in Figure 4.15. Here, $D_p$ is the damping coefficient of the active power loop, and $J$ is virtual inertia. The transfer function of the VSG controller from the net power $P_{\text{ref}} - P$ to the synchronizing angle $\Delta\theta$ is given by:

$$G_{\text{VSG}}(s) = \frac{1}{Js + D_p} \times \frac{\omega_0}{s} \tag{4.7}$$

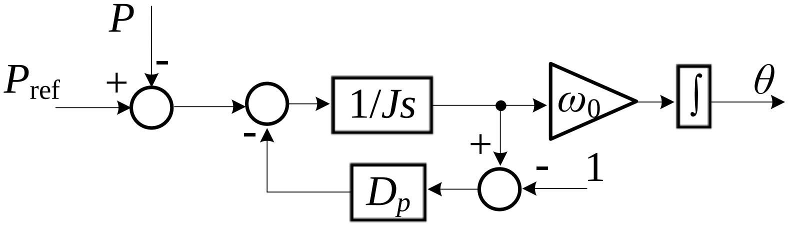

Figure 4.15 Control block diagram of VSG controller adopted for GFM IBR.

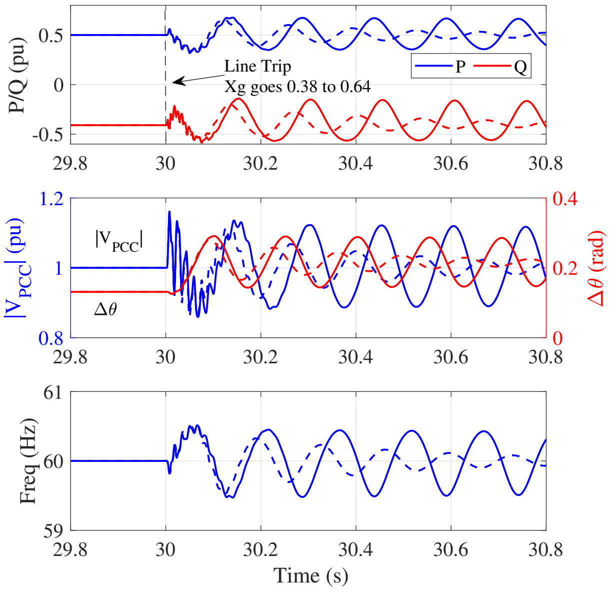

Figure 4.16 Comparison of GFM with different synchronization units when system is connected to series compensated network. Time domain responses for the real power $P$, $Q$, $|V_{\text{PCC}}|$, $\Delta\theta$, and frequency (Hz). Solid lines: $P - f$ droop control; Dashed line: VSG. The system is radially connected to the RLC network at $t = 30$ s, where grid reactance goes from 0.317 pu to 0.635 pu.

For the VSG controller, $J$ is considered as 0.02 pu, and the damping coefficient $D_p$ value is 20. The time domain results comparing the performance of droop-based GFM-IBR and the VSG-based GFM are presented in Figure 4.16. The results indicate that VSG and $P-f$ exhibit slightly worse performance when radially connected to the series compensated network ($K$ = 36.5%). Furthermore, the frequency-domain response of the loop gain (shown in Figure 4.17) indicates that the VSG controller does not help stability since VSG adds additional phase lag. The VSG increases phase lag and and worsens stability.

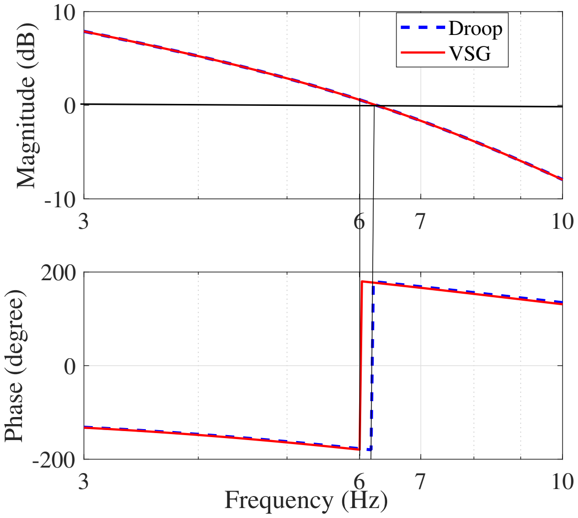

Figure 4.17 Frequency-domain response of the open-loop gain $G_{\mathrm{OL}}$. Red curve: VSG; blue dashed curve: droop control. The series compensation level is 40%.

## 4.6 Conclusion

This work investigates the interactions of series compensation with grid-connected IBRs, specifically GFL and GFM types. The study conducts EMT simulations, analytical model building, eigenvalue analysis, and open-loop frequency-domain analysis to reveal that series compensation may interact with synchronizing units in IBRs and create oscillations. Series compensation can increase the sensitivity of the PCC bus voltage angle towards the synchronizing angle, and introduce phase lag in the real power response towards the synchronizing angle. These factors may lead to interactions with PLL in the GFL-IBR systems and interactions with the power-based synchronization in the GFM-IBR systems, thereby leading to instability.

## Chapter 5: Digital Twin for IBR Power Plant

In this chapter, a digital twin for a IEEE 9 bus is proposed. IEEE-9 bus system consists of an IBR. The digital-twin performs two tasks, estimation of key grid parameters such as grid impedance, and grid voltage magnitude as seen from the IBR view-point. The second task is to run the reduced order model in real-time with the estimated parameters.

### 5.1 Introduction

Inverter-based resources (IBRs), including photovoltaic (PV) systems and wind turbines, are vital in transitioning toward a cleaner and more sustainable energy landscape. Their penetrations in power grids keep increasing. This brings new challenges to the stability and reliability of power systems.

Over the years IBR weak grid instability incidences have been reported in Hydro One, Texas, and Australia [33,34,71]. The task force paper by the IEEE Power & Energy Society IBR subsynchronous oscillation (SSO) task force [3] provides a survey of 19 real-world SSO events associated with IBRs due to either weak grid interconnection or radial interconnection with series capacitors. In addition to oscillations, many other challenges, e.g., large phase-locked-loop (PLL) angle deviation, subcycle overvoltage, AC overcurrent, have also been reported in real-world IBR operation. See e.g. [4–7]. Large PLL angle deviation in the 2021 Texas Odessa disturbances [7] have been demonstrated in computer simulation testbeds in [59], while the mechanism has been provided by the senior authors in [26] by use of a single inverter connected to an infinity bus through a grid impedance.

Consequently, there is a pressing requirement to devise methodologies that can assist system operators in modeling and analyzing intricate stability issues associated to IBRs. Ultimately, these methods should enable the prediction of stability issues and facilitate swift mitigation actions. This proactive approach can certainly enhance the resiliency and reliability of the power grid.

Digital twin technologies utilize advanced modeling, real-time simulation, real-time data streaming, and data analytics techniques to replicate an actual power under varying operating conditions [72]. Currently majority of the applications of digital twins are limited to small-scale individual systems, e.g., DC-DC power electronic converters' conditioning monitoring for MOSFET and capacitor degradation [73], a single-phase DC-AC converter's parameter identification [74], power electronics converter online diagnostic analysis [75], offshore wind turbine converters remaining useful life prediction [76], and a solar PV energy conversion unit fault diagnosis [77]. Very few applications are associated with a system with multiple units and they are designed for particular applications, e.g., unit commitment of networked microgrids [78], where virtual models are for steady-state analysis or power flow type of analysis based on energy management system (EMS) data [79].

To develop a digital twin as a virtual replica or real-time dynamic simulation of a real-world power system encompassing its many physical components, operational characteristics, and dynamic behaviors, is a challenging task. In [80], the authors from Australia Electric Market Operator (AEMO) introduce the concept of a power system digital twin to represent the Australian bulk power grid consisting of 55 GW generation and 40,000 km transmission line network. The authors have successfully implemented a synthetic model (S-NEM2300 [81]) in the real-time simulator. However, the full-fledged model of the power system requires a substantial number of processors/-cores to facilitate real-time simulations, raising concerns about the practical implementation of their digital twin.

In this work, the aim is to develop a digital twin for a grid interfaced with IBR. This digital twin must accurately capture the critical dynamics of IBR grid operations. Given the complexity of modeling every inverter within an IBR power plant, which typically comprises numerous solar PVs or wind turbines, and the impracticality of modeling an entire power grid as highlighted by the experiences of the Australian Energy Market Operator (AEMO) [80], we propose a simplified yet effective approach. We model a single IBR connected to an infinite bus, representing a realistic IBR power plant grid interconnection. Our extensive experience in IBR modeling confirms that this single-IBR infinite bus configuration effectively captures several real-world phenomena, including subcycle overvoltage upon inverter momentary cessation [82], AC overcurrent during grid faults [83], significant PLL angle deviation following grid voltage dips [26], and various types of oscillations [84–86].

In this approach, the grid is modeled as a Thévenin equivalent, defined by a stable voltage source situated behind an impedance. When the grid encounters contingencies, both the impedance and voltage of this model are subject to change. Consequently, it is essential for the digital twin of the IBR power plant to dynamically update these parameters using data measured in real-time. To enable the digital twin to perform real-time simulations effectively while conserving computational resources, we have developed a reduced-order model. This model represents the IBR power plant as a controllable current source, synchronized through a Phase-Locked Loop (PLL), ensuring accurate and efficient simulation capabilities [87].

The culmination of this research is a reconfigurable system-on-chip (SoC)-based digital twin for the IBR power plant. This system is capable of estimating critical grid parameters from measured data and performing real-time simulations to evaluate grid performance. SoC technology, which is increasingly recognized in the power systems domain, facilitates the integration of various functionalities—such as power system monitoring, fault detection, and control algorithms—into a single platform. This integration not only reduces hardware complexity but also lowers costs [88, 89].

In summary, our proposed digital twin framework leverages the reconfigurability of SoCs to provide a flexible and adaptable tool that can estimate vital grid parameters and offer real-time simulation capabilities to assess the performance of grids interfaced with IBRs. By incorporating data from a variety of grid sensors and external sources, the digital twin dynamically updates its model based on the estimated grid impedance to accurately reflect current grid conditions. This enables the preemptive identification of potential stability issues and the evaluation of mitigation strategies before their manifestation in the physical grid. For demonstration purposes, we utilize a modified IEEE 9-bus system with an IBR in the physical setup, while implementing the digital twin on a National Instruments cRIO-9063 platform. A visual depiction of this paper's scope is presented in Figure 5.1.

## 5.2 The Test Bed

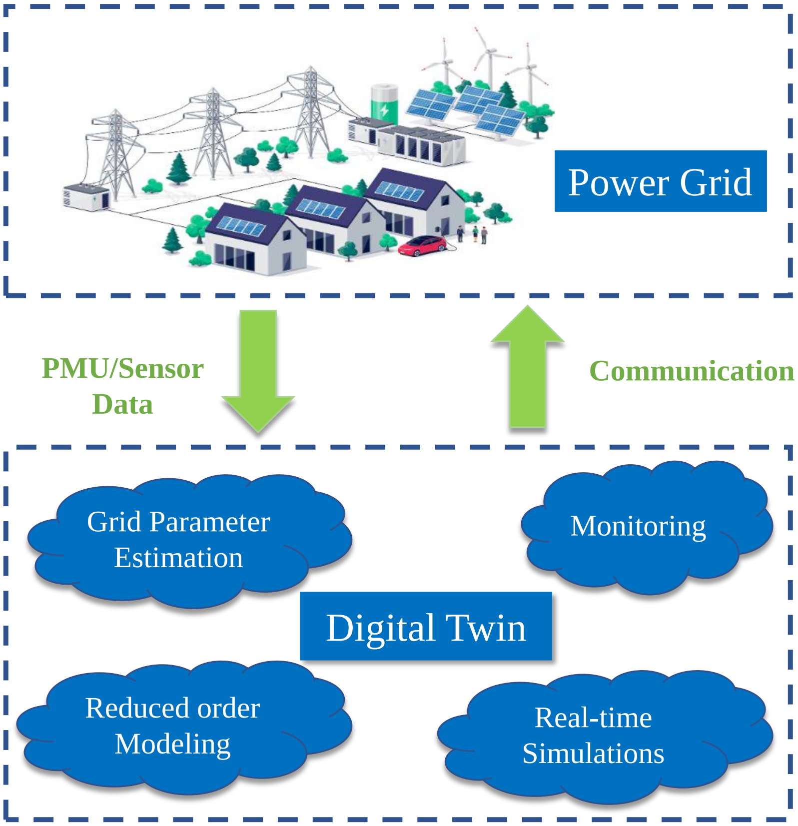

Figure 5.1 Pictorial representation showcasing the comprehensive scope and functionality of the implemented digital twin.

The testbed is illustrated in Figure 5.2, showcasing a system configured as a modified IEEE-9 bus system. This system operates at a transmission network voltage of 230 kV. Synchronous generators, modeled as constant voltage sources, are connected at Buses $B_1$ and $B_2$. The various line impedances and system parameters are tabulated in Table 5.1. An IBR, following the grid, is connected at Bus $B_3$, which serves as the Point of Common Coupling (PCC) bus. An IBR, following the grid, is connected at Bus $B_3$, which serves as the Point of Common Coupling (PCC) bus.

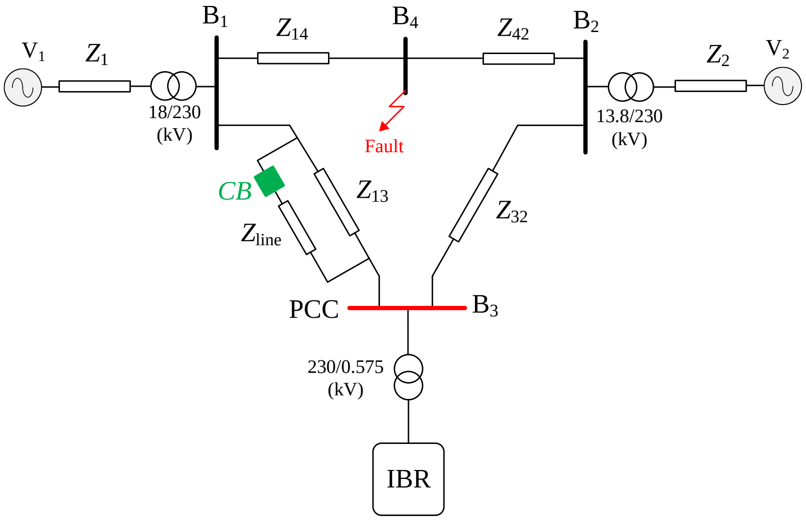

Figure 5.2 Modified IEEE-9 bus system. IBR is connected to bus B3.

Table 5.1 Parameters for modified IEEE-9 bus system.

| Description | Value (SI, pu) |
|---|---|
| Power Base | 100 MVA |
| $V_1$ | $18\angle(10^\circ)$ kV |
| $V_2$ | $13.8\angle(0^\circ)$ kV |
| Transmission Line Impedance | |
| $Z_1$, $Z_2$, $Z_{\text{line}}$, $Z_{32}$ | $0.201\angle(84.28^\circ)$ |
| $Z_{14}$, $Z_{42}$ | $0.1005\angle(84.28^\circ)$ |
| $Z_{13}$ | $1.005\angle(84.28^\circ)$ |

The inverter control consisting of fast inner current tracking and slower outer power or voltage regulation is implemented in the $dq$ reference frame based on the PLL. The PLL frame's $d$ axis is aligned with the point of common coupling (PCC) bus voltage space vector at steady state. A synchronous reference frame PLL (SRF-PLL) is used as the synchronizing unit. This SRF-PLL has the PCC bus three-phase voltage as the input and outputs an angle tracking the PCC bus voltage's angle ($\theta_{\text{PLL}}$). This angle is further used in $dq/abc$ and $abc/dq$ frame conversion in the inverter control. The control topology of the IBR is presented in Figure 5.3. Besides the PLL, the inverter control consists of fast inner current control and outer control for real power and reactive power (or voltage) regulation. Proportional integral (PI) controllers are used for signal tracking in both inner and outer control. The outer control generates reference currents for the inner current control. The parameters are listed in Table 5.2.

Table 5.2 Circuit and control parameters.

| Description | Parameter | Value (SI, pu) |
|---|---|---|
| Power Base | $S_b$ | 100 MVA |
| Inverter Voltage | $V_b$ | 575 V |
| Nominal Frequency | $f_0$ | 60 Hz |
| DC Voltage | $V_{DC}$ | 1100 V |
| Choke Filter | $X_f$ $R_f$ | 0.15, 0.15/50 |
| Inner Loop | $k_{ip}$, $k_{ii}$ | 0.3, 5 |
| Outer Loop $d$, $P$ control | $k_{Pp}$, $k_{Pi}$ | 0.1, 30 |
| Outer Loop $q$, Q control | $k_{Vp}$, $k_{Vi}$ | 0.2, 20 |
| PLL | $k_{\text{PLL}p}$, $k_{\text{PLL}i}$ | 60, 1400 |

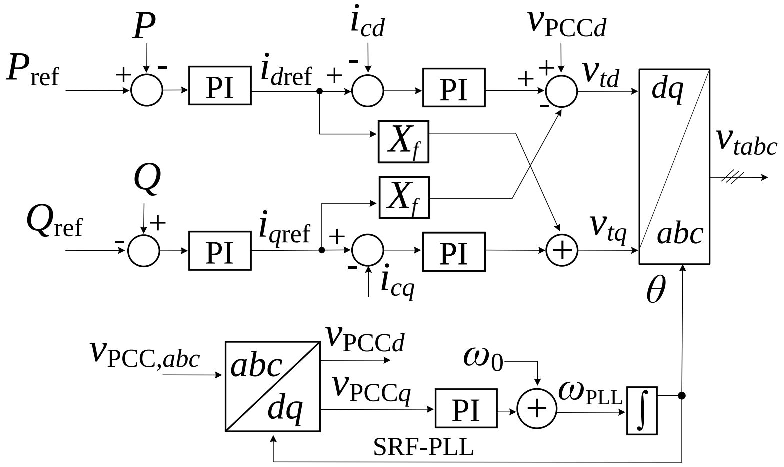

Figure 5.3 Control structure of the GFL IBR.

## 5.3 Thévenin Equivalent Representation

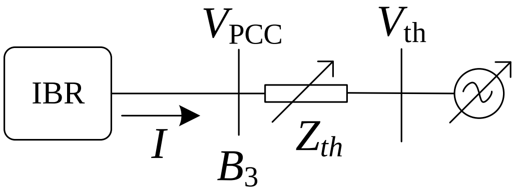

Figure 5.4 The simplified representation of grid-connected IBR.

From the perspective of the IBR, the grid connection at Bus $B_3$ is modeled as a Thévenin equivalent circuit. This includes a Thévenin equivalent impedance, denoted as $Z_{th}$, and a Thévenin equivalent voltage, represented by $\overline{V}_{th}$. The parameters of the Thévenin circuit are derived using the Least Square Estimation (LSE) method.

For the LSE algorithm, the measurements include the real power $P$ and the reactive power $Q$. The known variables in this estimation are the voltage magnitude $V_{PCC}$ and the phase angle $\delta_{PCC}$. As illustrated in Figure 5.4, which depicts the system as a two-bus model, the following relationships are established, assuming that the Thévenin resistance $R_{th}$ is approximately zero:

$$\begin{aligned} z_1 &= P = \frac{V_{\text{PCC}} V_{th} \sin \delta_{\text{PCC}}}{X_{th}} \\ z_2 &= Q = \frac{V_{\text{PCC}}^2 - V_{\text{PCC}} V_{th} \cos \delta_{\text{PCC}}}{X_{th}} \end{aligned} \tag{5.1}$$

### 5.3.1 LSE Algorithm

The aim of the algorithm is to estimate the Thévenin grid reactance ($X_{th}$) and the Thévenin grid voltage magnitude ($V_{th}$). These are treated as two state variables, denoted as $x_1$ and $x_2$ respectively.

With this assumption in place, (5.1) can be reformulated as follows:

$$\begin{aligned} h_1(x) &= \frac{V_{PCC} x_2 \sin \delta_{PCC}}{x_1} \\ h_2(x) &= \frac{V_{PCC}^2 - V_{PCC} x_2 \cos \delta_{PCC}}{x_1} \end{aligned} \tag{5.2}$$

The objective of the optimization problem in state estimation is to minimize the error between the measured values and the values estimated by the system model. The problem is formulated as follows:

### 5.3.2 Objective Function

The goal is to find the state vector $x = [x_1, x_2]$ that minimizes the sum of the squared differences between the observed measurements $z = [z_1, z_2]$ and the measurements predicted by the state model. The measurements are $z_1 = P$ and $z_2 = Q$. Mathematically, the problem is formulated as:

$$\min_x J(x) = ||z - h(x)||^2 \tag{5.3}$$

where $h(x) = [h_1(x); h_2(x)]$ represents the nonlinear measurement function, which maps the state vector $x$ to the predicted measurements.

### 5.3.3 Jacobian Matrix

The Jacobian matrix $J(x)$ of partial derivatives, with respective to state variables $x_1$ and $x_2$ is:

$$H(x) = \begin{bmatrix} \frac{\partial h_1}{\partial x_1} & \frac{\partial h_1}{\partial x_2} \\ \frac{\partial h_2}{\partial x_1} & \frac{\partial h_2}{\partial x_2} \end{bmatrix} \tag{5.4}$$

where each partial derivative is computed based on (5.2).

### 5.3.4 Update Rule

The update to the state vector is performed using the Newton-Raphson method:

$$x^{k+1} = x^k + (H(x^{(k)})^T H(x^{(k)}))^{-1} H(x^{(k)})^T e^{(k)} \tag{5.5}$$

where $e^{(k)} = z - h(x^{(k)})$ represents the error vector at iteration $k$. The LSE algorithm is favored because of its computational speed and ease of implementation, both essential for rapid decision-making.

## 5.4 Reduced-Order dq-Frame Model in Per Unit

For power grid dynamic studies, a grid-following IBR is often modeled as a controllable current source [17, 87]. It is a common practice in system-level dynamic studies to ignore the fast inner control loop, PLL, and line electromagnetic transient (EMT) dynamics, as shown in the WECC IBR generic model set REGC_A [90]. As indicated by [90], this simplification is not suitable for weak grid conditions. One of the senior authors showed that inclusion of the PLL dynamics in the current source representation can significantly increase the accuracy of stability analysis, especially for weak grid scenarios [87]. In this work, this type of reduced-order model is adopted to implement the digital twin. Figure 5.4 shows the circuit topology in per unit and the IBR represented as a current source, synchronized to the grid through a PLL.

For the reduced-order model, the inner current control loop and the line EMT dynamics are ignored. The justification is as follows. The inner loop typically operates at a much faster time scale compared to the outer control. This time-scale separation allows us to approximate the inner loop dynamics as a fast, quasi-steady-state process. A distinct advantage of model reduction is the reduced computation burden. This advantage has also been reported in [91] where a three-phase current source representation is adopted for a grid-following inverter. Compared to [91], the modeling framework of the digital twin is based on $dq$-frames, which further saves computing. A key technology of $dq$-frame representation is that instead of treating $\theta_{\text{PLL}}$ (the angle of the PLL viewed from the static frame) as a state variable, we use $\delta_{\mathrm{PLL}}$ (the angle of PLL viewed from the grid $dq$ frame) as a state variable. The grid $dq$ frame aligns with the constant grid voltage's space vector and its position against the static frame is $\omega_0 t$, where $\omega_0$ is the nominal angular frequency 377 rad/s. Therefore, $\delta_{\mathrm{PLL}} = \theta_{\mathrm{PLL}} - \omega_0 t$. The model can be divided into four sections: (a) outer loop, (b) PLL, (c) grid effect, and (d) frame conversion, as shown in Figure 5.5.

### 5.4.1 Outer Loop and PLL

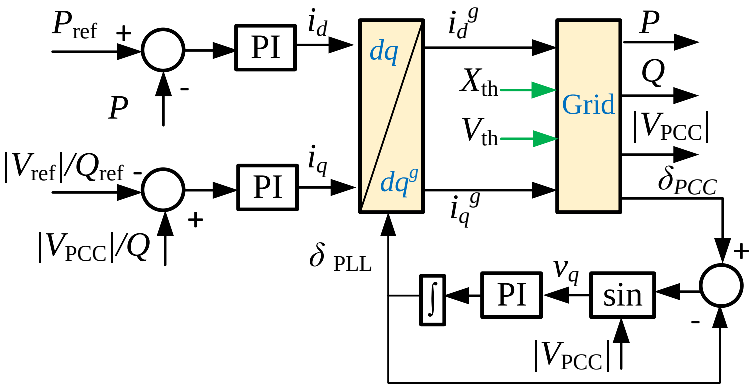

Figure 5.5 Reduced-order $dq$-frame model of the grid-connected IBR.

As mentioned earlier, the outer loop is in real power ($P$) and voltage control ($|V_{\mathrm{PCC}}|$). The two controls help track the power reference and voltage reference and generate the converter currents $i_d$ and $i_q$ order in the PLL frame. The PLL takes the PCC bus voltage's angle $\delta_{\mathrm{PCC}}$ as the input and outputs its own angle $\delta_{\mathrm{PLL}}$. At steady state, these two angles align with each other. During transients, they are different. The model of the PLL in the $dq$ frame is adopted from [87].

### 5.4.2 Grid Effect

From Figure 5.4, the algebraic relationship between the PCC bus voltage, current, and grid voltage (in grid frame of reference) can be set up as follows.

$$\overline{V}_{\text{PCC}} = (R_{th} + jX_{th})\bar{I} + \overline{V}_{th} \tag{5.6}$$

where $\overline{V}_{\text{PCC}} = v_d^g + jv_q^g$, $\bar{I} = i_d^g + ji_q^g$, and $\overline{V}_{th} = |V_{th}|$. The superscript $g$ notates the grid dq frame. From (5.6), the components $v_d^g$ and $v_q^g$ are:

$$v_d^g = R_{th}i_d^g - X_{th}i_q^g + |V_{th}|,\ v_q^g = R_{th}i_q^g + X_{th}i_d^g \tag{5.7}$$

In addition, the PCC bus voltage magnitude and angle can be calculated as $|V_{\text{PCC}}| = \sqrt{(v_d^g)^2 + (v_q^g)^2}$ and $\delta_{\text{PCC}} = \tan^{-1}(\frac{v_q^g}{v_d^g})$.

The real and reactive power exported by the IBR is calculated as:

$$P = v_d^g i_d^g + v_q^g i_q^g,\ Q = -v_d^g i_q^g + v_q^g i_d^g \tag{5.8}$$

This completes the grid block. Here, $X_{th}$ and $V_{th}$ are the Thévénin Equivalent impedance and voltage estimated by LSE.

### 5.4.3 Frame Conversion

As discussed earlier, the IBR is synchronized with the power grid using a PLL. The PLL provided us with the necessary synchronization angle $\delta_{\text{PLL}}$. Since the converter control is working in the PLL frame, we need to convert the currents from the PLL frame to the grid reference frame [87]:

$$(i_d + ji_q)e^{j\delta_{\text{PLL}}} = i_d^g + ji_q^g. \tag{5.9}$$

The blocks shown in Figure 5.5 are implemented in an SoC chip to represent the grid-connected IBR power plant.

## 5.5 Hardware-in-Loop Setup

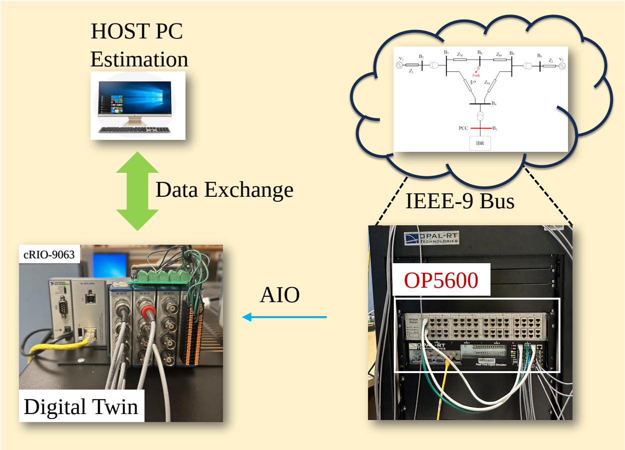

Figure 5.6 Hardware testbed including NI cRIO-9063 (digital-twin) and OP5600 real-time simulator for the system under test.

The digital twin setup includes two primary components:

1. Digital Simulator: This segment employs the OPAL-RT OP5600 platform to execute a real-time simulation of a modified IEEE-9 bus power grid. Analog signals, encompassing three-phase voltage and current waveform, are generated and outputted through dedicated analog output modules.
2. NI cRIO-9063: This element serves as the digital twin's core. It is a robust, compact reconfigurable input/output (cRIO) controller that integrates a reconfigurable Xilinx Zynq-7000 System on Chip (SoC). The programming of this controller is facilitated using NI LabVIEW FPGA, and it interfaces with external systems through four 16-bit c-Series modules. For data acquisition, the NI-9215 module is employed as a four-channel analog input module, while the NI-9264 module handles analog outputs.

Furthermore, the host computer runs the LSE algorithm in real-time for estimating impedance and voltage magnitude Communication between the host and the cRIO is managed via an Ethernet link. The cRIO acquires and transmits signal data to the host, where the LSE algorithm processes this data to estimate the required state variables. These variables are subsequently relayed back to the cRIO, enabling the digital twin to accurately emulate the simplified model of the power grid. Figure 5.6 presents the hardware setup.

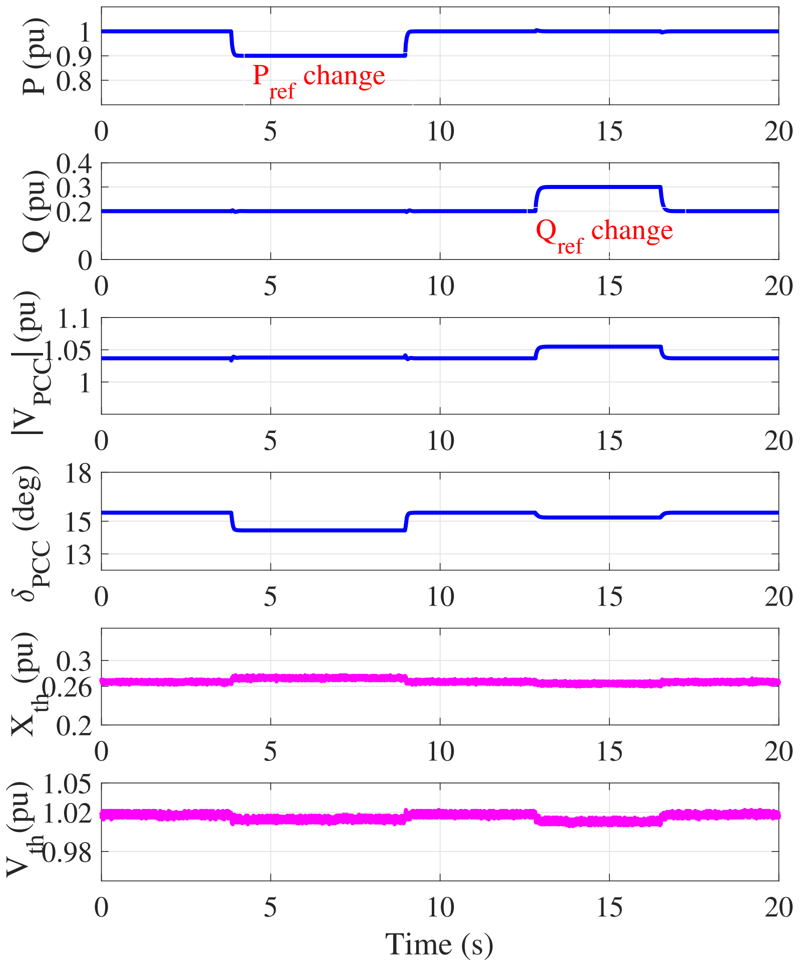

Figure 5.7 Time-domain responses of real power $P$, reactive power $Q$, $V_{\text{PCC}}$, $\delta_{\text{PCC}}$ and the estimated $X_{th}$ and $V_{th}$ from the digital twin. The results showcase the performance of LSE algorithm, when $P_{\text{ref}}$ and $Q_{\text{ref}}$ are varied.

## 5.6 Results

### 5.6.1 Thévénin Grid Reactance and Voltage Estimation

The LSE algorithm is implemented in real-time using LabVIEW software. In the test system, which utilizes the modified IEEE-9 bus configuration, the IBR operates in P/Q control mode. Figure 5.7 displays the results from the digital twin, highlighting the estimated Thévénin grid reactance and voltage as determined by the LSE algorithm. To evaluate the algorithm's performance, the reference values for real power ($P_{\text{ref}}$) and reactive power ($Q_{\text{ref}}$) controlled by the IBR are varied systematically. The estimated Thévénin reactance is $j0.26$pu, and voltage is $\approx$ 1.024 pu. It has been observed that despite changes in the power settings of the IBR, the estimated grid impedance and the voltage of the Thévénin equivalent circuit remain constant. This consistency suggests a robust performance of the LSE algorithm in maintaining accurate estimations regardless of variations in the IBR's power output. The results presented are specifically from measurements and calculations at Bus $B_3$ (PCC bus).

The results were confirmed through theoretical calculations using the conventional $Y$-bus matrix approach. For the system analyzed (see Figure 5.2), the $Y$-bus matrix is presented in (5.10):

$$\begin{bmatrix} \frac{1\angle 10^\circ}{Z_1} \\ \frac{1\angle 0^\circ}{Z_2} \\ I_3 \\ 0 \end{bmatrix} = \underbrace{\begin{bmatrix} \frac{1}{Z_1}+\frac{1}{Z_{13}}+\frac{1}{Z_{14}} & 0 & -\frac{1}{Z_{13}} & -\frac{1}{Z_{14}} \\ 0 & \frac{1}{Z_2}+\frac{1}{Z_{42}}+\frac{1}{Z_{32}} & -\frac{1}{Z_{32}} & -\frac{1}{Z_{42}} \\ -\frac{1}{Z_{13}} & -\frac{1}{Z_{32}} & \frac{1}{Z_{13}}+\frac{1}{Z_{32}} & 0 \\ -\frac{1}{Z_{14}} & -\frac{1}{Z_{42}} & 0 & \frac{1}{Z_{14}}+\frac{1}{Z_{42}} \end{bmatrix}}_{Y_{Bus}} \begin{bmatrix} V_1 \\ V_2 \\ V_3 \\ V_4 \end{bmatrix} \tag{5.10}$$

$$\begin{bmatrix} V_1 \\ V_2 \\ V_3 \\ V_4 \end{bmatrix} = \underbrace{\begin{bmatrix} 0.1251 & 0.0759 & 0.1027 & 0.1005 \\ 0.0759 & 0.1251 & 0.0983 & 0.1005 \\ 0.1027 & 0.0983 & 0.2 & 0.1005 \\ 0.1005 & 0.1005 & 0.1005 & 0.1507 \end{bmatrix} \angle 84.3^\circ}_{Z_{Bus}} \begin{bmatrix} \frac{1\angle 10^\circ}{Z_1} \\ \frac{1\angle 0^\circ}{Z_2} \\ I_3 \\ 0 \end{bmatrix} \tag{5.11}$$

To evaluate the Thévenin equivalent impedance, the impedance matrix $Z_{Bus} = Y_{Bus}^{-1}$ is evaluated. The results are presented in (5.11). The Thévenin equivalent circuit, as seen from Bus $B_3$, is derived by expanding the third row of (5.11):

$$V_3 = \underbrace{Z_{13}\frac{1\angle 10^\circ}{Z_1} + Z_{23}\frac{1\angle 0^\circ}{Z_2}}_{V_{th}} + Z_{33}I_3 \tag{5.12}$$

In this expression, $Z_{33}$ represents the Thévenin equivalent impedance. The calculated values are $Z_{th} = Z_{33} = 0.2\angle 84.2894^\circ$, and $V_{th} = 0.9962\angle 5.1^\circ$. These theoretical values closely match the real-time estimated results, validating the accuracy of the algorithm. Due to the omission of grid impedance's resistive part and with the assumption that the grid voltage as seen from bus $B_3$ as zero in the estimation algorithm, the estimated $X_{th}$ and $V_{th}$ are slightly larger compared to the true value. The estimated values are now utilized within the digital twin to accurately replicate the modified IEEE-9 bus system.

### 5.6.2 Case Study 1: Three-phase Fault

The first test scenario involves the application of a three-phase fault at Bus 4, which persists for six cycles (starting at $t = 2s$) and the fault impedance is assumed to be $j0.1$ pu. The LSE algorithm operates in real-time to estimate changes in the Thévénin grid impedance and voltage, leading to immediate updates in the digital twin model. The estimated values during fault, for $X_{th}$ and $V_{th}$ are $0.19j$ pu and $0.6j$ pu respectively. The theoretically calculated (based on (5.11)) values are $X_{th} = 0.1512j$, and $V_{th} = 0.5970\angle 6.7^\circ$.

The side-by-side comparison between the actual system and the developed digital twin for this scenario are detailed in Figure 5.8. The results presented demonstrates that the algorithm and the developed digital twin provide an accurate reflection of the modified IEEE-9 bus system's response to a three phase fault. These scenarios highlight the robustness and reliability of the LSE algorithm in adapting to dynamic changes and ensuring the digital twin remains an accurate representation of the actual system.

### 5.6.3 Case Study 2: Line Tripping Event

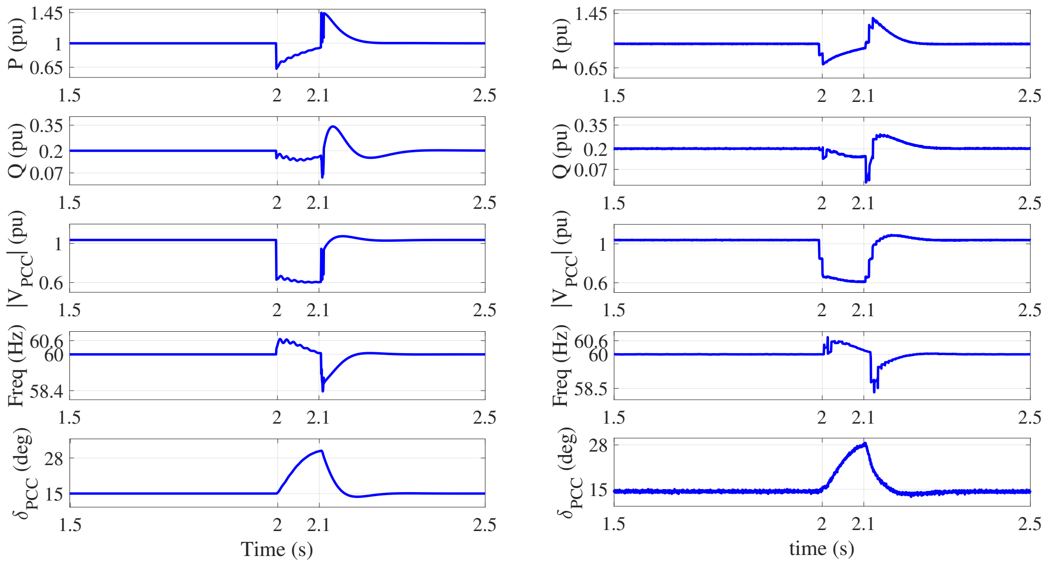

(a) (b)

Figure 5.8 Time-domain responses of real power $P$, reactive power $Q$, $V_{\text{PCC}}$, $\theta_{\text{PCC}}$, Frequency (Hz) for a three-phase fault at Bus $B_4$ for 6 cycles. (a) Modified IEEE 9 bus system. (b) Digital Twin.

For the second case study, a line tripping event is caused by the opening of breaker “CB” (at $t$ = 1s), which results in the disconnection of the transmission line with impedance $Z_{\text{line}}$. Theoretical calculation results in the Thévénin grid reactance and voltage as $X_{th} = 0.28j$, and $V_{th} = 0.9963\angle 4^{\circ}$, while the estimates from the LSE algorithm are $X_{th} = 0.34j$, and $V_{th} = 1.026$ pu.

The real-time application of the LSE algorithm allows for the continuous adjustment of the Thévénin grid impedance and voltage in the digital twin model, as illustrated in Figure 5.5. The results of this adaptation are showcased in Figure 5.9, confirming that the algorithm effectively replicates the actual dynamics of the IEEE-9 bus system under such disturbances. This demonstrates that the developed digital twin reflects the behavior of the actual system. The successful implementation of this model showcases its practicality and effectiveness.

## 5.7 Conclusion

In summary, this study introduces a digital twin specifically designed for a grid-connected IBR power plant, which has been effectively implemented. By integrating a reduced-order model of the IBR system and updating the grid impedance with real-time data, the digital twin accurately reflects and replicates the behavior of the physical system, while ensuring computational efficiency for the SoC. The effectiveness of the digital twin is validated by introducing a three-phase fault and line-tripping scenario. The performance of the implemented developed digital twin confirms its capability to closely emulate its physical counterpart, demonstrating its significant potential.

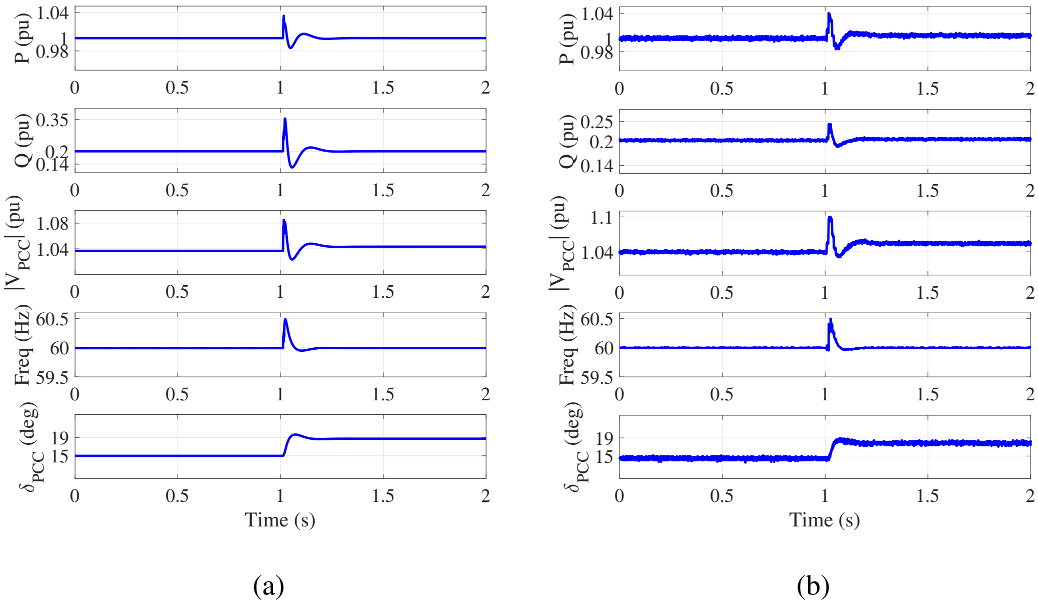

Figure 5.9 Time-domain responses of real power $P_{B1}$, reactive power $Q_{B1}$, $V_{\text{PCC}}$, $\theta_{\text{PCC}}$, frequency (Hz) for a line tripping event between bus $B_1$ and $B_3$. (a) Modified IEEE 9 bus system (b) Digital Twin.

# Chapter 6: Conclusions and Future Works

## 6.1 Conclusions

This dissertation thoroughly investigates the stability challenges associated with integrating IBRs into power grids using a multilayered approach that combines time-domain simulations, analytical modeling, and hardware validations.

The first area of focus was on the performance of IBRs in weak grids. The primary cause of instability here is identified as the high sensitivity of voltage to current injections in weak grids, a phenomenon typically associated with voltage stability issues. Various control structures, including GFM IBRs, were modeled and analyzed. By implementing a coordination scheme that utilizes feedback from the PCC bus voltage after passing it through a high-pass filter, the system's stability margin significantly improved.

The study also examined the interactions between series compensation and grid-connected IBRs. EMT simulations, analytical model building, eigenvalue analysis, and open-loop frequency-domain analysis were conducted to demonstrate that series compensation may interact with synchronizing units in IBRs, potentially causing oscillations. Series compensation was found to increase the sensitivity of the PCC bus voltage angle towards the synchronizing angle and introduce a phase lag in the real power response towards the synchronizing angle. These factors may lead to interactions with PLL in GFL-IBR systems and with power-based synchronization in GFM-IBR systems, resulting in instability.

Finally, the dissertation implemented and tested a digital twin specifically designed for a grid-connected IBR power plant. By integrating a reduced-order model of the IBR system and updating the grid impedance with real-time data, the digital twin accurately reflects and replicates the behavior of the physical system while ensuring computational efficiency for the SoC. The effectiveness of the digital twin was validated through scenarios involving a three-phase fault and line tripping. The performance of the developed digital twin confirms its capability to closely emulate its physical counterpart, demonstrating significant potential.

## 6.2 Future Work

Previously, in Chapters 3 and 4, the focus was primarily on modeling and analyzing single IBRs individually. Moving forward, the aim is to simulate more complex networks involving multiple IBRs, such as GFL and GFM systems. A key area of investigation will be how various IBR control systems interact under conditions of weak grid interconnections or when integrated with series-compensated lines. Additionally, the modeling of other types of controllers, such as proportional resonant controllers and controller saturation, will also be considered. The focus will also expand to include large-scale power system modeling. Currently, the grid is modeled as an infinite bus, ignoring the complexities of the grid. To produce more accurate analysis, the grid should be modeled using a large-scale power system.

Past studies were limited to analyzing only the fundamental component of the power system, neglecting the effects of higher harmonics. Future work will explore the impact of multiple harmonics, such as the second and third, requiring the development of a more complex nonlinear model. This model will facilitate stability studies under unbalanced grid conditions, providing deeper insights into harmonic influences on system behavior.

Another objective is to enhance the functionality of the digital twin system. Currently, the digital twin only estimates the grid impedance and the grid voltage magnitude, assuming the equivalent grid resistance and the grid voltage angle are zero. The state estimation algorithm will be improved to estimate more parameters. Furthermore, plans include incorporating more sophisticated real-world communication protocols, such as IEEE C37.118-2011, and integrating real-world phasor measurement units. These enhancements will enable the digital twin to more accurately emulate complex power grid scenarios, improving its utility and relevance in real-world applications.

# References

[1] H. Ritchie, M. Roser, and P. Rosado, “Renewable energy,” *Our World in Data*, 2020, https://ourworldindata.org/renewable-energy.

[2] A. Yazdani and R. Iravani, *Voltage-sourced converters in power systems: modeling, control, and applications*. John Wiley & Sons, 2010.

[3] Y. Cheng, L. Fan, J. Rose, F. Huang, J. Schmall, X. Wang, X. Xie, J. Shair, J. Ramamurthy, N. Modi, C. Li, C. Wang, S. Shah, B. C. Pal, Z. Miao, A. Isaacs, J. Mahseredjian, and Z. J. Zhou, “Real-world subsynchronous oscillation events in power grids with high penetrations of inverter-based resources,” *IEEE Transactions on Power Systems*, pp. 1–1, 2022.

[4] NERC, “1200 MW Fault Induced Solar Photovoltaic Resource Interruption Disturbance Report: Southern California 8/16/2016 Event,” North American Electric Reliability Corporation, Tech. Rep., 06 2017.

[5] Joint NERC and WECC Staff. (2018) (2018, February) 900 MW Fault Induced Solar Photovoltaic Resource Interruption Disturbance Report: Southern California Event: October 9, 2017.

[6] Joint NERC and WECC Staff Report. (2020, November) San Fernando Disturbance, South California Event: July 7, 2020.

[7] Joint NERC and Texas RE Staff Report. (2021, September) Odessa Disturbance.

[8] M. Nagpal, M. Jensen, M. Higginson *et al.*, “Protection challenges and practices for interconnecting inverter based resources to utility transmission systems,” *IEEE Power Energy Soc.*, pp. 1–65, 2020.

[9] North American Electric Reliability Corporation (NERC), “Integrating inverter-based resources into low short circuit strength systems,” North American Electric Reliability Corporation (NERC), Reliability Guidelines, November 2017, available: https://www.nerc.com/comm/RSTC_Reliability_Guidelines/Item_4a._Integrating%20_Inverter-Based_Resources_into_Low_Short_Circuit_Strength_Systems_-_2017-11-08-FINAL.pdf.

[10] Y. Xu, “Modeling, control and analysis of inverter-based generators in the power grids,” Ph.D. dissertation, University of South Florida, 2021.

[11] “Ieee guide for planning dc links terminating at ac locations having low short-circuit capacities,” *IEEE Std 1204-1997*, pp. 1–216, 1997.

[12] Y. Li, L. Fan, and Z. Miao, “Stability control for wind in weak grids,” *IEEE Transactions on Sustainable Energy*, vol. 10, no. 4, pp. 2094–2103, 2019.

[13] A. Egea-Alvarez, S. Fekriasl, and O. Gomis-Bellmunt, “Advanced vector control for voltage source converters connected to weak grids,” in *2016 IEEE Power and Energy Society General Meeting (PESGM)*, 2016, pp. 1–1.

[14] L. Fan, “Modeling type-4 wind in weak grids,” *IEEE Transactions on Sustainable Energy*, vol. 10, no. 2, pp. 853–864, 2018.

[15] E. Muljadi, C. Butterfield, B. Parsons, and A. Ellis, “Effect of variable speed wind turbine generator on stability of a weak grid,” vol. 22, pp. 29–36, Mar. 2007.

[16] Y. Li, L. Fan, and Z. Miao, “Wind in weak grids: Low-frequency oscillations, subsynchronous oscillations, and torsional interactions,” *IEEE Transactions on Power Systems*, vol. 35, no. 1, pp. 109–118, 2019.

[17] L. Fan and Z. Miao, “An explanation of oscillations due to wind power plants weak grid interconnection,” *IEEE Transactions on Sustainable Energy*, vol. 9, no. 1, pp. 488–490, 2018.

[18] L. Fan, R. Kavasseri, Z. L. Miao, and C. Zhu, “Modeling of dfig-based wind farms for ssr analysis,” vol. 25, no. 4, pp. 2073–2082, 2010.

[19] Z. Miao, “Impedance-model-based SSR analysis for type 3 wind generator and series-compensated network,” *IEEE Transactions on Energy Conversion*, vol. 27, no. 4, pp. 984–991, 2012.

[20] R. Mittal, Z. Miao, and L. Fan, “Stability enhancement for ibrs operating in weak grids through proper coordination and control,” *IEEE Transactions on Energy Conversion*, pp. 1–11, 2024.

[21] ——, “Grid forming inverter: Laboratory-scale hardware test bed setup and weak grid operation,” in *2021 North American Power Symposium (NAPS)*, 2021, pp. 1–6.

[22] R. Mittal and Z. Miao, “Analytical model of a grid-forming inverter,” in *2022 IEEE Power Energy Society General Meeting (PESGM)*, 2022, pp. 1–5.

[23] L. Fan and Z. Miao, “Modeling and stability analysis of inverter-based resources.”

[24] R. Teodorescu, M. Liserre, and P. Rodriguez, *Grid converters for photovoltaic and wind power systems*. John Wiley & Sons, 2011, vol. 29.

[25] “Grid-forming technology: An overview of the technology, benefits, and applications,” North American Electric Reliability Corporation (NERC), Tech. Rep., 2023. [Online]. Available: https://www.nerc.com/comm/RSTC_Reliability_Guidelines/White_Paper_Grid_Forming_Technology.pdf

[26] L. Fan, Z. Wang, and Z. Miao, “Large angle deviation in grid-following IBRs upon grid voltage dip,” *IEEE Transactions on Energy Conversion*, 2023.

[27] P. Kundur, *Power system stability and control*. Tata McGraw-Hill Education, 1994.

[28] J. Löfberg, “Yalmip : A toolbox for modeling and optimization in matlab,” in *In Proceedings of the CACSD Conference*, Taipei, Taiwan, 2004.

[29] MathWorks, “linmod,” https://www.mathworks.com/help/simulink/slref/linmod.html, 2024, accessed: 2024-05-15.

[30] H. Holttinen, A. Groom, E. Kennedy, D. Woodfin, L. Barroso, A. Orths, K. Ogimoto, C. Wang, R. Moreno, K. Parks, and T. Ackermann, “Variable renewable energy integration: Status around the world,” *IEEE Power and Energy Magazine*, vol. 19, no. 6, pp. 86–96, Nov 2021.

[31] B. Badrzadeh, Z. Emin, S. Goyal, S. Grogan, A. Haddadi, A. Halley, A. Louis, T. Lund, J. Matevosyan, T. Morton, D. Premm, and S. Sproul, “System strength,” *CIGRE Science and Technology Journal:*, vol. 21, Feburary 2021.

[32] S.-H. Huang, J. Schmall, J. Conto, J. Adams, Y. Zhang, and C. Carter, “Voltage control challenges on weak grids with high penetration of wind generation: Ercot experience,” in *2012 IEEE Power and Energy Society General Meeting*. IEEE, 2012, pp. 1–7.

[33] C. Li, “Unstable operation of photovoltaic inverter from field experiences,” *IEEE Transactions on Power Delivery*, vol. 33, no. 2, pp. 1013–1015, 2018.

[34] A. Jalali, B. Badrzadeh, J. Lu, N. Modi, and M. Gordon, “System strength challenges and solutions developed for a remote area of australian power system with high penetration of inverter-based resources,” *CIGRE Sci. Eng. J.*, pp. 27–37, 2021.

[35] Y. Cheng, L. Fan, J. Rose, F. Huang, J. Schmall, X. Wang, X. Xie, J. Shair, J. Ramamurthy, N. Modi, C. Li, C. Wang, S. Shah, B. C. Pal, Z. Miao, A. Isaacs, J. Mahseredjian, and Z. J. Zhou, “Real-world subsynchronous oscillation events in power grids with high penetrations of inverter-based resources,” *IEEE Transactions on Power Systems*, pp. 1–1, 2022.

[36] L. Fan, Z. Miao, S. Shah, Y. Cheng, J. Rose, S.-H. Huang, B. Pal, X. Xie, N. Modi, S. Wang, and S. Zhu, “Real-world 20-hz ibr subsynchronous oscillations: Signatures and mechanism analysis,” *IEEE Transactions on Energy Conversion*, pp. 1–11, 2022.

[37] B. Wen, D. Boroyevich, R. Burgos, P. Mattavelli, and Z. Shen, “Analysis of d-q small-signal impedance of grid-tied inverters,” *IEEE Transactions on Power Electronics*, vol. 31, no. 1, pp. 675–687, 2016.

[38] L. Huang, C. Wu, D. Zhou, and F. Blaabjerg, “A double-plls-based impedance reshaping method for extending stability range of grid-following inverter under weak grid,” *IEEE Transactions on Power Electronics*, vol. 37, no. 4, pp. 4091–4104, 2022.

[39] C. Guo, W. Liu, C. Zhao, and R. Iravani, “A frequency-based synchronization approach for the vsc-hvdc station connected to a weak ac grid,” *IEEE Transactions on Power Delivery*, vol. 32, no. 3, pp. 1460–1470, 2017.

[40] C. Li, S. Wang, F. Colas, and J. Liang, “Dominant instability mechanism of vsi connecting to a very weak grid,” *IEEE Transactions on Power Systems*, vol. 37, no. 1, pp. 828–831, 2022.

[41] H. Gong, X. Wang, and L. Harnefors, “Rethinking current controller design for pll-synchronized vscs in weak grids,” *IEEE Transactions on Power Electronics*, vol. 37, no. 2, pp. 1369–1381, 2022.

[42] A. Egea-Alvarez, S. Fekriasl, F. Hassan, and O. Gomis-Bellmunt, “Advanced vector control for voltage source converters connected to weak grids,” *IEEE Transactions on Power Systems*, vol. 30, no. 6, pp. 3072–3081, 2015.

[43] G. Wu, H. Sun, B. Zhao, S. Xu, X. Zhang, A. Egea-Àlvarez, S. Wang, G. Li, Y. Li, and X. Zhou, “Low-frequency converter-driven oscillations in weak grids: Explanation and damping improvement,” *IEEE Transactions on Power Systems*, vol. 36, no. 6, pp. 5944–5947, 2021.

[44] Y. Li, L. Fan, and Z. Miao, “Stability control for wind in weak grids,” *IEEE Transactions on Sustainable Energy*, vol. 10, no. 4, pp. 2094–2103, 2018.

[45] S.-H. Huang, J. Schmall, J. Conto, J. Adams, Y. Zhang, and C. Carter, “Voltage control challenges on weak grids with high penetration of wind generation: Ercot experience,” in *2012 IEEE Power and Energy Society General Meeting*. IEEE, 2012, pp. 1–7.

[46] L. Fan, *Control and dynamics in power systems and microgrids*. CRC Press, 2017.

[47] L. Fan and Z. Miao, “An explanation of oscillations due to wind power plants weak grid interconnection,” *IEEE Transactions on Sustainable Energy*, vol. 9, no. 1, pp. 488–490, 2018.

[48] Y. Li, L. Fan, Y. Zhou, and Z. Miao, “Stability enhancement module for grid-following converters: Hardware implementation and validation,” *International Transactions on Electrical Energy Systems*, vol. 31, no. 11, p. e13115, 2021.

[49] “NERC — Report Title — Report Date I Integrating Inverter-Based Resources into Low Short Circuit Strength Systems,” 2017. [Online]. Available: https://www.nerc.com/comm/RSTC_Reliability_Guidelines/Item_4a._Integrating%20_Inverter-Based_Resources_into_Low_Short_Circuit_Strength_Systems_-_2017-11-08-FINAL.pdf

[50] B. Badrzadeh, N. Modi, N. Crooks, and A. Jalali, “Power system operation with reduced system strength for inverter-connected generation during prior outage conditions,” *CIGRE SCIENCE & ENGINEERING*, vol. 17, pp. 141–149, 2020.

[51] A. Jalali, B. Badrzadeh, J. Lu, N. Modi, and M. Gordon, “System strength challenges and solutions developed for a remote area of australian power system with high penetration of inverter-based resources,” *CIGRE SCIENCE & ENGINEERING*, vol. 20, pp. 27–37, Feb 2021.

[52] L. Fan, Z. Miao, and S. Shah, “Mechanism analysis of wind turbine var oscillations,” *IEEE Transactions on Industrial Electronics*, pp. 1–4, 2022.

[53] L. Fan, Z. Miao, S. Shah, P. Koralewicz, and V. Gevorgian, "Solar pv and bess plant-level voltage control and interactions: Experiments and analysis," *IEEE Transactions on Energy Conversion*, pp. 1–10, 2023.

[54] "A universal grid-forming inverter model and simulation-based characterization across timescales," in *56th Annual Hawaii International Conference on System Sciences, HICSS 2023*. IEEE Computer Society, 2023, pp. 2631–2640.

[55] D. Ramasubramanian, W. Baker, J. Matevosyan, S. Pant, and S. Achilles, "Asking for fast terminal voltage control in grid following plants could provide benefits of grid forming behavior," *IET Generation, Transmission & Distribution*, 2022.

[56] L. Harnefors, M. Schweizer, J. Kukkola, M. Routimo, M. Hinkkanen, and X. Wang, "Generic pll-based grid-forming control," *IEEE Transactions on Power Electronics*, vol. 37, no. 2, pp. 1201–1204, 2022.

[57] J. W. Ballance and S. Goldberg, "Subsynchronous resonance in series compensated transmission lines," *IEEE Transactions on Power Apparatus and Systems*, vol. PAS-92, no. 5, pp. 1649–1658, 1973.

[58] Y. Cheng, L. Fan, J. Rose, S.-H. Huang, J. Schmall, X. Wang, X. Xie, J. Shair, J. R. Ramamurthy, N. Modi, C. Li, C. Wang, S. Shah, B. Pal, Z. Miao, A. Isaacs, J. Mahseredjian, and J. Zhou, "Real-world subsynchronous oscillation events in power grids with high penetrations of inverter-based resources," *IEEE Transactions on Power Systems*, vol. 38, no. 1, pp. 316–330, 2023.

[59] L. Fan, Z. Miao, D. Ramasubramanian, and H. Ding, "Operational challenges of solar PV plus storage power plants and modeling recommendations," *IEEE Open Access Journal of Power and Energy*, vol. 10, pp. 477–489, 2023.

[60] L. Fan and Z. Miao, "Nyquist-stability-criterion-based SSR explanation for type-3 wind generators," *IEEE Transactions on Energy Conversion*, vol. 27, no. 3, pp. 807–809, 2012.

[61] X. Xie, X. Zhang, H. Liu, H. Liu, Y. Li, and C. Zhang, “Characteristic analysis of subsynchronous resonance in practical wind farms connected to series-compensated transmissions,” *IEEE Transactions on Energy Conversion*, vol. 32, no. 3, pp. 1117–1126, 2017.

[62] R. K. Varma, S. Auddy, and Y. Semsedini, “Mitigation of subsynchronous resonance in a series-compensated wind farm using FACTS controllers,” *IEEE Transactions on Power Delivery*, vol. 23, no. 3, pp. 1645–1654, 2008.

[63] L. Fan and Z. Miao, “Analytical model building for type-3 wind farm subsynchronous oscillation analysis,” *Electric Power Systems Research*, vol. 201, p. 107566, 2021. [Online]. Available: https://www.sciencedirect.com/science/article/pii/S0378779621005472

[64] H. Ma, P. Brogan, K. Jensen, and R. Nelson, “Sub-synchronous control interaction studies between full-converter wind turbines and series-compensated ac transmission lines,” in *2012 IEEE Power and Energy Society General Meeting*. IEEE, 2012, pp. 1–5.

[65] M. Beza and M. Bongiorno, “On the risk for subsynchronous control interaction in type 4 based wind farms,” *IEEE Transactions on Sustainable Energy*, vol. 10, no. 3, pp. 1410–1418, 2019.

[66] Y. Xu, M. Zhang, L. Fan, and Z. Miao, “Small-signal stability analysis of type-4 wind in series-compensated networks,” *IEEE Transactions on Energy Conversion*, vol. 35, no. 1, pp. 529–538, 2020.

[67] North American Electric Reliability Corporation, “Grid forming technology: Bulk power system reliability considerations,” https://www.nerc.com/comm/RSTC_Reliability_Guidelines/White_Paper_Grid_Forming_Technology.pdf#search=Grid%20Forming%20Technology, [Accessed 14-01-2024].

[68] L. Fan, C. Zhu, Z. Miao, and M. Hu, “Modal analysis of a dfig-based wind farm interfaced with a series compensated network,” vol. 26, no. 4, pp. 1010–1020, 2011.

[69] H.-P. Beck and R. Hesse, “Virtual synchronous machine,” *2007 9th International Conference on Electrical Power Quality and Utilisation*, pp. 1–6, 2007. [Online]. Available: https://api.semanticscholar.org/CorpusID:42096573

[70] N. Mohammed, H. H. Alhelou, and B. Bahrani, *Grid-Forming Power Inverters: Control and Applications*. CRC Press, 2023.

[71] S.-H. Huang, J. Schmall, J. Conto, J. Adams, Y. Zhang, and C. Carter, “Voltage control challenges on weak grids with high penetration of wind generation: Ercot experience,” in *2012 IEEE Power and Energy Society General Meeting*, 2012, pp. 1–7.

[72] T. Wagner, C. Kittl, J. Jakob, J. Hiry, and U. Häger, “Digital twins in power systems: A proposal for a definition,” *IEEE Power and Energy Magazine*, vol. 22, no. 1, pp. 16–23, 2024.

[73] Y. Peng, S. Zhao, and H. Wang, “A digital twin based estimation method for health indicators of dc–dc converters,” *IEEE Transactions on Power Electronics*, vol. 36, no. 2, pp. 2105–2118, 2020.

[74] Q. Wu, W. Wang, Q. Wang, L. Xiao, and B. Hu, “Digital twin approach for degradation parameters identification of a single-phase dc-ac inverter,” in *2022 IEEE Applied Power Electronics Conference and Exposition (APEC)*, 2022, pp. 1725–1730.

[75] M. Milton, C. De La O, H. L. Ginn, and A. Benigni, “Controller-embeddable probabilistic real-time digital twins for power electronic converter diagnostics,” *IEEE Transactions on Power Electronics*, vol. 35, no. 9, pp. 9850–9864, 2020.

[76] K. Sivalingam, M. Sepulveda, M. Spring, and P. Davies, “A review and methodology development for remaining useful life prediction of offshore fixed and floating wind turbine power converter with digital twin technology perspective,” in *2018 2nd International Conference on Green Energy and Applications (ICGEA)*, 2018, pp. 197–204.

[77] P. Jain, J. Poon, J. P. Singh, C. Spanos, S. R. Sanders, and S. K. Panda, “A digital twin approach for fault diagnosis in distributed photovoltaic systems,” *IEEE Transactions on Power Electronics*, vol. 35, no. 1, pp. 940–956, 2019.

[78] Y.-Y. Hong and G. F. D. Apolinario, “Ancillary services and risk assessment of networked microgrids using digital twin,” *IEEE Transactions on Power Systems*, vol. 38, no. 5, pp. 4542–4558, 2023.

[79] M. Zhou, J. Yan, and D. Feng, “Digital twin framework and its application to power grid online analysis,” *CSEE Journal of Power and Energy Systems*, vol. 5, no. 3, pp. 391–398, 2019.

[80] F. Arraño-Vargas and G. Konstantinou, “Modular design and real-time simulators toward power system digital twins implementation,” *IEEE Transactions on Industrial Informatics*, vol. 19, no. 1, pp. 52–61, 2023.

[81] ——, “Synthetic grid modeling for real-time simulations,” in *2021 IEEE PES Innovative Smart Grid Technologies - Asia (ISGT Asia)*, 2021, pp. 1–5.

[82] L. Fan, Z. Miao, and M. Zhang, “Subcycle overvoltage dynamics in solar pvs,” *IEEE Transactions on Power Delivery*, vol. 36, no. 3, pp. 1847–1858, 2021.

[83] L. Fan and Z. Miao, “Root cause analysis of ac overcurrent in july 2020 san fernando disturbance,” *IEEE Transactions on Power Systems*, vol. 36, no. 5, pp. 4892–4895, 2021.

[84] L. Fan, Z. Miao, S. Shah, Y. Cheng, J. Rose, S.-H. Huang, B. Pal, X. Xie, N. Modi, S. Wang *et al.*, “Real-world 20-hz ibr subsynchronous oscillations: Signatures and mechanism analysis,” *IEEE Transactions on Energy Conversion*, vol. 37, no. 4, pp. 2863–2873, 2022.

[85] Y. Cheng, L. Fan, J. Rose, S.-H. Huang, J. Schmall, X. Wang, X. Xie, J. Shair, J. R. Ramamurthy, N. Modi *et al.*, “Real-world subsynchronous oscillation events in power grids with high penetrations of inverter-based resources,” *IEEE Transactions on Power Systems*, vol. 38, no. 1, pp. 316–330, 2022.

[86] L. Fan, Z. Miao, D. Piper, D. Ramasubramanian, L. Zhu, and P. Mitra, “Analysis of 0.1-hz var oscillations in solar photovoltaic power plants,” *IEEE Transactions on Sustainable Energy*, vol. 14, no. 1, pp. 734–737, 2023.

[87] L. Fan, “Modeling type-4 wind in weak grids,” *IEEE Transactions on Sustainable Energy*, vol. 10, no. 2, pp. 853–864, 2019.

[88] A. H. Etemadi, E. J. Davison, and R. Iravani, “A decentralized robust control strategy for multi-der microgrids—part ii: Performance evaluation,” *IEEE Transactions on Power Delivery*, vol. 27, no. 4, pp. 1854–1861, 2012.

[89] M. Abedini, M. Davarpanah, M. Sanaye-Pasand, S. M. Hashemi, and R. Iravani, “Generator out-of-step prediction based on faster-than-real-time analysis: Concepts and applications,” *IEEE Transactions on Power Systems*, vol. 33, no. 4, pp. 4563–4573, 2017.

[90] P. Pourbeik, J. J. Sanchez-Gasca, J. Senthil, J. D. Weber, P. Zadkhast, Y. Kazachkov, S. Tacke, J. Wen, and A. Ellis, “Generic dynamic models for modeling wind power plants and other renewable technologies in large-scale power system studies,” *IEEE Transactions on Energy Conversion*, vol. 32, no. 3, pp. 1108–1116, 2017.

[91] M. Luchini, O. Batista, F. Lopes, R. Reis, and B. Souza, “Equivalent grid-following inverter-based generator model for atp/atpdraw simulations,” *Electric Power Systems Research*, vol. 223, p. 109624, 2023. [Online]. Available: https://www.sciencedirect.com/science/article/pii/S0378779623005138

# Appendix A: Copyright Permissions

The permission below is for the reproduction of material in Chapter 2 and Chapter 3.

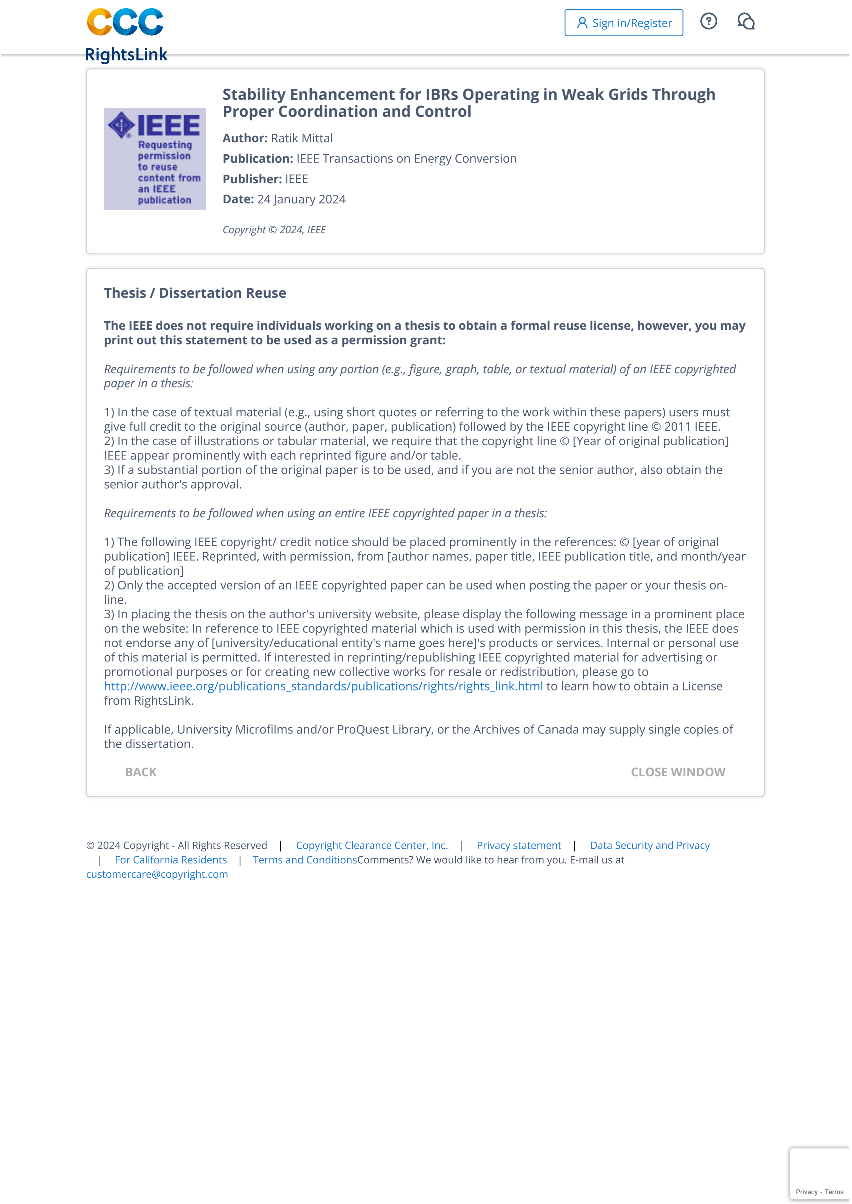

**Stability Enhancement for IBRs Operating in Weak Grids Through Proper Coordination and Control**

**Author:** Ratik Mittal
**Publication:** IEEE Transactions on Energy Conversion
**Publisher:** IEEE
**Date:** 24 January 2024

*Copyright © 2024, IEEE*

**Thesis / Dissertation Reuse**

**The IEEE does not require individuals working on a thesis to obtain a formal reuse license, however, you may print out this statement to be used as a permission grant:**

*Requirements to be followed when using any portion (e.g., figure, graph, table, or textual material) of an IEEE copyrighted paper in a thesis:*

1) In the case of textual material (e.g., using short quotes or referring to the work within these papers) users must give full credit to the original source (author, paper, publication) followed by the IEEE copyright line © 2011 IEEE.
2) In the case of illustrations or tabular material, we require that the copyright line © [Year of original publication] IEEE appear prominently with each reprinted figure and/or table.
3) If a substantial portion of the original paper is to be used, and if you are not the senior author, also obtain the senior author's approval.

*Requirements to be followed when using an entire IEEE copyrighted paper in a thesis:*

1) The following IEEE copyright/ credit notice should be placed prominently in the references: © [year of original publication] IEEE. Reprinted, with permission, from [author names, paper title, IEEE publication title, and month/year of publication]
2) Only the accepted version of an IEEE copyrighted paper can be used when posting the paper or your thesis on-line.
3) In placing the thesis on the author's university website, please display the following message in a prominent place on the website: In reference to IEEE copyrighted material which is used with permission in this thesis, the IEEE does not endorse any of [university/educational entity's name goes here]'s products or services. Internal or personal use of this material is permitted. If interested in reprinting/republishing IEEE copyrighted material for advertising or promotional purposes or for creating new collective works for resale or redistribution, please go to http://www.ieee.org/publications_standards/publications/rights/rights_link.html to learn how to obtain a License from RightsLink.

If applicable, University Microfilms and/or ProQuest Library, or the Archives of Canada may supply single copies of the dissertation.

© 2024 Copyright - All Rights Reserved | Copyright Clearance Center, Inc. | Privacy statement | Data Security and Privacy | For California Residents | Terms and ConditionsComments? We would like to hear from you. E-mail us at customercare@copyright.com

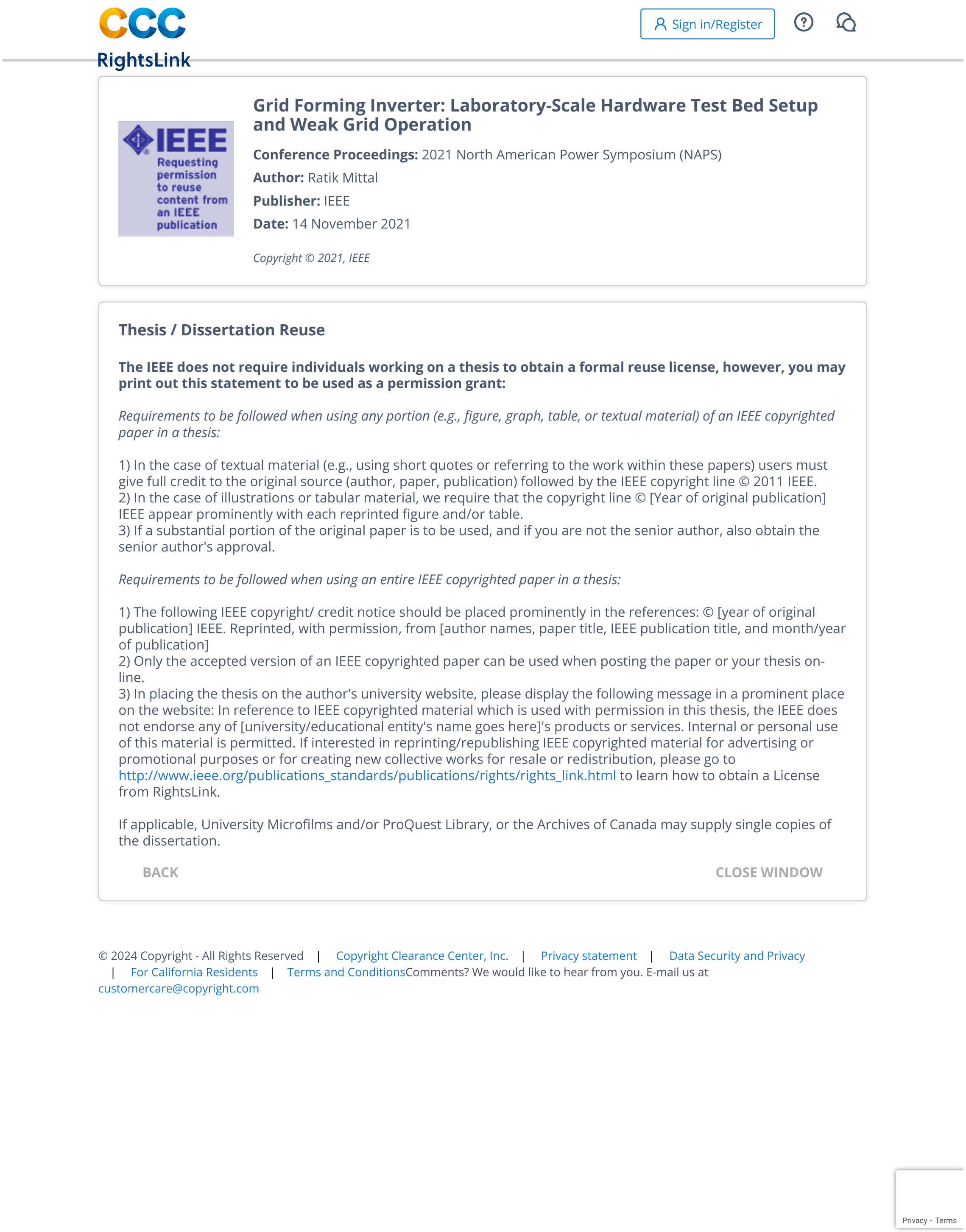

IEEE
Requesting permission to reuse content from an IEEE publication

## Grid Forming Inverter: Laboratory-Scale Hardware Test Bed Setup and Weak Grid Operation

**Conference Proceedings:** 2021 North American Power Symposium (NAPS)
**Author:** Ratik Mittal
**Publisher:** IEEE
**Date:** 14 November 2021

*Copyright © 2021, IEEE*

### Thesis / Dissertation Reuse

**The IEEE does not require individuals working on a thesis to obtain a formal reuse license, however, you may print out this statement to be used as a permission grant:**

*Requirements to be followed when using any portion (e.g., figure, graph, table, or textual material) of an IEEE copyrighted paper in a thesis:*

1) In the case of textual material (e.g., using short quotes or referring to the work within these papers) users must give full credit to the original source (author, paper, publication) followed by the IEEE copyright line © 2011 IEEE.
2) In the case of illustrations or tabular material, we require that the copyright line © [Year of original publication] IEEE appear prominently with each reprinted figure and/or table.
3) If a substantial portion of the original paper is to be used, and if you are not the senior author, also obtain the senior author's approval.

*Requirements to be followed when using an entire IEEE copyrighted paper in a thesis:*

1) The following IEEE copyright/ credit notice should be placed prominently in the references: © [year of original publication] IEEE. Reprinted, with permission, from [author names, paper title, IEEE publication title, and month/year of publication]
2) Only the accepted version of an IEEE copyrighted paper can be used when posting the paper or your thesis on-line.
3) In placing the thesis on the author's university website, please display the following message in a prominent place on the website: In reference to IEEE copyrighted material which is used with permission in this thesis, the IEEE does not endorse any of [university/educational entity's name goes here]'s products or services. Internal or personal use of this material is permitted. If interested in reprinting/republishing IEEE copyrighted material for advertising or promotional purposes or for creating new collective works for resale or redistribution, please go to http://www.ieee.org/publications_standards/publications/rights/rights_link.html to learn how to obtain a License from RightsLink.

If applicable, University Microfilms and/or ProQuest Library, or the Archives of Canada may supply single copies of the dissertation.

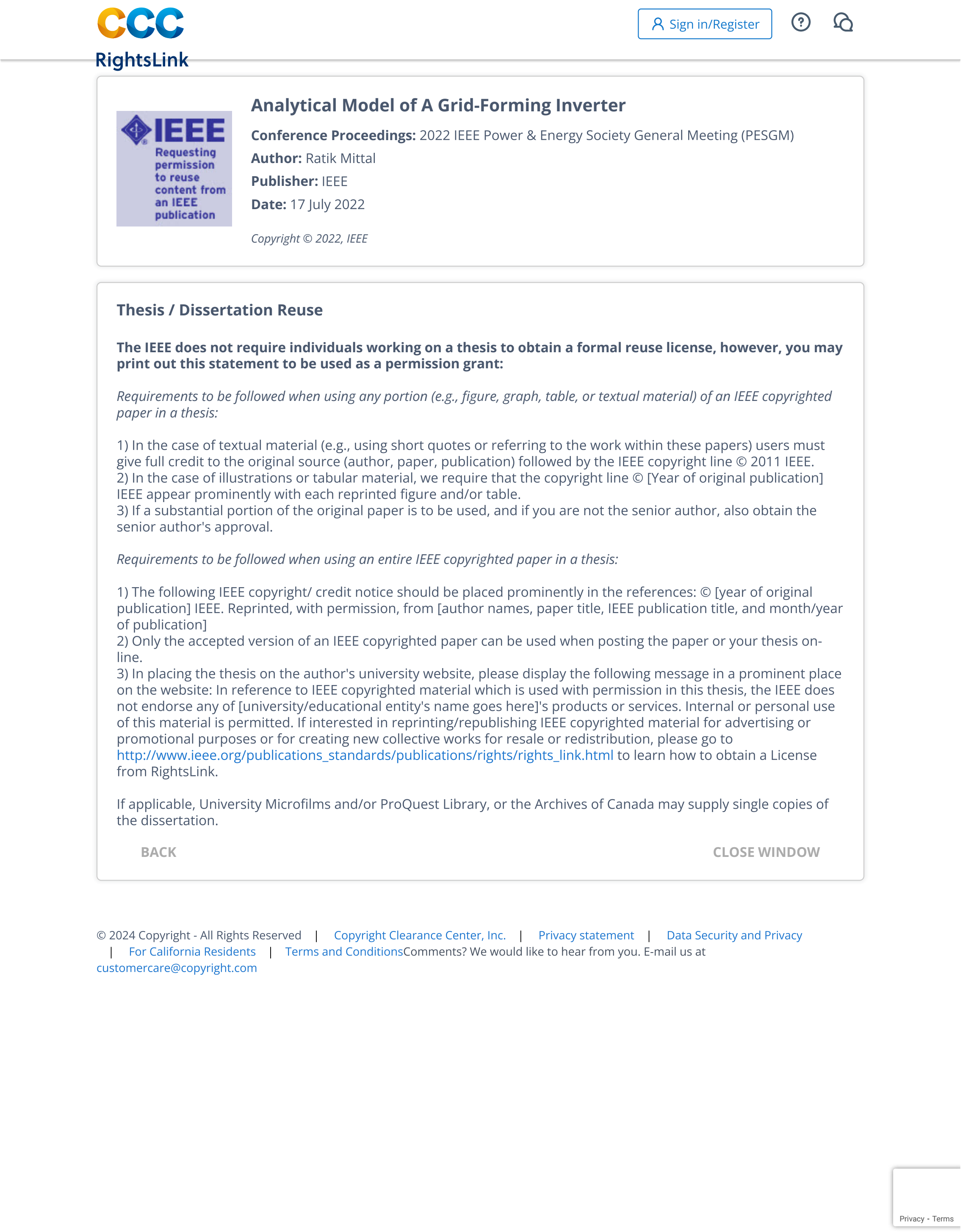

## Analytical Model of A Grid-Forming Inverter

**Conference Proceedings:** 2022 IEEE Power & Energy Society General Meeting (PESGM)
**Author:** Ratik Mittal
**Publisher:** IEEE
**Date:** 17 July 2022

*Copyright © 2022, IEEE*

### Thesis / Dissertation Reuse

**The IEEE does not require individuals working on a thesis to obtain a formal reuse license, however, you may print out this statement to be used as a permission grant:**

*Requirements to be followed when using any portion (e.g., figure, graph, table, or textual material) of an IEEE copyrighted paper in a thesis:*

1) In the case of textual material (e.g., using short quotes or referring to the work within these papers) users must give full credit to the original source (author, paper, publication) followed by the IEEE copyright line © 2011 IEEE.
2) In the case of illustrations or tabular material, we require that the copyright line © [Year of original publication] IEEE appear prominently with each reprinted figure and/or table.
3) If a substantial portion of the original paper is to be used, and if you are not the senior author, also obtain the senior author's approval.

*Requirements to be followed when using an entire IEEE copyrighted paper in a thesis:*

1) The following IEEE copyright/ credit notice should be placed prominently in the references: © [year of original publication] IEEE. Reprinted, with permission, from [author names, paper title, IEEE publication title, and month/year of publication]
2) Only the accepted version of an IEEE copyrighted paper can be used when posting the paper or your thesis on-line.
3) In placing the thesis on the author's university website, please display the following message in a prominent place on the website: In reference to IEEE copyrighted material which is used with permission in this thesis, the IEEE does not endorse any of [university/educational entity's name goes here]'s products or services. Internal or personal use of this material is permitted. If interested in reprinting/republishing IEEE copyrighted material for advertising or promotional purposes or for creating new collective works for resale or redistribution, please go to http://www.ieee.org/publications_standards/publications/rights/rights_link.html to learn how to obtain a License from RightsLink.

If applicable, University Microfilms and/or ProQuest Library, or the Archives of Canada may supply single copies of the dissertation.

# About the Author

Ratik Mittal was born on September 27, 1993, in Nainital, India. He earned his Bachelor of Engineering in Electrical Engineering from Thapar University, Patiala, India, in 2015, followed by a Master's degree from the University of South Florida, Tampa, USA, in 2019. He commenced his Ph.D. studies at the University of South Florida's Smart Grid Power Systems Lab in May 2019. His research focuses on the modeling of inverter-based resources, stability analysis, power flow studies, and hardware-in-the-loop testing and modeling.

Following the completion of his Ph.D. in the summer of 2024, Ratik will be joining Quanta Technology as Engineer III in the Transmission and Regulatory department.